

---

# Magnetic reconnection during sawtooth instability in ASDEX Upgrade

Oleg Samoylov

---



München 2022



---

# **Magnetic reconnection during sawtooth instability in ASDEX Upgrade**

**Oleg Samoylov**

---

Doctoral Thesis  
an der Fakultät für Physik  
der Ludwig–Maximilians–Universität  
München

vorgelegt von  
Oleg Samoylov  
aus Perm, Russland

München, 22. August 2022

Erstgutachter: Prof. Dr. Hartmut Zohm

Zweitgutachter: Prof. Dr. Harald Lesch

Tag der mündlichen Prüfung: 26. October 2022

To the memory of my grandparents  
Lena (1926 - 2013) and Vova (1933 - 2006) Shcherbininy

# Zusammenfassung

Im Plasmazentrum eines Tokamaks kann es zu periodisch auftretenden Instabilitäten kommen, welche aufgrund ihres Erscheinungsbildes Sägezähne genannt werden. In dieser Arbeit werden zwei physikalische Aspekte des Sägezahn-Crashes behandelt. Erstens wurde untersucht, ob die magnetische Rekonnexion während des Crashes globaler (überall entlang der  $q = 1$  helikalen magnetischen Linie) oder lokaler Natur (nur an einer bestimmten toroidalen Stelle auf der  $q = 1$  helikalen magnetischen Linie) ist. Die numerische Analyse der Wärmeausbreitung während der Crash-Phase zeigt, dass sich die Wärme helikal entlang des Torus schneller verteilt als die zeitliche Auflösung aller existierenden Messmethoden der Elektronentemperatur wie zum Beispiel die Elektronenzyklotron-Emissionen (ECE) Diagnostik. Dies macht lokale und globale (symmetrisch entlang der Helixachse) magnetische Rekonnexion für einen Beobachter ununterscheidbar. Nur wenn die Wärmeausbreitung eines lokalen Crashes auf eine helikale Region begrenzt bleibt, ist es möglich diese von einem globalen Crash zu unterscheiden. Die statistische Analyse von Sägezahn-Crashes mit Hilfe der ECE-Bild (ECEI) Diagnostik im ASDEX Upgrade zeigt keine Verschiebung der Wärme innerhalb einer endlichen helikalen Region. Die statistischen Daten deuten auf eine globale magnetische Rekonnexion.

Zweitens wurde die radiale Ausbreitungsgeschwindigkeit während des Crashes mittels der ECEI Diagnostik untersucht. Diese Messung stellt einen neuen Ansatz zur Untersuchung der magnetischen Rekonnexion während des Sägezahn-Crashes dar. Es ermöglicht die Geschwindigkeit der Rekonnexion aus der Geschwindigkeit des radialen Wärmepulses zu bestimmen. Diese Messungen wurden mit nichtlinearen Zwei-Fluid-MHD Simulationen verglichen. Der Vergleich zeigt eine gute quantitative Übereinstimmung, was darauf hindeutet, dass Zwei-Fluid-Effekte (Trägheit und Druckgradient der Elektronen) für die korrekte Vorhersage der experimentellen Ergebnisse ausreichen. Im Gegensatz dazu stimmen die Crash-Zeiten des Kadomtsev-Modells, das auf einem Ein-Fluid-Bild der magnetischen Rekonnexion basiert, nicht mit den experimentellen Ergebnissen überein.

# Abstract

Sawtooth oscillations are internal periodic relaxation events in a tokamak that lead to a rapid redistribution (crash) of plasma core temperature and density. Two topics of sawtooth crash physics are studied. First, the question of whether magnetic reconnection during the crash has global (everywhere along the  $q = 1$  helical magnetic line) or local (only at a particular toroidal location on the  $q = 1$  helical magnetic line) nature is investigated. Numerical analysis of heat distribution during the crash phase shows that heat distributes itself helically along the torus faster than the temporal resolution of any existing electron cyclotron emission (ECE) diagnostics. It makes local and global (symmetric along the helical axis) magnetic reconnection indistinguishable for an observer. Only if the heat propagation of a local crash remains confined within a helical region, then the distinction between the local and global crashes can be measured. Statistical analysis of sawtooth crashes with the ECEI diagnostic is conducted in ASDEX Upgrade. The displacement of the heat within a finite helical region has not been observed. The statistical data supports global magnetic reconnection.

Second, the radial velocity of the plasma core during the crash is studied with the electron cyclotron emission imaging (ECEI) diagnostic. These measurements introduce a novel approach for studying magnetic reconnection during sawteeth since the radial velocity characterises the rate of the reconnection. The measurements have been compared with nonlinear two-fluid simulations. The comparison reveals good qualitative and quantitative agreement, which indicates that two-fluid effects (inertia and pressure gradient of electrons) are sufficient for the correct prediction of the experimental results. Contrarily, the crash time of the Kadomtsev model, which is based on a single-fluid picture of magnetic reconnection, disagrees with the experimental results.



# Contents

|   |            |
|---|------------|
| <b>Zusammenfassung</b>                                    | <b>vi</b>  |
| <b>Abstract</b>   | <b>vii</b> |
| <b>1 Introduction</b>                                     | <b>1</b>   |
| 1.1 Nuclear Fusion . . . . .                              | 1          |
| 1.2 Sawtooth instability . . . . .                        | 6          |
| 1.3 Magnetic Reconnection . . . . .                       | 8          |
| 1.4 Outline . . . . .                                     | 10         |
| <b>2 Theory</b>   | <b>13</b>  |
| 2.1 MHD . . . . .   | 13         |
| 2.2 Magnetic reconnection . . . . .                       | 15         |
| 2.2.1 Vacuum . . . . .                                    | 15         |
| 2.2.2 Perfectly conducting plasma . . . . .               | 16         |
| 2.2.3 Resistive plasma . . . . .                          | 18         |
| 2.2.4 Types of reconnection in a tokamak plasma . . . . . | 20         |
| 2.2.5 Sweet-Parker model . . . . .                        | 22         |
| 2.2.6 Beyond Sweet-Parker . . . . .                       | 24         |
| 2.2.7 Strong guide field reconnection . . . . .           | 32         |
| 2.3 Sawtooth instability . . . . .                        | 34         |
| 2.3.1 Notations in toroidal coordinates . . . . .         | 34         |
| 2.3.2 Phenomenology . . . . .                             | 37         |
| 2.3.3 Kink mode . . . . .                                 | 37         |
| 2.3.4 Trigger problem . . . . .                           | 41         |
| 2.3.5 Kadomtsev model . . . . .                           | 41         |
| 2.3.6 Quasi-Interchange model (Jardin model) . . . . .    | 44         |
| 2.3.7 Stochastic model . . . . .                          | 46         |
| 2.3.8 Ballooning model . . . . .                          | 47         |
| 2.3.9 Postcursor . . . . .                                | 48         |
| 2.4 Summary . . . . .                                     | 49         |

|          |   |            |
|----------|---|------------|
| <b>3</b> | <b>Diagnostic</b>   | <b>51</b>  |
| 3.1      | ASDEX Upgrade . . . . .   | 51         |
| 3.2      | Magnetic coils . . . . .  | 53         |
| 3.3      | Soft X-ray . . . . .  | 53         |
| 3.4      | ECE . . . . .   | 55         |
| 3.4.1    | ECEI . . . . .  | 57         |
| 3.4.2    | Noise . . . . .   | 59         |
| 3.4.3    | Digital filtering of the noise . . . . .                            | 59         |
| 3.5      | Summary . . . . .   | 65         |
| <b>4</b> | <b>Global nature of magnetic reconnection during sawtooth crash</b> | <b>67</b>  |
| 4.1      | Introduction . . . . .  | 67         |
| 4.2      | Can a toroidally localized crash be measured? . . . . .             | 69         |
| 4.3      | Statistical analysis of sawtooth crashes . . . . .                  | 71         |
| 4.4      | Summary . . . . .   | 78         |
| <b>5</b> | <b>Velocimetry analysis of sawtooth crashes</b>                     | <b>79</b>  |
| 5.1      | Introduction . . . . .  | 79         |
| 5.2      | Description of the measurement and the simulation . . . . .         | 80         |
| 5.3      | Comparison of the experimental data with the simulation . . . . .   | 83         |
| 5.3.1    | Displacement . . . . .  | 83         |
| 5.3.2    | Angular frequency . . . . .   | 85         |
| 5.3.3    | Radial velocity . . . . .   | 86         |
| 5.4      | Summary . . . . .   | 90         |
| <b>6</b> | <b>Conclusions</b>  | <b>93</b>  |
|          | <b>Appendix</b>   | <b>96</b>  |
| <b>A</b> | <b>Typical core plasma parameters in ASDEX Upgrade</b>              | <b>96</b>  |
| <b>B</b> | <b>Transport coefficients in GRILLIX</b>                            | <b>101</b> |
| <b>C</b> | <b>Crash statistic: plasma parameters</b>                           | <b>102</b> |
| <b>D</b> | <b>Velocimetry: plasma parameters</b>                               | <b>104</b> |
| <b>E</b> | <b>Plasma vortexes during the crash phase</b>                       | <b>105</b> |
|          | <b>Bibliography</b>   | <b>107</b> |
|          | <b>Acknowledgements</b>   | <b>127</b> |
|          | <b>The Author</b>   | <b>129</b> |





# Chapter 1

## Introduction

*If you want to make things  
complicated, there is no end.*

---

Qingquan Yu

The title of this thesis includes the words "sawtooth instability" and "ASDEX Upgrade", which are absent in the vocabulary of an average person. In this chapter, a reader may learn not only what is behind these words, but how they are related to a temperature of hundreds of million degrees Kelvin, to solar flares (which is still a mysterious phenomenon, although big flares may be visible even with a naked eye), to far located neutron stars (the closest are in hundreds of lightyears from us) and, finally, to an energy source that has been long hoped to meet human needs, not for just the next hundreds of thousands of years, but for as far into the future as we can see.

### 1.1 Nuclear Fusion

Our introduction begins with Nuclear Physics, which showed that there is "hidden" energy inside atoms. Humanity has succeeded to harness this hidden energy through a nuclear fission reaction. Fission is the splitting of a nucleus (such as  $U^{235}$ ) into two more-or-less equal fragments (fission products), with an associated release of energy. Currently, there are more than 400 nuclear fission power plants in 30 countries [Sta, 2022]. However, most of the fission plants were built between 1970 and 1990, even though the energy demand of humanity is ever-growing [Chen, 2011] and the problem of the climate change requires  $CO_2$  free energy sources [Hardy, 2003, Gore, 2007]. There are two main reasons why new fission plants are rarely built: first, negative public opinion about nuclear fusion due to the accidents in Chornobyl and Fukushima fission plants [Steinhauser et al., 2014], which lead to radioactive contamination of the surrounding environment; second, necessary long-term storage of nuclear waste (the waste must be isolated from the human environment for hundreds of thousands of years [Pescatore and Vári, 2006, Kautsky et al., 2016]). Except

for fission, one of the very few sustainable options that could replace fossil fuels as the world's primary energy source is nuclear fusion [Hoffert et al., 2002].

Nuclear Fusion is binding together or "fusing" two small nuclei into larger ones (in fission, in comparison, the other way around - large nuclei are split into smaller ones). Energy is released when the larger nuclei have higher binding energy than the smaller ones. This can be shown schematically in figure 1.1. Fusion Science studies the ways of harnessing the released energy and producing electrical energy in fusion power reactors. The research has been ongoing since the 1940s [Barbarino, 2020, Reinders, 2021], but the technology is still in its development phase.

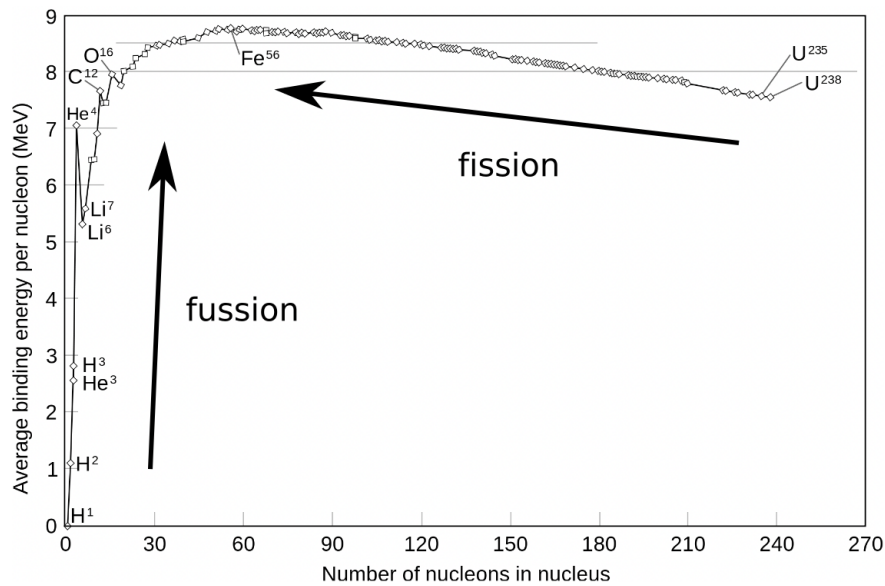


Figure 1.1: Binding energy per nucleon. Adapted from [Krane, 1991].

The most promising reaction (i.e. the easiest possible for the currently available technology) for the fusion is:



where D (or  $H_1^2$ ) is deuterium, a hydrogen isotope containing one proton and neutron, T (or  $H_1^3$ ) is tritium, a hydrogen isotope containing one proton and two neutrons;  $\alpha$  is helium ( $He_2^4$ ), containing two protons and two neutrons;  $n$  is a neutron.

The D-T fusion reaction releases 17.6 MeV in the form of the kinetic energy of the neutron and the alpha-particle ( $He_2^4$ ). The energy of the alpha-particle, which 20% (about 3.5 MeV) of the total released energy, will be used to keep the nuclear fusion reaction going. The neutron, which carries 80% (about 14.1 MeV) of the total released energy, has to be captured and its energy transformed into heat. In a fusion power plant, this heat, then, can be transformed into electricity. Although neither reaction product is itself radioactive, the neutron can induce radioactivity in the walls of the reactor, and this material has to be handled with care. However, the amount of the long-lived (more than

100 years) radioactive material expected in a fusion reactor is much smaller (three orders of magnitude) than the amount of nuclear waste in a regular fission power plant [Toschi, 1997, Chen, 2011].

To ignite D-T reaction (when the heat from the fusion-born particles compensates for losses during the reaction), one has to create a D-T plasma with sufficient density and temperature, that be sustained long enough for a sufficient number of fusion reactions to take place. The ignition criterion was first suggested by Lawson [Lawson, 1957], who estimated that D-T plasma should be heated to a temperature  $T \geq 15 \text{ keV}$  (170 million K) and must satisfy:

$$n\tau_E > 1.5 \cdot 10^{20} \text{ m}^{-3} \text{ s} \quad (1.2)$$

where  $n$  is the D-T plasma density;  $\tau_E$  is the energy confinement time, the ratio of the energy stored in the plasma to the heat loss rate. The Lawson criterion of the ignition is more commonly expressed in terms of the fusion "triple product" [Wesson and Campbell, 2011]:

$$nT\tau_E > (3 - 5) \cdot 10^{21} \text{ m}^{-3} \cdot \text{s} \cdot \text{keV} \quad (1.3)$$

where  $T$  is the temperature of the D-T plasma.

As we mentioned earlier, to achieve ignition, one has to heat the D-T plasma up to hundreds of millions of degrees of Kelvin, which is hotter than the Sun's core (15 million K). To sustain this temperature for a reactor-relevant amount of time (from one hour to a year), one has to use a magnetic field to confine the plasma. Due to the nature of the magnetic field, a moving charged particle experiences a force in the presence of a magnetic field, which is perpendicular to both particle velocity and the magnetic field. This force is called the Lorentz force:

$$F_L = q[\vec{v} \times \vec{B}] \quad (1.4)$$

where  $q$  is the particle charge,  $\vec{v}$  is the velocity vector of the particle, and  $\vec{B}$  is the magnetic field vector. As one sees from equation 1.4, the force does not affect a particle that is stationary nor one that moves only along a magnetic field line. Only the perpendicular motion of a charged particle is affected by the force. As a result, ions and electrons circle around magnetic field lines in gyration orbits as schematically shown in figure 1.2a.

If magnetic lines end on a wall somewhere, then the plasma will hit the wall and lose its energy, since Lorentz's force does not act parallel to the magnetic field and will not prevent the plasma-wall collision. The solution is to make magnetic lines that close into themselves and do not intersect the material wall, which results in a toroidal topology of magnetic field lines as shown in figure 1.2b. However, such a simple configuration of a purely toroidal axisymmetric field does not hold the plasma equilibrium with the magnetic field [Taylor and Newton, 2015]. The grad B drift is opposite for electrons and ions, which leads to the vertical separation of the positively and negatively charged particles and their accumulation on the opposite vertical ends (figure 1.2b). These separated charges create an electric field

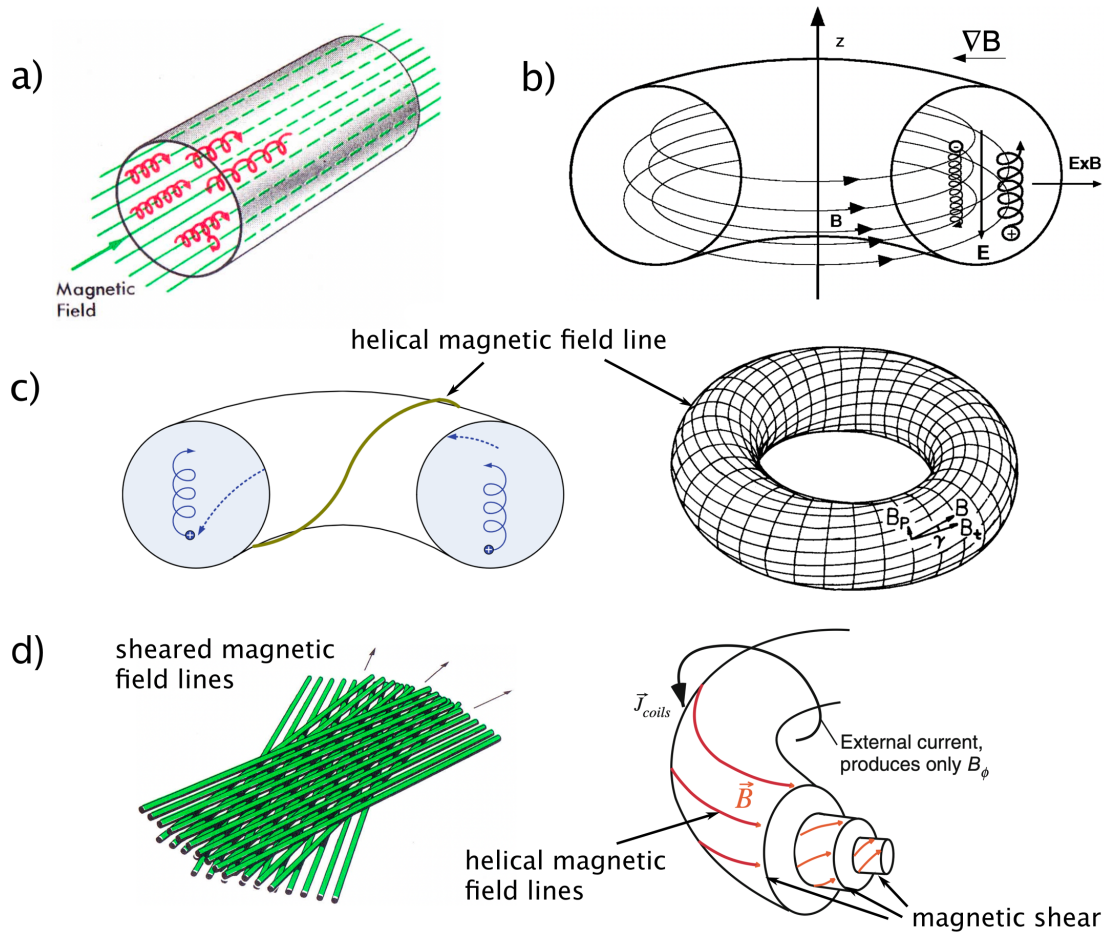


Figure 1.2: Illustration of plasma confinement in different magnetic field structures. In (a), in a homogeneous parallel field, charged particles travel in a helical orbit encircling some line of the magnetic field. The plasma particles are confined in the direction that is perpendicular to the magnetic field but move freely in the parallel direction. In (b), the plasma particles are not confined in the purely toroidal axisymmetric field (toroidal solenoid) due to the drift of charged particles outwards the torus. In (c), an example of a helical winding in a torus; and the compensation of the particle drifts in a helical field. Plasma particles can be confined in a torus with a helical magnetic field. In (d), illustration of magnetic field shear in planes and in a torus on different magnetic flux surfaces. The shear helps to suppress pressure-driven plasma instabilities. The figures are adapted from [Bishop, 1960, Dinklage et al., 2005, Chen, 2011, Igochine et al., 2015].

and result in an  $\mathbf{E} \times \mathbf{B}$  drift, which is the same for both ions and electrons. This drift of particles causes the whole plasma to move outwards away from the axis of symmetry. The plasma confinement is lost. In order to have an equilibrium in which the plasma pressure is balanced by the magnetic forces, it is also necessary to have a poloidal magnetic field (figure 1.2c). The resulting helical magnetic field compensates for the grad B drift and

prevents the charge separation [Wesson and Campbell, 2011, Igochine et al., 2015]. This way, due to the helical structure of the magnetic field, the plasma can be confined within toroidal surfaces in the equilibrium state. Finally, to suppress pressure-driven instabilities in the plasma and thus, improve its confinement and stability, a sheared magnetic field (or helically twisted magnetic field, shown in figure 1.2d) is necessary [Wesson and Campbell, 2011]. The effect of holding the plasma with sheared magnetic lines can be understood through a jello analogy of plasma [Chen, 2011]. Imagine that we try to squeeze jello with rubber bands that are parallel to each other. The jello would squeeze out between rubber bands, exchanging places with an equal volume of rubber, so that the rubber bands were on the inside and the jello on the outside. However, if we weave the rubber bands into a mesh (i.e. introduce shear), then it would be harder for the jello to penetrate through the created rubber mesh. The helical twist of magnetic lines on each magnetic surface is usually described by a value  $q = \frac{\Delta\phi}{\Delta\theta}$  (where  $\phi$  is the toroidal angle, and  $\theta$  is the poloidal angle), which is called "safety factor". Large  $q$  means the twist is gentle, and small  $q$  means that the twist is tight.

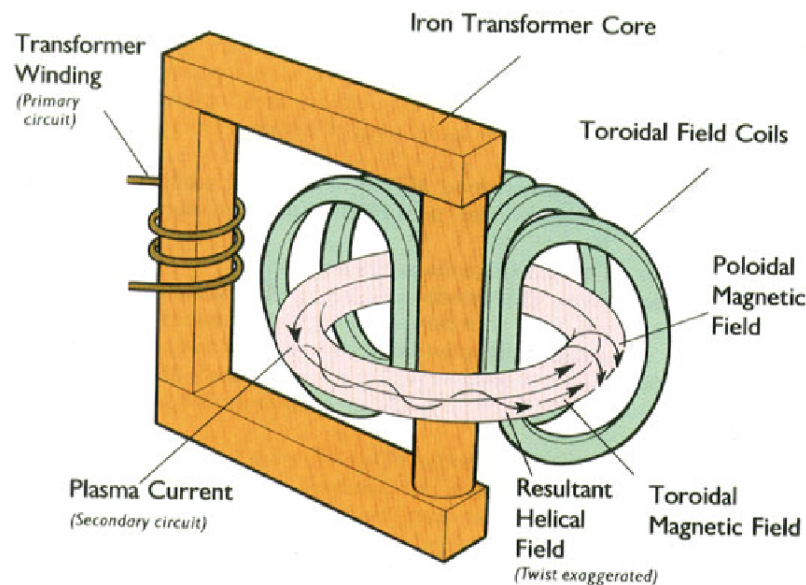


Figure 1.3: Basic setup for a tokamak. The figure is taken from [Reinders, 2021].

Toroidal plasma devices with helically twisted magnetic fields are seen to be the most promising candidates for future fusion power plants. So far, the highest triple product [Keilhacker et al., 1999, Isayama et al., 2003] has been achieved in the tokamak configuration [Artsimovich, 1972, Wesson and Campbell, 2011]. The tokamak is a toroidal plasma device (shown in figure 1.3), where the helical twist is achieved by driving a large amount of current through plasma itself. Plasma has a resistivity due to electron-ion collisions and can be considered as a one-turn secondary winding in the transformer of a tokamak. When an electric field is applied around the plasma loop through the transformer scheme, the electrons carry the current. The current flows in the toroidal direction (the long way

around the torus), and it generates a poloidal magnetic field (the short way around the torus). When this poloidal field is added to the main toroidal field from the large outside coils, the magnetic field inside the plasma is twisted into helices. Two tokamaks, ITER [Green et al., 2003] and SPARC [Creely et al., 2020], are being built with the aim to achieve D-T ignition and study burning plasma experiments. The first experiments in both devices are planned in  $\sim 2025-2027$ . The experimental results of this thesis have been obtained in ASDEX Upgrade [Herrmann and Gruber, 2003], which is a research-oriented tokamak operating in deuterium-deuterium plasma (more details are given in Chapter 3).

Having described nuclear fusion research in tokamaks and its relevance, we have come close to the research field of this thesis - instabilities in tokamaks. In tokamaks, a single charged particle of plasma is confined within this toroidal magnetic bottle. However, this magnetic trap is still imperfect. Charged particles experience electromagnetic interaction with each other. These interactions may lead to the collective behaviour of the particles, resulting in microscopic and macroscopic plasma instabilities. These instabilities practically underlie all aspects of achievable plasma performance in tokamaks and determine the principal operational limits for tokamaks: maximum plasma current and plasma pressure, and their gradients (the form of the current and pressure profiles) [Igochine et al., 2015]. This thesis is focused on a macroscopic instability that is commonly observed in all tokamaks - the sawtooth instability.

## 1.2 Sawtooth instability

Sawtooth oscillations are internal periodic relaxation events in a tokamak that lead to a rapid redistribution (i.e., crash) of core temperature and density. The first published report of sawteeth was in 1974 by [von Goeler et al., 1974] in the ST tokamak. They reported sawtooth-like oscillations in the x-ray signal from the core of the discharge, which is primarily a measure of the electron temperature. A sketch of the experimental arrangement and the x-ray signals are shown in figure 1.4a and b, respectively. The basic pattern (figure 1.4c) consists of a slow increase in central temperature and density, followed by the precursor oscillation, and ends with a sudden collapse (crash). The whole process repeats in a periodic manner. Outside the central region, an inverted sawtooth is seen, a slow decay is followed by a fast rise. These oscillations are now seen regularly on all tokamaks and can be observed in many diagnostics including soft X-rays, temperature and density measurements. A theoretical description of the sawtooth phenomenon is given in Chapter 2.

The phenomenon of sawtooth oscillations has been known for decades, leading to the establishment of an extensive knowledge base for the prediction and control of the instability [Igochine et al., 2015]. However, a conclusive theory that explains all the experimental observations of sawtooth oscillations has not yet been proposed and further investigations are required to fill knowledge gaps. The instability is expected to occur (i.e. is accepted in the operational procedure) in large fusion devices of the future such as ITER [Hu et al., 2006]. Even though the temperature and density modulation due to sawteeth are predicted

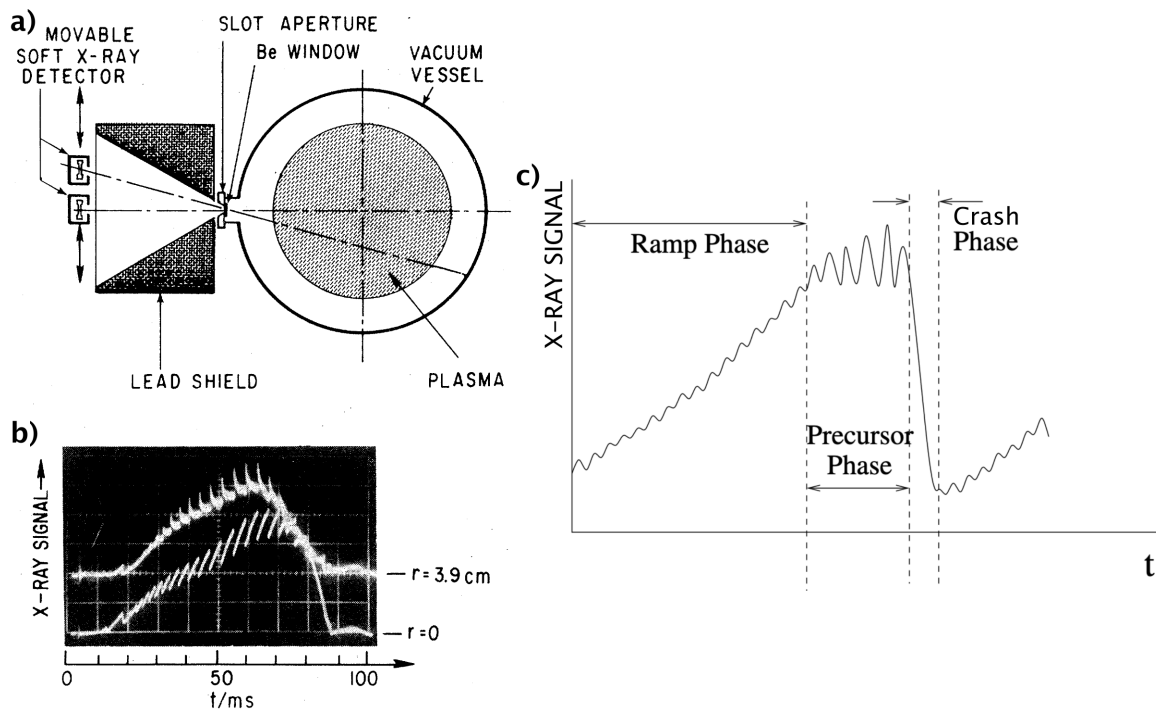


Figure 1.4: Experimental setup (a) and x-ray signals (b) showing sawtooth oscillations in the ST tokamak [von Goeler et al., 1974]. As shown in (c), the sawtooth oscillation typically consists of a ramp phase, then a precursor oscillation followed by the crash phase.

to have a moderate effect on both the plasma stored energy and the neutron production in ITER [Hender et al., 2007], the instability can not be ignored. Sawteeth may seed neoclassical tearing modes (NTM) [Chapman et al., 2010], which may lead to substantial loss of plasma energy and confinement degradation. Furthermore, NTMs may cause plasma disruptions [Zohm, 2015] (sudden loss of plasma temperature and confinement). It is crucial to avoid plasma disruptions in future burning plasma machines because a plasma disruption could destroy the wall components. On the other hand, sawteeth could have a positive contribution to the transport of impurities (as well as helium ash in the future burning plasmas) from the core to the outer regions [Nave et al., 2003], in which case the controlled pacing of crashes would be beneficial for the operation. As the control and prediction of sawteeth are based on theory, the removal of knowledge gaps would result in better simulation and improved performance and safety of the machine operation.

This thesis is focused on the physics of the sawtooth crash phase, which is a magnetic reconnection event. The reconnection is a fundamental process in plasma physics and deserves a separate introduction that is given in the next section.

### 1.3 Magnetic Reconnection

In the plasma physics literature, magnetic reconnection occupies a special place. "There is hardly a term in plasma physics exhibiting more scents, facets and also ambiguities than does magnetic reconnection. It is even used sometimes with a touch of magic." - Biskamp writes in [Biskamp, 1997, pg 127]. "Magnetic reconnection is a marvellous work designed by the nature and played by magnetic field and plasma." - Wang writes in [Wang, 2010]. The basic picture underlying the idea of magnetic reconnection is that two field lines (thin flux tubes, properly speaking) are being carried along with the fluid owing to the property of flux conservation until they come closer together at some point, where, by the effect of finite resistivity, they are cut and reconnected in a different way [Biskamp, 1997, pg 127]. Though it is a localised process, it may fundamentally change the global field line connection as indicated in figure 1.5, permitting fluid motions which would be prohibited in the absence of such local decoupling of fluid and magnetic field.

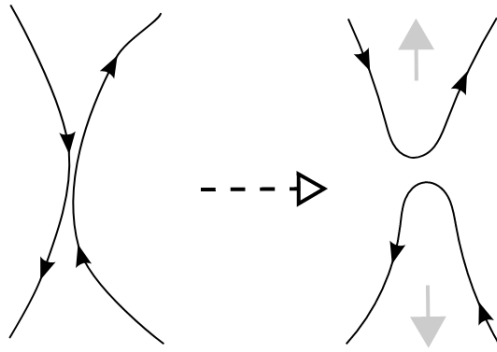


Figure 1.5: Illustration of magnetic reconnection.

In the previous section, the sawtooth cycle has been introduced (figure 1.4c). Now, we shall discuss the physical processes behind this cycle and find out how they are connected with magnetic reconnection phenomenon. In the beginning of the cycle, the temperature profile is relatively flat, and the safety factor value on the magnetic axis is above unity ( $q(0) > 1$ ), as required for ideal stability [Rosenbluth et al., 1973b]. The plasma is heated ohmically (i.e., by collisions that resist the plasma current). Since the current density is peaked on axis, the core of the plasma is preferentially heated, causing the temperature to peak in the core. Since the resistivity decreases with increasing temperature ( $\eta \propto T^{-3/2}$  for collisional plasma), the core becomes a relatively better electrical conductor than the edge, and the current density further peaks at  $r = 0$ , causing  $q(0)$  to decrease ( $q \sim \frac{1}{I_p}$ ). This leads to a further increase in the local heating rate, a further peaking of the temperature, and a further decrease in  $q(0)$ . When  $q(0)$  value drops below unity, a  $q = 1$  magnetic surface forms in the plasma core (shown in figure 1.6: Time 1). A tokamak plasma in a stable equilibrium is considered to consist of toroidally concentric nested flux surfaces on each of which plasma electron temperature  $T_e$  is constant (in figure 1.6b, the electron cyclotron radiation temperature  $T_{rad,e}$  is shown; in the plasma core  $T_{rad,e} \approx T_e$  [Hartfuss

et al., 1997a)], and the plasma is well confined on each flux surface [Wesson and Campbell, 2011]. Because of good parallel thermal conductivity of electrons, the  $T_e(r, z)$  profiles represent the profiles of magnetic surfaces (figure 1.6b and c), where the  $(r, z)$  plane is a poloidal plane. On the  $q = 1$  flux surface, the internal kink instability with poloidal mode number  $m = 1$  and toroidal mode number  $n = 1$  (or  $(1, 1)$  mode) is triggered. The  $(1, 1)$  kink mode is often called a precursor mode. Its nonlinear evolution leads to a crash - a rearrangement of the magnetic flux (magnetic reconnection) and flattening of the plasma temperature. The temperature inside the  $q = 1$  surface exhibits a rapid decrease, while outside that surface it exhibits a rapid increase until the original state with relatively flat temperature is restored (figure 1.6: Time 4). When the field lines are reconfigured, the magnetic and plasma pressure gradient that drives the precursor instability is suddenly reduced and reconnection is terminated.

Magnetic reconnection events are not limited to vacuum chambers of laboratory experiments. More than 99% of all known visible matter in the Universe is in the plasma state [Baumjohann and Treumann, 2012] and magnetic reconnection is one of the fundamental processes that are ubiquitous in all plasmas. Reconnection events are observed or theoretically suggested in: solar flares and coronal mass ejection [Shibata et al., 1995, Golub et al., 1999, Webb and Howard, 2012]; the interaction of the solar wind with the Earth's magnetosphere [Dungey, 1961, Øieroset et al., 2001, Phan et al., 2006, Retinò et al., 2007]; in magnetized accretion disks around black holes [Dal Pino and Lazarian, 2000] and nebulae [Yamada, 2022, pg 130]; and in the magnetosphere of neutron stars [Lyutikov, 2003, Spitkovsky, 2006]. Reconnection is essential for dynamos and the large-scale restructuring known as magnetic self-organization [Zweibel and Yamada, 2009]. The reconnection may be part of the underlying processes generating some of the most energetic particles in the Universe, including the recently discovered fast radio bursts [Zhang, 2020], and may even influence the habitability conditions for life on exoplanets [MacGregor et al., 2021]. Some classical examples of magnetic reconnection are illustrated in figure 1.7.

Magnetic reconnection is a subject of active research for the last fifty years [Yamada et al., 2010, Zweibel and Yamada, 2016, Yamada, 2022]. The research directions can be formulated by the following questions: why is the reconnection rate so fast in semi-collisional and collisionless conductive plasmas? What are the mechanisms of magnetic reconnection in these plasmas? What determines the structure of the reconnection layer? What is the onset of the reconnection? What are the mechanisms of the heating and nonthermal particle acceleration during the reconnection? How is the global plasma system connected with the narrowly localized reconnection region? As a result of the application of two-fluid and kinetic theories during the last 30 years, much theoretical insight has been obtained [Ji et al., 2022, Yamada, 2022], but the posted questions are still not completely answered. A good platform for studying reconnection is provided by laboratory experiments, since it is believed that magnetic reconnection in laboratories has the same physical nature as reconnection in space [Ricci et al., 2004b, Zweibel and Yamada, 2009, Yamada et al., 2010, Ji et al., 2022]. Commonly, numerical simulations based on theories of the reconnection are compared with measurements in laboratory experiments and space observations, and, in this way, the theories are being verified. That way experiment, simulation, and theory may

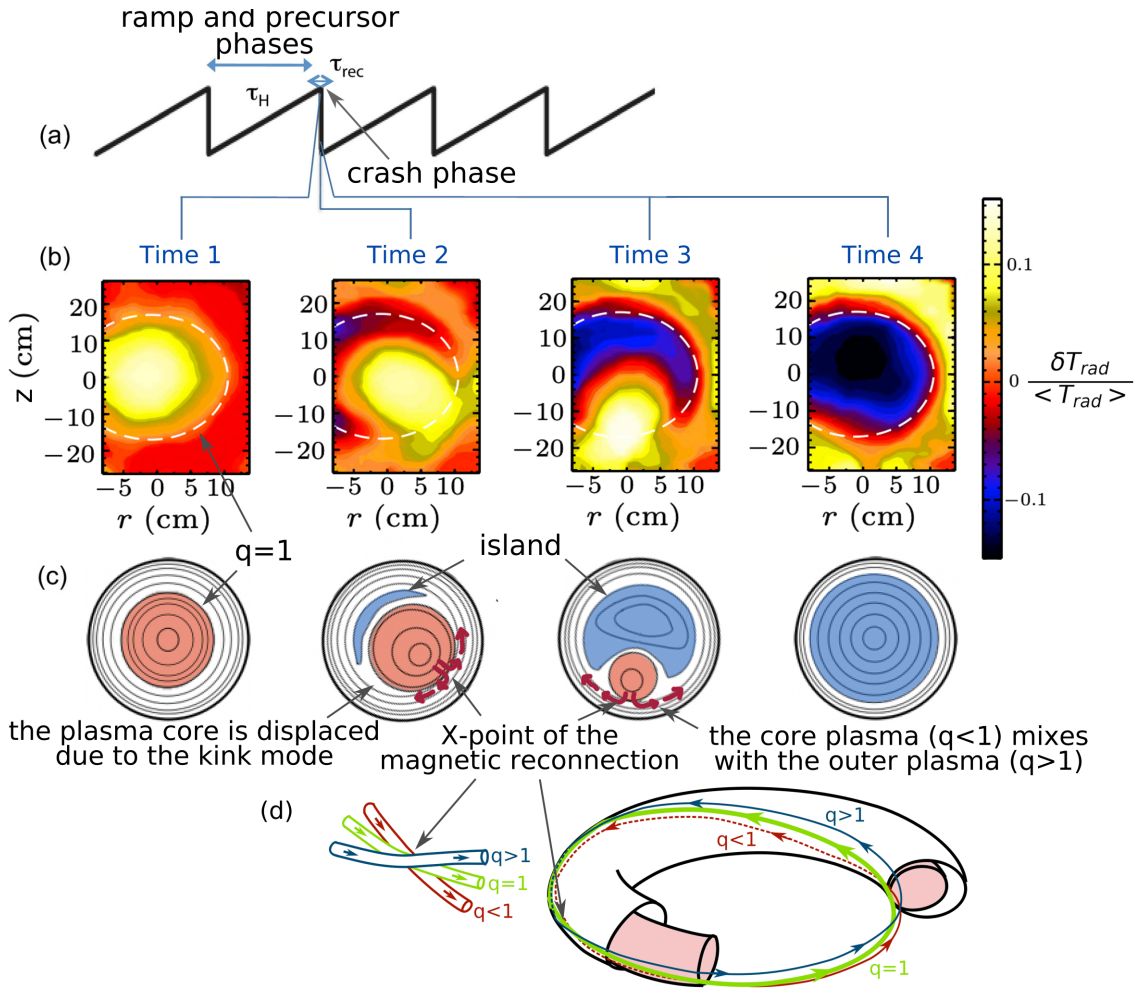


Figure 1.6: Simplified illustration of the core 1D electron cyclotron emission (ECE) signal during several sawtooth periods is shown in (a). One sawtooth period typically consists of a ramp and a precursor phases ( $\sim 100$  ms) followed by the crash phase ( $\sim 100$   $\mu$ s). The 2D ECE measurements [Azam et al., 2015] of one crash phase is shown in (b).  $\delta T_{rad} / \langle T_{rad} \rangle$  is normalized fluctuation of electron radiation temperature. Corresponding illustration of the magnetic flux surfaces and their reconnection is shown in (c). The reconnection X-point is illustrated in (d).

mutually motivate and reinforce one another. Consequently, experimental observations of sawtooth crashes conducted in this thesis contribute to the general research of magnetic reconnection physics.

## 1.4 Outline

After introducing the sawtooth crash and its relevance to the nuclear fusion and magnetic reconnection research, we have arrived at the main focus of this thesis. Two topics of crash

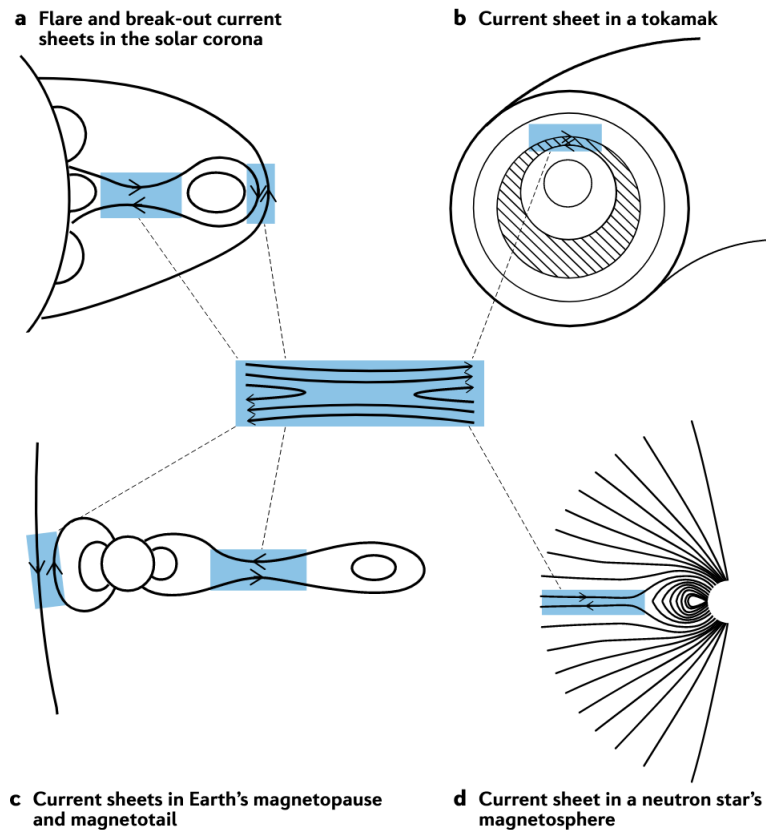


Figure 1.7: Illustrations of the magnetic reconnection in solar flares (a), in a tokamak plasma during a sawtooth crash (b), in the interaction of solar wind with the Earth's magnetosphere (c) and in the magnetosphere of a neutron star (d). The figure is taken from [Ji et al., 2022].

physics are studied. First, the question of whether magnetic reconnection during the crash has global (everywhere along the  $q = 1$  helical magnetic line) or local (only at a particular toroidal location on the  $q = 1$  helical magnetic line) nature is investigated. While most of the research published on sawtooth instability assumes that the crash occurs globally, there are multiple publications that report an observation of helical localisation of the crash [Nagayama et al., 1996, Munsat et al., 2007, Park, 2019]. Clarifying this uncertainty would tell whether one has to use models with well-resolved grid in the toroidal direction or the helically axisymmetric geometry (which is less demanding in terms of computational resources than the former case) is sufficient. Second, the radial velocity of the plasma core during the crash is studied with the electron cyclotron emission imaging (ECEI) diagnostic. These measurements introduce a novel approach for studying magnetic reconnection during sawteeth since the radial velocity characterises the rate of the reconnection. Furthermore, the measurements are compared with nonlinear two-fluid simulation. This comparison addresses the question of whether the two-fluid description is sufficient to correctly model the crash phase or whether additional physical effects are needed.

The thesis is organised as follows: Chapter 2 presents a mathematical model that describes plasma as a fluid (magnetohydrodynamics). Within this model, a theoretical description of the magnetic reconnection and sawtooth physics is given. Chapter 3 introduces the diagnostic and measurement techniques that are used in this thesis. Chapter 4 describes our study on the global and local sawtooth crashes. Chapter 5 presents the experimental and numerical studies of the radial velocity during the crash. Conclusions are drawn in Chapter 6.

# Chapter 2

## Theory

*Grandma told me all about it,  
Told me so I couldn't doubt it,  
How she danced - my Grandma  
danced! -  
Long ago.*

---

Mary Mapes Dodge, *The Minuet*, 1879

In this chapter, we introduce a MagnetoHydroDynamic (MHD) description of plasma - how plasma can be described as a fluid in a magnetic field. Then, we will come to the well-known model of the magnetic reconnection in a single fluid MHD - the Sweet-Parker model. Within the geometry of the Sweet-Parker reconnection, the following effects on the reconnection process are reviewed: two-fluid, plasmoids, turbulence and guide field. Next, we will move on to magnetic reconnection events that happen in tokamaks, where the sawtooth instability will be discussed. The phenomenon and its different phases (precursor, crash and post-cursor) are described. The main attention is given to the crash phase of the instability, which is the focus of research in this thesis.

### 2.1 MHD

Magnetohydrodynamics, or MHD, is a theoretical way of describing the statics and dynamics of electrically conducting fluids in a magnetic field. MHD is the simplest mathematical model of plasma, where plasma is approximated as a conducting fluid (or two conducting fluids of electrons and ions). This approximation of plasma substitutes microscopic variables (particle velocities, particle trajectories, etc.) by macroscopic ones (such as mass density, fluid velocity, and pressure), making the material properties of the fluid independent of the physical size of the sample. Even though MHD description completely ignores that the plasma is made of individual ions and electrons and that they might be so hot that collisions between particles are relatively rare events, nonetheless, it is a fact that MHD

provides a remarkably accurate description of the low-frequency, long-wavelength dynamics of real plasmas [Troyon et al., 1988, Bondeson et al., 1992, Hender et al., 2007, Wesson and Campbell, 2011, Zohm, 2015, Igochine et al., 2015].

A closed set of equations defining two-fluid MHD model is summarized below (with  $\alpha = e$  for the electrons and  $\alpha = i$  for the ions)[Kulsrud, 1983][Inan and Golkowski, 2010, pg 107][Stacey, 2012, pg 87][Zohm, 2015, pg 1]:

$$\text{continuity} : \frac{\partial n_\alpha}{\partial t} + \nabla \cdot (n_\alpha \mathbf{u}_\alpha) = 0 \quad (2.1)$$

$$\begin{aligned} \text{momentum balance} : m_\alpha \frac{\partial (n_\alpha \mathbf{u}_\alpha)}{\partial t} = & -\nabla \cdot (m_\alpha n_\alpha \mathbf{u}_\alpha \otimes \mathbf{u}_\alpha + \bar{\mathbf{P}}_\alpha) \\ & + n_\alpha q_\alpha (\mathbf{E} + \mathbf{u}_\alpha \times \mathbf{B}) + \mathbf{R}_{\alpha\beta} \end{aligned} \quad (2.2)$$

$$\text{Ohm} : \mathbf{E} + \mathbf{v} \times \mathbf{B} = \mathbf{R}\mathbf{D} \quad (2.3)$$

$$\text{energy} : \frac{d}{dt} \left( \frac{p_\alpha}{\rho_\alpha^{\gamma_\alpha}} \right) = 0 \quad (2.4)$$

$$\text{Faraday} : \nabla \times \mathbf{E} = -\frac{\partial \mathbf{B}}{\partial t} \quad (2.5)$$

$$\text{Ampere} : \nabla \times \mathbf{B} = \mu_0 \mathbf{J} \quad (2.6)$$

$$\text{no magnetic monopoles} : \nabla \cdot \mathbf{B} = 0 \quad (2.7)$$

, where  $n$  is the fluid density,  $u$  is the average fluid velocity,  $m$  is the mass,  $q$  is the electrical charge,  $\bar{\mathbf{P}}$  is the pressure tensor,  $\mathbf{E}$  is the electric field,  $\mathbf{B}$  is the magnetic field,  $\mathbf{R}_{\alpha\beta}$  is the friction force between  $\alpha$  and  $\beta$  species,  $\mathbf{v}$  is the centre of mass fluid velocity ( $\mathbf{v} = \frac{m_i n_i \mathbf{u}_i + m_e n_e \mathbf{u}_e}{m_i n_i + m_e n_e}$ ),  $\mathbf{R}\mathbf{D}$  is the resistive-diffusive terms in Ohm's law (these terms will be introduced in the next section),  $\mathbf{J}$  is the plasma current,  $\mu_0$  is the vacuum permeability,  $\gamma_\alpha$  is the adiabatic coefficient. The MHD equations 2.1-2.4 are derived clearly in [Krall and Trivelpiece, 1973, pg 79], [Goedbloed et al., 2004, pg 48], [Inan and Golkowski, 2010, pg 84] and [Pert, 2021, pg 149].

The two-fluid set of equations 2.1-2.7 can be further reduced to a one-fluid MHD description of plasma [Zohm, 2015, pg 4] or what is usually called just the MHD model. The one-fluid approach is preferable for short-time hydrodynamic effects in which nonideal effects play a minor role. Its great advantage is that its equations are considerably simpler to handle than the two-fluid approach. Finally, it can be used in longer-time problems to get an idea of at least some of the plasma behaviour. The two-fluid equations are more accurate and necessary for any precision in the discussion of phenomena where plasma dissipation is involved.

Application of the MHD models in Nuclear Fusion research [Balescu, 1988, pg 313]:

- Equilibrium theory [Zohm, 2015, pg 15]. One tries to find an "equilibrium" state in which all hydrodynamic quantities are time-independent. The problem consists of

finding a magnetic field and a plasma pressure satisfying the mechanical equilibrium condition derived from the MHD force balance equation. For instance, in a tokamak within the one-fluid approach and sufficiently small plasma flow velocities, the equilibrium equations has a form of:  $\nabla \mathbf{p} = \mathbf{J} \times \mathbf{B}$ .

- Stability theory [Zohm, 2015, pg 43]. When equilibrium is found, its stability against small perturbations must be studied. There is no universally stable magnetic field confinement: the plasmas are plagued with an enormous variety of instabilities. The identification of the instabilities, the calculation of their thresholds and growth rates, and the evolution of an initially growing perturbation and its saturation are the key problems in the stability theory.
- Dynamics of MHD instabilities [Goedbloed et al., 2010] (sawtooth and tearing modes and magnetic reconnection during these two modes; kink modes, edge localized modes, disruptions). The theoretical and numerical studies and their comparison with the experimental observations allow us to validate the used models and understand the physics behind the observed processes.

Apart from nuclear fusion, the MHD description of plasmas is widely used in the astrophysical and space research [Somov, 2012a, Somov, 2012b, Somov, 2013]. The examples of the phenomena that are described with MHD models are: flares on the Sun and other stars, coronal mass ejections, interaction of solar wind with Earth's magnetosphere, accretion disks of stars, astrophysical jets, interplanetary MHD shock waves, the plasma motion in the interior of stars, nuclei of active galaxies and quasars.

## 2.2 Magnetic reconnection

In this section, we study magnetic reconnection within the MHD (single- and two-fluid) framework.

### 2.2.1 Vacuum

Magnetic reconnection occurs at the boundary of two regions with opposite (or partially) opposite field directions. To get an idea of what it is, we consider a simple example: two parallel wires which contain identical currents flowing into the page in a vacuum medium (shown in figure 2.1). When we move the wires toward each other, the fields of the wires will meet in the center between them and form an X-shape field line. The centre of the X is the neutral point of the magnetic field. At this point, the field line of the same colour can break and reconnect as shown in the figure 2.1. Such a process is termed reconnection of field lines. The number of field lines (i.e. the magnetic flux) pointing toward are equal to the number of field lines pointing away from the neutral point. Thus, the breaking and reconnecting of magnetic lines comply with  $\nabla \cdot \mathbf{B} = 0$ .

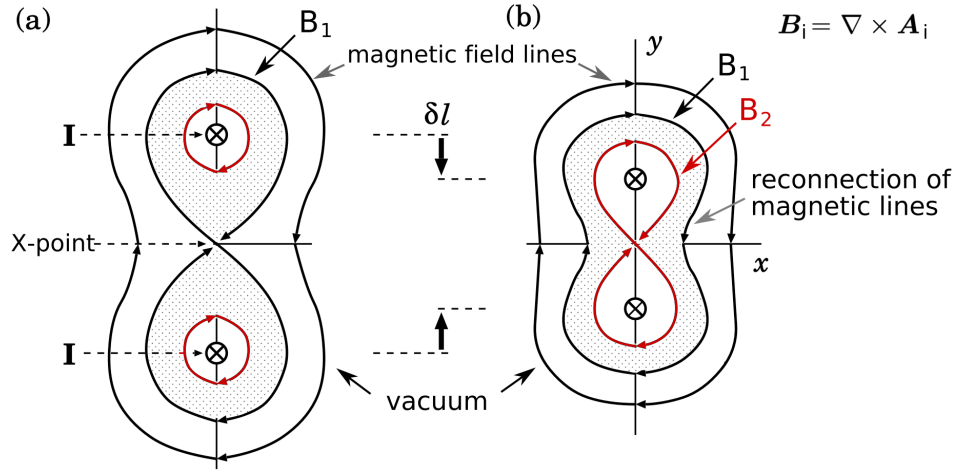


Figure 2.1: The magnetic field lines of two parallel currents  $I$  in a vacuum: (a) the initial state; (b) the final state after they have been drawn nearer by a driven displacement  $\delta l$ .  $B$  is the magnetic field and the  $A$  is the vector potential of the magnetic field. The figure is adapted from [Somov, 2012b, pg 7].

This simple example of the two wires also illustrates that reconnection is inevitably associated with electric field generation. This electric field is inductive, as can be shown through the following formulae [Somov, 2012b, pg 8]:  $\mathbf{E} = -\frac{1}{c} \frac{\partial \mathbf{A}}{\partial t} \approx -\frac{1}{c} \frac{A_2 - A_1}{\delta t} \mathbf{e}_z$ , where  $\mathbf{A}$  is the vector potential of magnetic field  $\mathbf{B} = \nabla \times \mathbf{A}$ ; and  $\delta t$  is the characteristic time of the reconnection process shown in figure 2.1. The generated electric field is directed along the  $z$  axis (out of the paper).

Reconnection in a vacuum is a real physical process: magnetic field lines move to an X-type neutral point and reconnect in it. During this process, the electric field is induced and can accelerate a charged particle in the vicinity of the neutral point.

### 2.2.2 Perfectly conducting plasma

The process of magnetic reconnection changes when perfectly conducting (or ideal plasma) is added between the two wires as shown in figure 2.2. Since the plasma is a perfect conductor, the electric field in the plasma frame is zero. Any presence of an internal electric field will be quickly counteracted by motions of the charged particles. According to Faraday's law (equation 2.5), when the electric field is zero, there must be no change in a magnetic field. This means the magnetic field is frozen in the plasma. When a plasma moves, the magnetic field has to move along. The plasma that co-moves with the magnetic field is said to be under "frozen-in" condition. We call the plasma that is perfectly under frozen-in conditions "ideal" MHD plasma.

Under the frozen-in condition, the electric field zeroes only in the plasma frame. If an element of plasma moves with the velocity  $\mathbf{u}$  as observed, in the lab frame, the electric field of the plasma element  $\mathbf{E}$  can be thought to come into existence purely by means of

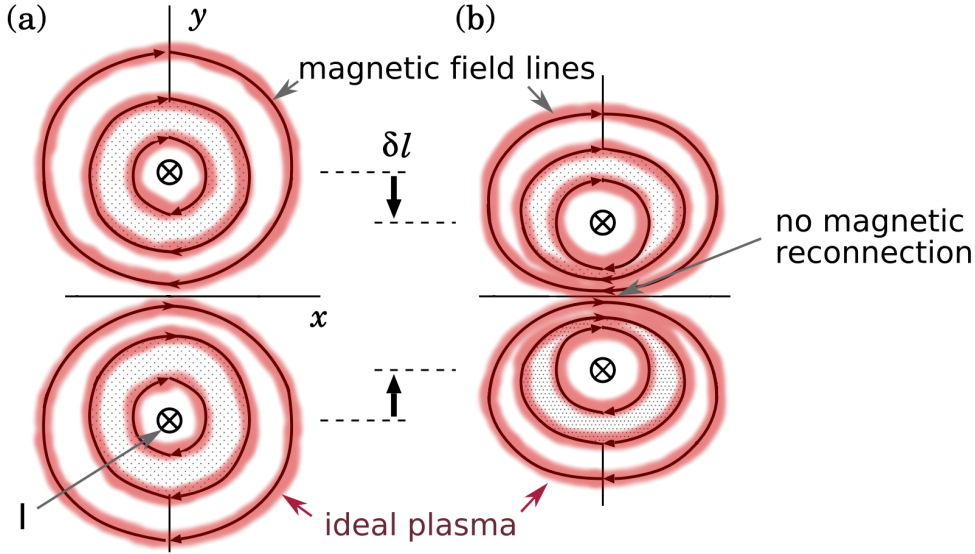


Figure 2.2: The magnetic field lines of two parallel currents  $I$  with ideal plasma confined along the magnetic field: (a) the initial state; (b) the final state after they have been drawn nearer by a driven displacement  $\delta l$ . There is no magnetic reconnection due to the flux conservation in ideal plasma. The figure is adapted from [Somov, 2012b, pg 12].

the frame transformation, which follows Ohm's law for ideal plasma (equation 2.3 with resistive term set to zero):

$$\mathbf{E} = -\mathbf{u} \times \mathbf{B} \quad (2.8)$$

Using a vector identity, this equation can also be rearranged to:

$$\mathbf{u}_{\perp} = -\frac{\mathbf{E} \times \mathbf{B}}{B^2} \quad (2.9)$$

where  $\mathbf{u}_{\perp}$  is the plasma velocity in the direction perpendicular to the magnetic field. In ideal plasma, the perpendicular velocity of a plasma flux is solely governed by  $\mathbf{E} \times \mathbf{B}$  drift (the guiding centers of ions and electrons co-move with the same velocity in the drift motion).

An equivalent formulation of frozen-in condition is magnetic flux conservation in ideal plasma (the magnetic flux  $\Phi$  through any closed loop following the fluid motion remains constant in time:  $\frac{\partial \Phi}{\partial t} + \mathbf{u} \cdot \nabla \Phi = \oint (\mathbf{E} + \mathbf{u} \times \mathbf{B}) dl = 0$  if  $\eta = 0$ ) [Zohm, 2015, pg 8]. An important consequence of magnetic flux conservation is that two magnetic flux tubes in plasma do not merge. A flux tube is defined as a tube-like object that has no magnetic field perpendicular to its side surface and equal magnetic fluxes coming in and going out through its end surfaces. If they can merge into one, then the amount of the magnetic flux from the two tubes can combine. This breaks the conservation of the flux within each tube. The idea is illustrated in figure 2.3. The motion of the ideal plasma is constrained to not change the topology of the flux tubes. Thus, magnetic reconnection is impossible in perfectly conducting plasma.

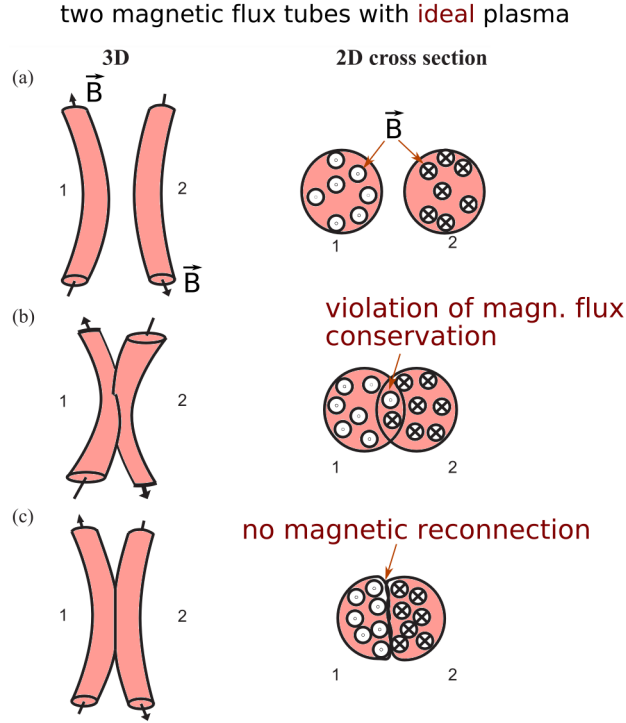


Figure 2.3: Interactions of two flux tubes illustrated in both 3D pictures and top-view 2D cross-section. (a) Two flux tubes away from each other. Tube 1 has 7 flux units pointed out of the page (from 2D view). Tube 2 has 7 units pointed into the page. (b) Two flux tubes are merging. The net number of flux contained in each tube is not conserved. Tubes 1 and 2 now have the net flux of 6 in the out of the page and into the page directions respectively. (c) From the viewpoint of the frozen-in theorem, two flux tubes can be pressed toward each other but cannot merge. Without merging, each tube conserves the amount of flux no matter how it is pressed. The figure is adapted from [Malakit, 2012].

### 2.2.3 Resistive plasma

As we have learned, in the ideal MHD the connectivity of plasma elements cannot be changed. Any form of magnetic reconnection requires non-ideal or resistive-diffusive terms ( $RD$ ) in the Ohm's law (equation 2.3). The latter can be demonstrated through its simplest resistive form (only the electron-ion collisions term is considered):

$$\mathbf{E} + \mathbf{v} \times \mathbf{B} = \eta \mathbf{j} \quad (2.10)$$

, where  $\eta$  is the plasma resistivity. Combining with

$$\frac{\partial \mathbf{B}}{\partial t} = \nabla \times \mathbf{E} \quad (2.11)$$

yields

$$\frac{\partial \mathbf{B}}{\partial t} = \nabla \times (\mathbf{v} \times \mathbf{B}) + \frac{\eta}{\mu_0} \nabla^2 \mathbf{B} \quad (2.12)$$

The last term gives a diffusion of the magnetic field over the so-called resistive timescale  $\tau_R = \mu_0 L^2 / \eta$  ( $L$  is the characteristic length of the reconnection region).

All of the resistive terms are included in the so-called **generalized Ohm's law**, which can be written as [Cozzani, 2020, pg 13]:

$$\boxed{\underbrace{\mathbf{E} + \mathbf{u}_i \times \mathbf{B}}_{\text{ideal}} = \underbrace{\frac{\eta \mathbf{j}}{ne}}_{\text{electron-ion collisions}} + \underbrace{\frac{\mathbf{j} \times \mathbf{B}}{ne}}_{\text{Hall}} - \underbrace{\frac{1}{ne} \nabla \cdot \overline{\mathbf{P}}_e}_{\text{electron pressure}} + \underbrace{\frac{m_e}{ne^2} \nabla \cdot \left( \mathbf{j} \mathbf{u}_i + \mathbf{u}_i \mathbf{j} - \frac{\mathbf{j} \mathbf{j}}{ne} \right)}_{\text{electron inertia}} + \frac{m_e}{ne^2} \frac{\partial \mathbf{j}}{\partial t}} \quad (2.13)$$

where  $m_e$  is the electron mass. During the derivation quasi-neutrality  $n \approx n_i \approx n_e$  is assumed, and the  $1 + \frac{m_e}{m_i} \approx 1$  and  $\frac{m_e}{m_i} |\mathbf{u}_i| \ll |\mathbf{u}_e|$  simplifications are used. Other forms of the generalized Ohm's law can be found in [Krall and Trivelpiece, 1973, pg 91], [Priest and Forbes, 2000, pg 41], [Boyd et al., 2003, pg 65], [Inan and Golkowski, 2010, pg 120] and [Gurnett and Bhattacharjee, 2017, pg 189].

As can be seen from equation 2.13, there are four resistive terms: electron-ion collisions, Hall, the electron pressure and the electron inertia. We compare the resistive terms with the ideal term in order to understand their contribution to the electric field  $E$  value (if for a given resistive term  $\left| \frac{\text{resistive term}}{\mathbf{u}_i \times \mathbf{B}} \right| \ll 1$ , then the contribution of this term can be neglected) [Priest and Forbes, 2000, pg 41] [Stacey, 2012, pg 93] [Cozzani, 2020, pg 15]:

$$\text{electron - ion collisions : } \left| \frac{\eta \mathbf{j}}{\mathbf{u}_i \times \mathbf{B}} \right| \sim \beta \frac{\lambda_e^2 \lambda_i^2 v_A^2}{L^2 \lambda_{mfp}^2 V_0^2} \quad (2.14)$$

$$\text{Hall : } \left| \frac{\mathbf{j} \times \mathbf{B} / nec}{\mathbf{u}_i \times \mathbf{B}} \right| \sim \frac{\lambda_i^2 v_A^2}{V_0^2 L^2} \quad (2.15)$$

$$\text{electron pressure : } \left| \frac{\nabla \cdot \overline{\mathbf{P}}_e / ne}{\mathbf{u}_i \times \mathbf{B}} \right| \sim \beta \frac{\rho_i^2 v_A^2}{L^2 V_0^2} \quad (2.16)$$

$$\text{electron inertia : } \left| \frac{\frac{m_e}{ne^2} \frac{\partial \mathbf{j}}{\partial t}}{\mathbf{u}_i \times \mathbf{B}} \right| \sim \left| \frac{\frac{m_e}{ne^2} \nabla \cdot \left( \mathbf{j} \mathbf{u}_i + \mathbf{u}_i \mathbf{j} - \frac{\mathbf{j} \mathbf{j}}{ne} \right)}{\mathbf{u}_i \times \mathbf{B}} \right| \sim \frac{\lambda_e^2}{L^2} \quad (2.17)$$

where  $V_0$  is the characteristic velocity of the plasma fluid;  $\lambda_e$  is the electron-inertial length or skin-depth;  $\lambda_i$  is the ion-inertial length or skin-depth;  $v_A$  is the Alfvén velocity;  $\beta$  is the plasma-beta parameter;  $\rho_i$  the ion-gyro radius (or ion Larmor radius),  $\lambda_{mfp}$  is the mean-free path for electron-ion collisions.  $L$  corresponds to the characteristic scale of interest (it allows to understand at which scale length a given resistive term becomes important and cannot be neglected) [Priest and Forbes, 2000, pg 42]:

$$L_{\text{inertia}} = \lambda_e = \frac{c}{\omega_{pe}} \approx 5.3 \cdot 10^6 (n [m^{-3}])^{-1/2} [m] \quad (2.18)$$

where  $\omega_{pe}$  is the electron plasma frequency.

$$L_{Hall} = \frac{\lambda_i}{M} = \frac{c}{\omega_{pe} M} \approx 2.27 \cdot 10^8 \left( \frac{\tilde{\mu}}{n[m^{-3}]} \right)^{1/2} \frac{1}{M} [m] \quad (2.19)$$

, where  $\tilde{\mu} = \bar{m}/m_p$  is the mean atomic weight,  $\omega_{pe}$  is the electron plasma frequency.  $M$  is the Alfvénic Mach number:

$$M = \frac{V_0}{u_A} = \frac{V_0[m/s] \cdot \sqrt{n[m^{-3}]}}{2.18 \cdot 10^{12} \cdot B_0[G]} \quad (2.20)$$

$$L_{pressure} = \frac{\beta^{1/2} \rho_i [m]}{M} \quad (2.21)$$

where

$$\beta = nk_B T \left( \frac{2\mu}{B_0^2} \right) \approx 3.5 \cdot 10^{-29} \frac{n[m^{-3}] \cdot T[K]}{B_0^2} \quad (2.22)$$

and

$$\rho_i = \frac{(k_B T_i m_p \tilde{\mu})^{1/2}}{e B_0} \approx 9.5 \cdot 10^{-7} \frac{(T_i[K] \cdot \tilde{\mu})^{1/2}}{B_0[G]} [m] \quad (2.23)$$

$$L_{collisions} = \beta^{1/2} \frac{\lambda_e [m] \cdot \lambda_i [m]}{\lambda_{mfp} [m]} \frac{1}{M} [m] \quad (2.24)$$

with  $\lambda_{mfp}$  is the mean-free path for electron-ion collisions [Chen, 2016, pg 415]:

$$\lambda_{mfp} = 3(2\pi)^{3/2} \frac{(k_B T_e \epsilon_0)^2}{n e^4 \ln \Lambda} \approx 1.1 \cdot 10^9 \frac{(T_e[K])^2}{n[m^{-3}] \cdot \ln \Lambda} [m] \quad (2.25)$$

, where  $\ln \Lambda$  is the Coloumb logarithm that can be estimated as [Priest and Forbes, 2000, pg 14]:

$$\ln \Lambda = \begin{cases} 16.3 + \frac{3}{2} \ln(T[K]) - \frac{1}{2} \ln(n[m^{-3}]), & T < 4.2 \cdot 10^5 K, \\ 22.8 + \ln(T[K]) - \frac{1}{2} \ln(n[m^{-3}]), & T > 4.2 \cdot 10^5 K. \end{cases} \quad (2.26)$$

The estimated scale-lengths parameters for the core plasma in ASDEX Upgrade is presented in table 2.1 (the calculations are shown in appendix A).

Finally, it is worth mentioning that the electron-ion collision, electron pressure and inertia terms contribute to the reconnection electric field  $E$ , which can break the frozen flux constraint, but the Hall term does not if the plasma density is homogeneous as shown in [Baumjohann and Treumann, 2012, pg 371].

## 2.2.4 Types of reconnection in a tokamak plasma

As we just learned, magnetic reconnection occurs within the MHD description only when resistive-diffusive terms in the generalized Ohm's law are present. At first sight, we might

| Parameter                            | Value                      |
|--------------------------------------|----------------------------|
| $L$                                  | 1.0 <i>m</i>               |
| $\lambda_D$                          | 53 $\mu m$                 |
| $\lambda_e$                          | 0.6 <i>mm</i>              |
| $\lambda_i$                          | 3.6 <i>cm</i>              |
| $\rho_e$                             | 60 $\mu m$                 |
| $\rho_i$                             | 4 <i>mm</i>                |
| $\rho_s$                             | 4 <i>mm</i>                |
| $\lambda_{mfp}$                      | 1.6 <i>km</i>              |
| $L_{inertia}$                        | 0.6 <i>mm</i>              |
| $L_{Hall, Sweet-Parker}$             | 0.5 <i>m</i>               |
| $L_{Hall, strong\ guide\ field}$     | 5.7 <i>cm</i>              |
| $L_{pressure, Sweet-Parker}$         | 7 <i>cm</i>                |
| $L_{pressure, strong\ guide\ field}$ | 7.4 <i>mm</i>              |
| $L_{collisions}$                     | $3 \cdot 10^{-8}$ <i>m</i> |

Table 2.1: Characteristic scale-lengths of the core plasma in ASDEX Upgrade.

expect the reconnection process to be slow, as it is in resistive diffusion. However, reconnection occurs much more rapidly if it is concentrated in a small region. This fast reconnection is the focus of our research. In general, there are two types of reconnection that occur in tokamak plasmas:

1. **Tearing mode** [Taylor and Newton, 2015, pg 23] (figure 2.4a) is resistive instability that occur in thin plasma layers in which resistivity is dominant no matter how small it may be. In these small layers, the magnetic field is able to slip rapidly through the plasma. The result is that, if one starts out with a one-dimensional sheet with straight field lines and then makes a perturbation such as the one in figure 2.4a (current perturbation directed into the paper), the resulting forces are such as to make the perturbation grow. The magnetic tension tends to pull the new loops of field up and down away from the X-points, while the magnetic pressure gradient tends to push plasma in from the side towards the X-points. Also, the field lines at the sides are curved and so possess a restoring magnetic tension force, which is minimized for long wavelengths. In other words, the fewer X-points a tearing mode has the less is restoring force of the magnetic tension acted on the mode and the easier for the mode to grow. The tearing mode is driven by the free energy stored in plasma pressure and magnetic field.
2. **Forced reconnection** (or driven) [Taylor and Newton, 2015, pg 26] (figure 2.4b) is magnetic reconnection that is driven by plasma flows or imposed on the reconnection region.

More material on tearing modes and their evolution is given [Priest and Forbes, 2000, pg 177][Schnack, 2009, pg 205][Zohm, 2015, pg 141]. This thesis is focused on the forced

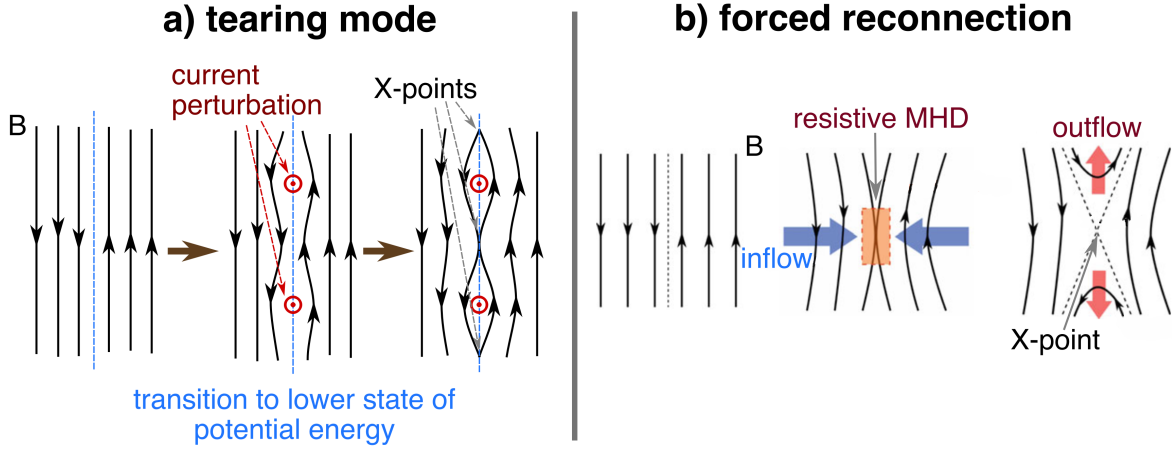


Figure 2.4: Illustration of tearing mode (a) and forced (b) reconnections.

reconnection type.

### 2.2.5 Sweet-Parker model

An idealised form of forced reconnection is Sweet-Parker model [Parker, 1957, Sweet, 1958][Priest and Forbes, 2000, pg 120]. The reconnection is steady-state and based on single-fluid MHD of collisional plasma (electron-ion collisional term is dominant in the generalized Ohm's law:  $\mathbf{E} + \mathbf{u} \times \mathbf{B} = \eta \mathbf{J}$ ) [Schnack, 2009, pg 197][Taylor and Newton, 2015, pg 26]. The model represents plasma flow through an X-point of a two dimensional magnetic field, as illustrated in figure 2.5. The antiparallel reconnecting fields are forced towards X-point by flows in the  $\pm y$  direction, reconnect, and then flow outwards along the  $\pm x$  directions. The forced inflows cause "flattening" of the X-point to eventually form a current sheet of thickness  $\delta$  and length  $\Delta$ , as indicated in figure 2.5. The field  $B$  changes direction across this current sheet.

The fluid enters the current sheet at velocity  $u_{in}$ . This is the rate at which magnetic flux enters the inner layer. This magnetic flux reconnects within the resistive layer of the current sheet. The fluid then flows out along the current sheet. No more fluid can enter the layer and carry in magnetic flux until the previous bit of fluid leaves. The ratio of the inflow velocity to the outflow velocity,  $u_{in}/u_{out}$ , therefore determines the rate at which magnetic flux can be reconnected. The electric field  $E_z$  in the current sheet points in the  $z$ -direction.

From the Ohm's law we have the inflow velocity:

$$u_{in} \sim \frac{\eta}{\mu_0 \delta} \quad (2.27)$$

The equation 2.27 means that in a steady-state the plasma must carry the field lines at the same speed as they are trying to diffuse outward. Pressure balance:

$$\rho \frac{u_{out}^2}{2} \sim \frac{B_0^2}{2\mu_0} \quad (2.28)$$

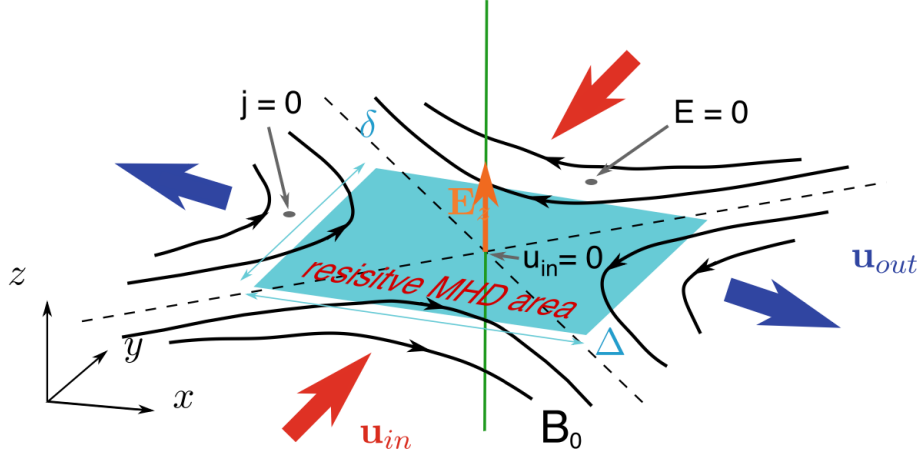


Figure 2.5: Sweet-Parker problem. The diffusion region is represented with the light blue rectangle. The area that surrounds this diffusion region is described by the ideal MHD. Reconnection electric field  $E$ , magnetic field  $B_0$ , and in/outflow velocities  $u_{in/out}$  are shown in orange, black, and red/blue respectively. The figure is adapted from [Cozzani, 2020].

gives for the outflow:

$$u_{out} \sim \frac{B_0}{\sqrt{\mu_0 \rho}} = V_{A,in} \quad (2.29)$$

, where  $V_{A,in}$  is the Alfvén speed at the inflow. The equation 2.29 means that the magnetic force accelerates the plasma to the Alfvén speed. Mass conservation requires:

$$u_{in} \Delta \sim u_{out} \delta \quad (2.30)$$

Consequently, by multiplying 2.30 by  $u_{in} \Delta^2$  and using 2.27 and 2.29 we obtain:

$$u_{in}^2 \sim \frac{\Delta^2}{\tau_R \tau_A} \quad (2.31)$$

, where  $\tau_A = \frac{\delta}{v_A}$  is the Alfvén time;  $\tau_R = \frac{\mu_0 \Delta^2}{\eta}$  is the resistive time.

Finally, the reconnection rate of the Sweet-Parker model is (derived from the equations 2.29, 2.30 and 2.31):

$$\boxed{\frac{u_{in}}{u_{out}} = \frac{\delta}{\Delta} = \frac{1}{\sqrt{S}}} \quad (2.32)$$

, where  $S = \tau_R / \tau_A$  is the Lundquist number. The reconnection rate depends on the aspect ratio  $\delta / \Delta$  of the diffusion region, which in turn depends on the microphysics in the resistive MHD region.

A simple calculation of the energy conversion in the Sweet-Parker model gives:

$$\frac{\text{Kinetic energy out}}{\text{Electromagnetic energy in}} = \frac{\rho v_A^2 / 2 \cdot 2 v_A \delta}{E \times B_0 / 4\pi \cdot 2\Delta} = \frac{1}{2} \quad (2.33)$$

where the condition  $E = u_{in} \times B$  is used in the expression for the Poynting flux in the denominator. Equation 2.33 shows that half of the incoming magnetic energy is converted to the Alfvénic outflow jets during magnetic reconnection. The other half goes to the thermal energy of the plasma inside the reconnection layer due to the Ohmic heating.

It has been shown that the Sweet-Parker model well describes the magnetic reconnection in collisional plasmas at modest Lundquist numbers ( $S \leq 10^4$ ) [Yamada et al., 2006, Kuritsyn et al., 2006, Yamada and Ji, 2010]. However, at higher  $S$  numbers (for example,  $S$  is  $10^4 - 10^8$  in laboratory fusion plasmas,  $10^{10} - 10^{14}$  in solar flares, and  $10^{15} - 10^{20}$  in the interstellar medium of the Galaxy) and lower collisionality, current sheets begin to develop structures comparable to the ion inertial length or ion sound gyroradius and the mean free path of electron (or both ions and electrons) becomes much larger than the size of the reconnection area. Electrons and ions begin to behave differently and this behaviour cannot be correctly described with the single-fluid MHD. Consequently, the Sweet-Parker model does not provide a quantitatively correct answer to describe the observed reconnection rate in plasmas with  $S > 10^4$ . For example, the model predicts the reconnection time  $\sim 2$  months for solar flares and  $\sim 1 - 10$  ms for sawtooth crashes, whereas the observed numbers are  $\sim 15 - 60$  min and  $\sim 0.1$  ms for solar flare and sawtooth reconnections, respectively. To describe these much faster reconnection rates, two-fluid and/or kinetic physics is required.

### 2.2.6 Beyond Sweet-Parker

In this section, we go beyond the idealized, classical, single quasi-stationary X-line geometry described with single-fluid MHD. We discuss physical effects that can only be seen when a two-fluid or kinetic description of the plasma is employed. These effects allow us to explain the fast reconnection rates (much faster than predicted by the Sweet-Parker model) observed in laboratory and space plasmas.

#### — Two-fluid terms in generalized Ohm’s law —

Generally, in collisional plasma, only the electron-ion collision term acts in the generalized Ohm’s law (equation 2.13) as its contribution is much larger than the contribution from other terms. When collisionality is reduced and the Sweet-Parker layer (or the diffusion region) becomes thinner than the ion skin depth (the ratio of the Sweet-Parker layer thickness to the ion skin depth  $\approx 0.2\sqrt{L/\lambda}$ , where  $\lambda$  is the mean free path,  $L$  is the global length of the current layer [Yamada et al., 2006]), the plasma transits to the semi-collisional or collisionless regimes, where the motion of the ions and electrons decouple and the contribution of the Hall, electron pressure and inertia terms have to be included since these terms become comparable to the collisional one. These terms produce physical effects, which are called two-fluid or kinetic effects <sup>1</sup>, which does not exist in the collisional

<sup>1</sup>The name "kinetic effects" originates from the description of physics on the ion and/or electron characteristic length scale (also called kinetic length scale) on which the two-fluid physics begins to play the major role. However, this term might be misleading, since these kinetic effects are described within the

single-fluid description of the plasma.

In the following, in order to understand the physics behind the two-fluid dynamics, the effect of each two-fluid term in Ohm's law on the reconnection process is discussed separately (though, in a nonlinear system, which magnetic reconnection is, the final physical process does not have to consist from the sum of the isolated contribution of each two-fluid term):

- Hall term (acts on the ion skin depth  $\lambda_i = c/\omega_{pi}$  scale): ions approaching the diffusion region are brought to a halt over a distance comparable to the ion skin depth, while electrons remain frozen-in to the field until they reach a distance comparable to electron skin depth. This creates a charge separation and Hall currents generation [Sonnerup, 1988], which leads to the generation of the out-of-plane magnetic field, which has a quadrupole structure. This quadrupole field generation is explained by [Uzdensky and Kulsrud, 2006] as follows. Consider an incoming flux tube as it moves deeper and deeper into the (ion-scale) reconnection region toward the X-point 2.6a. The poloidal magnetic field in the central part of the tube near  $x = 0$  has to decrease, and hence the volume of this central part has to expand. As electrons are tightly coupled to magnetic field lines, this expansion would lead to a drop in electron density. However, the ions are not magnetized and their density does not decrease. Therefore, as almost perfect charge neutrality is to be maintained, a very small poloidal electric field arises and it immediately pulls the electrons along the field lines inward from the outer parts of the flux tube into this central region. Owing to the very large mobility of electrons along the field, this parallel electric field is negligibly small. As a result, we get a strong inflow of electrons along the poloidal magnetic field in the upstream region (2.6b). This inflow rapidly accelerates as the field line approaches the separatrix, because of the rapidly increasing rate of flux-tube expansion near the X-point. In the downstream region, the direction of the electron flow reverses: as a newly reconnected field line moves away from the X-point, the volume of its central part decreases and so the electrons are squeezed out and flow rapidly outward along the field (2.6c). As the field line moves further away, this outflow gradually decelerates. The resulting overall picture of the electron flow is shown in 2.6c. There is a poloidal electric current associated with the flow of electrons and by Ampere's law this current generates a quadrupole toroidal magnetic field concentrated along the separatrix (2.6d).

If the plasma is homogenous, the sole Hall term does not produce the reconnection and an additional dissipative term is needed to allow the reconnection [Baumjohann and Treumann, 2012, pg 371]. This has been numerically confirmed by [Andrés et al., 2014].

The Hall term accelerates the magnetic reconnection rate (in comparison to purely collisional Sweet-Parker) [Yamada et al., 2006, Yamada et al., 2010] since the term (i) allows large electric field generation in the X-point region and (ii) increases the

---

two-fluid MHD framework without involving the kinetic theory.

### The Hall term

$$\underbrace{E + u_i \times B}_{\text{ideal}} = \underbrace{\frac{j \times B}{ne}}_{\text{Hall}} + \underbrace{\dots}_{\text{dissipative term to permit the reconnection}}$$

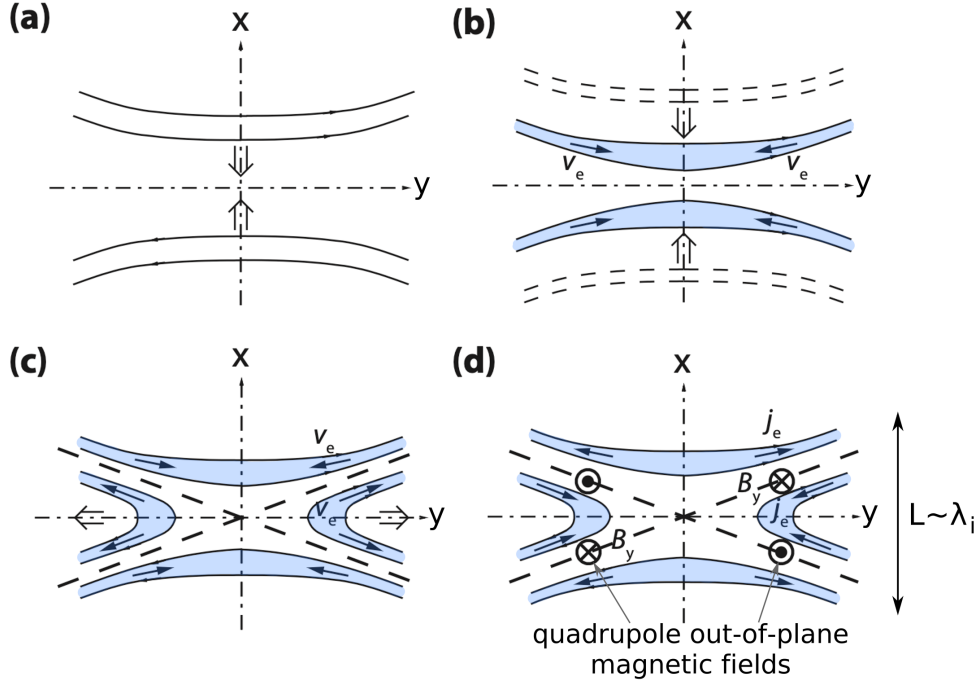


Figure 2.6: Generation of the quadrupole magnetic field by the Hall term. Adapted from [Uzdensky and Kulsrud, 2006]

perpendicular size of the reconnection region (making it larger than the Sweet-Parker size), which allows for continuity equation to transfer more plasma.

The Hall effect has been demonstrated by numerous two-fluid and kinetic simulations [Ma and Bhattacharjee, 1996, Biskamp et al., 1997, Ma and Bhattacharjee, 2001, Birn et al., 2001] and has been confirmed by the experimental observation in the laboratory plasmas [Ren et al., 2005, Yamada et al., 2006], in subsolar magnetopause [Mozer et al., 2002], in solar wind [Mistry et al., 2016] in the Earth's magnetotail [Tang et al., 2021].

- Electron inertia term (acts on the electron skin depth  $\lambda_e = c/\omega_{pe}$  scale): The concept of 'inertial' resistivity, in which the finite time a particle spends within the current layer plays the role of an intercollision time, was recognized by [Speiser, 1970, Wesson, 1990, Drake and Kleva, 1991, Ottaviani and Porcelli, 1993]. The inertial limit can be thought of as the resistive limit but with the resistivity determined by the flow time rather than by the (much longer) intercollision time. An effective inertial resistivity may be defined when the characteristic system length is small compared to a collisional mean free path. The lifetime of the particle in the system replaces

a mean time for collisions in the expression of the resistivity, which is essentially determined by the inertia of the particles within the size of electron skin depth  $\lambda_e$  (figure 2.7a). Thus, reconnection can proceed without collisions, with energy being carried off by accelerated particles [Speiser, 1970].

### The electron inertia term

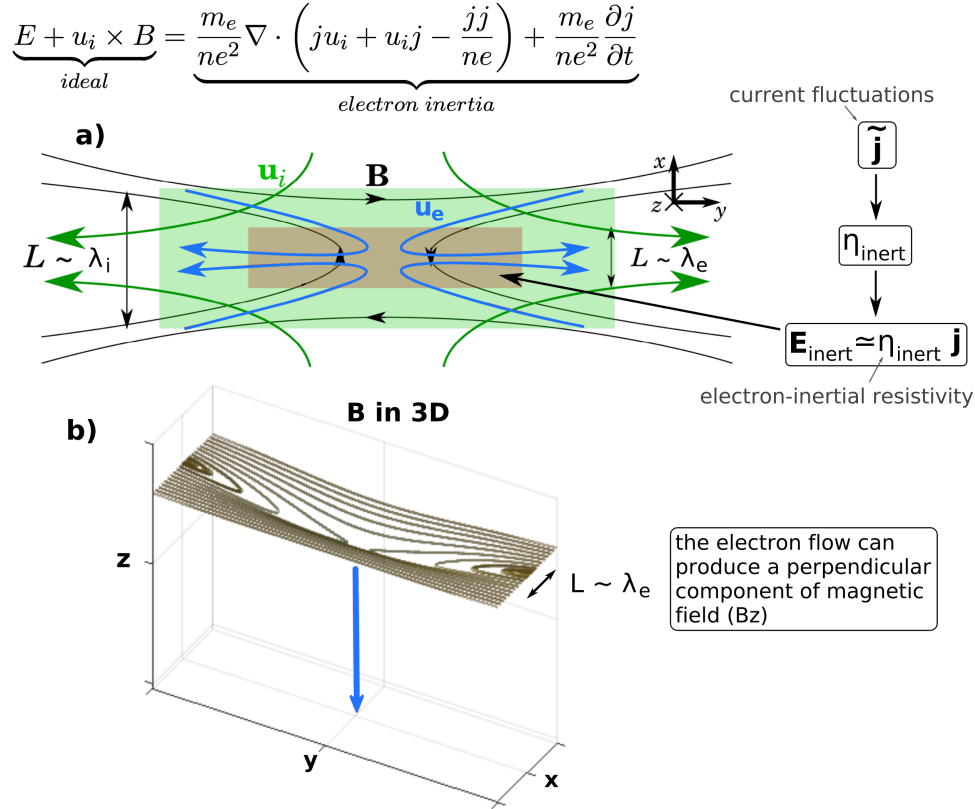


Figure 2.7: The effects produced by electron inertia term in generalized Ohm's law: a) electron-inertial resistivity  $\eta_{inert}$ , b) out-of-plane magnetic field  $B_z$  due to the electron outflow downstream from the X-point. Adapted from [Yoon and Bellan, 2018, Yoon, 2020]

The inertial resistivity is caused by fluctuation in the current density and can be estimated as [Baumjohann and Treumann, 2012, pg 376]:  $\eta_{inert} \approx 1/\epsilon_0 \omega_{pe}^2 \tau_j$ , where  $\tau_j$  is the typical time of variation of the current. The higher frequency of the current fluctuations ( $\nu_j = 1/\tau_j$ ) corresponds to a larger contribution of the inertial term to the resulting reconnection electric field. Since this fluctuation frequency is not expected to be a constant, the electron inertia effect is a temporarily variable process and is even suggested to switch on and off during the reconnection [Baumjohann and Treumann, 2012, pg 376].

The reconnection rate due to the inertial term can be faster than the classical Sweet-Parker rate due to the higher reconnection electric field that the term is capable to

generate. The contribution of the inertial term to the reconnection rate has been experimentally validated in Earth’s magnetopause reconnection [Genestreti et al., 2018].

Apart from that, the electron acceleration and outflow in the  $z$  direction can distort the magnetic field in the out-of-plane direction producing a perpendicular component of the magnetic field (figure 2.7b). This distortion occurs within the electron skin depth  $\lambda_e$  scale, where electrons are decoupled both from the ions and the magnetic field [Yoon and Bellan, 2018, Yoon, 2020]. This three-dimensional effect is suggested [Yoon, 2020] to explain the observations of the highly elongated stable structure downstream from the X-point of a magnetospheric reconnection [Phan et al., 2007] (electron diffusion region has a highly elongated stable structure, the electron jet extends at least 60 ion skin depths downstream from the X-point).

- Electron pressure gradient term (acts on the ion skin depth  $\lambda_i = c/\omega_{pi}$  scale ): the contributions from viscosity and anisotropy can be studied separately [Yoon and Bellan, 2019, Yoon, 2020] as shown in figure 2.8. Generally, higher viscosity leads to larger size of the current density region (figure 2.8a). And the pressure anisotropy skews the structure of magnetic lines that surround the reconnection X-point (figure 2.8b).

The nature of the electron pressure gradient is not fully understood. Some explanations of why viscosity and anisotropy of the electron fluid may appear in the reconnection region are suggested in [Baumjohann and Treumann, 2012, pg 374].

The pressure gradient effect has been numerically shown to increase the reconnection rate in semi-collisional and collisional plasmas in comparison to the Sweet-Parker rate [Dungey, 1989, Lyons and Pridmore-Brown, 1990, Aydemir, 1992, Kleva et al., 1995]. This increase is attributed to larger electric field generation in the X-point region and larger perpendicular size of the reconnection region (figure 2.8a) in comparison to the Sweet-Parker model. The influence of the pressure gradient term on reconnection has been experimentally validated in the reconnection of solar wind plasma in the Earth magnetosphere [Genestreti et al., 2018]. Moreover, these observations indicate that the reconnection rate was mostly defined by the electron pressure gradient term alone.

It should be noted that there is no consensus on which of these two-fluid terms play the major role in speeding up the reconnection rate (in comparison to the Sweet-Parker) since each of these terms is capable to increase the reconnection rate in collisionless plasmas acting alone (sole Hall effect: [Birn et al., 2001], sole electron inertia effect: [Andrés et al., 2014], sole electron pressure gradient effect: [Dungey, 1989, Lyons and Pridmore-Brown, 1990]). Furthermore, a different combination of these two-fluid terms may produce different resulting reconnection processes, since the reconnection is a highly nonlinear phenomenon.

## The electron pressure gradient term

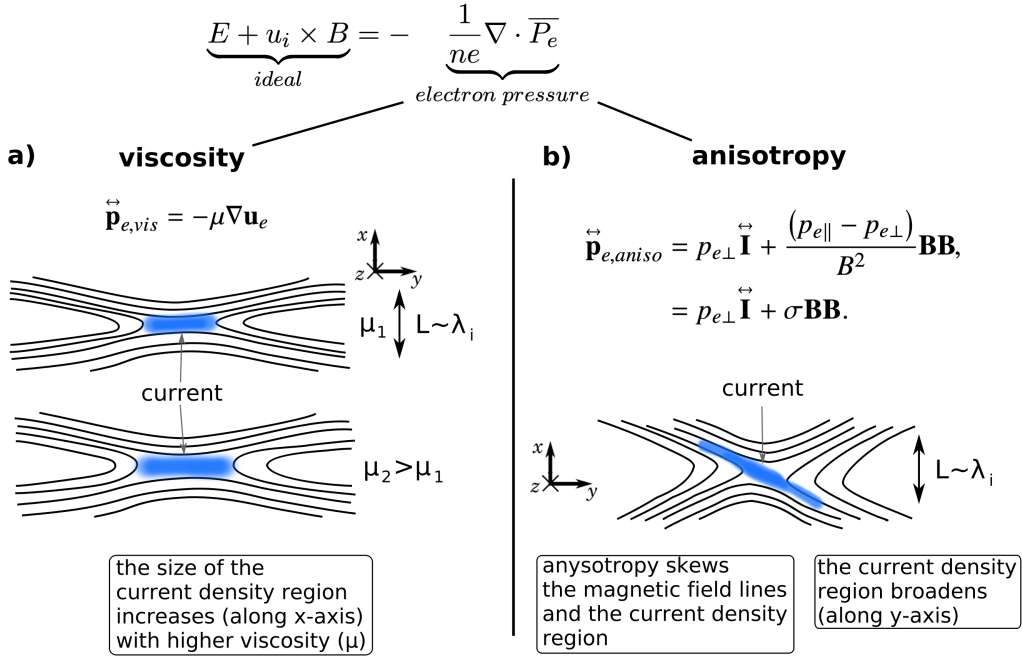


Figure 2.8: Effects on reconnection from a) viscosity and b) anisotropy in the electron pressure gradient term. The illustrations follow the description from [Yoon and Bellan, 2019].

## — Plasmoids and turbulence —

Two major assumptions invoked in the derivation of the SP model that are: (i) the reconnection geometry proposed by Sweet-Parker is steady-state, and (ii) the background plasma flow is laminar. In the following, we discuss the applicability of these assumptions.

First, [Loureiro et al., 2007] analytically found out that the Sweet-Parker diffusion layers are linearly unstable and break up into secondary islands or plasmoids [Samtaney et al., 2009] (figure 2.9), when  $S$  exceeds a critical value ( $S_c \sim 10^4$ ). The instability growth rate in the linear stage  $\gamma \sim S^{\frac{1}{4}}/\tau_A$  [Loureiro et al., 2007, Samtaney et al., 2009]. The number of plasmoids scales as  $S^{\frac{3}{8}}$  [Samtaney et al., 2009]. In the nonlinear regime, plasmoids continue to grow faster than they are ejected and completely disrupt the reconnection layer [Samtaney et al., 2009, Uzdensky et al., 2010], yet the reconnection rate seems to saturate (or show weak dependence on  $S$ ) at high- $S$  numbers [Huang and Bhattacharjee, 2010]. It is worth noting, that the plasmoid occurrence is possible even with the resistive single-fluid MHD description without the two-fluid effects described earlier. However, in semi-collisional and collisionless plasmas, these multiple plasmoids may break into even thinner current sheets through multiple levels of cascading (i.e. a chain of secondary magnetic islands, shown in figure 2.9) [Shibata and Tanuma, 2001, Loureiro and Uzdensky, 2015]. Due to the cascading, the current layers become even thinner and for them, the

two-fluid effects have to be taken into account [Loureiro and Uzdensky, 2015].

The plasmoids have been obtained numerically in the single-fluid and two-fluid MHD, and in the fully kinetic (PIC) plasma descriptions, (the up-to-date list of references can be found in [Ji et al., 2022, Yamada, 2022]) and observed in the laboratory experiments [Stenzel et al., 1986, Ono et al., 2011, Dorfman et al., 2013, Olson et al., 2016, Hare et al., 2017] and in the Earth’s magnetotail reconnection [Chen and Hau, 2022]. However, only single plasmoids at a given time have been observed in all of these experiments with the sole exception of [Jara-Almonte et al., 2016], where multiple plasmoids are reliably detected. In tokamaks, there is indirect evidence of multiple plasmoids [Liang et al., 2007, Ebrahimi and Raman, 2015] that is yet to be confirmed.

The discovery of plasmoids means that the Sweet-Parker assumption of the steady-state geometry does not hold when the Lundquist number exceeds the critical value  $S_c \sim 10^4$ .

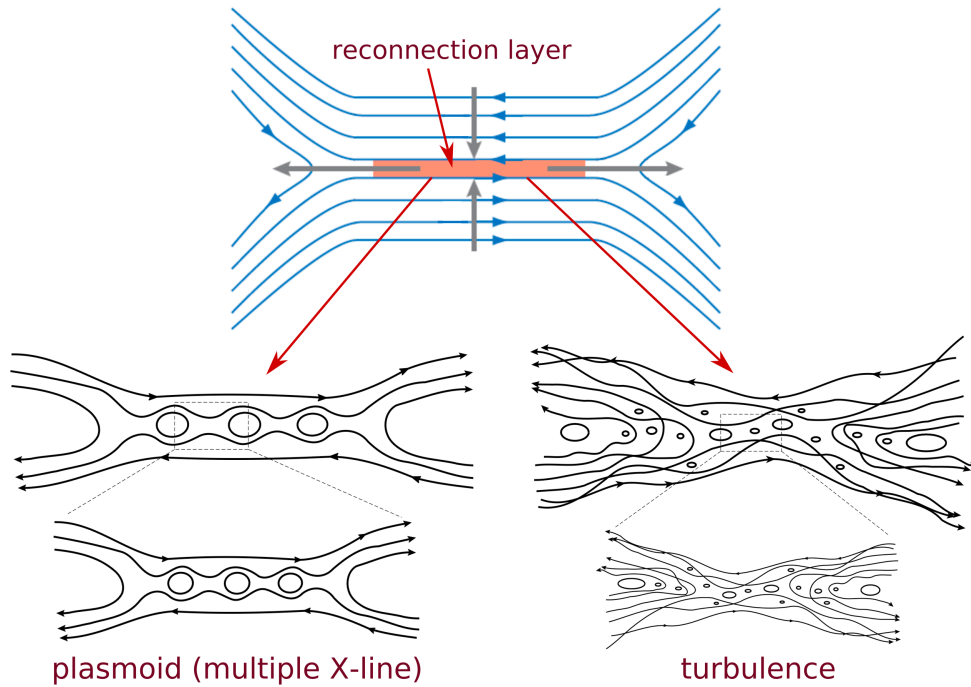


Figure 2.9: Artistic representation of plasmoids and turbulence formation in the reconnection region of the Sweet-Parker geometry. Adapted from [Ji et al., 2022]

Second, plasmas may have a certain level of magnetic turbulence [Tsytovich, 2016]. For example, in the interstellar medium, a so-called "big power law in the sky" indicates the presence of turbulence on scales from tens of parsecs to thousands of kilometres [Armstrong et al., 1994]. Furthermore, there is an experimentally observed evidence [Nakamura et al., 2017, Fu et al., 2017] for turbulent boundary layers in the reconnections that happen in Earth’s magnetosphere [Nakamura et al., 2017]. Generally speaking, eddies of plasma turbulence are thought to be anisotropic in all directions with respect to the local mean magnetic field [Loureiro and Boldyrev, 2020]. In particular, they should resemble current sheets-localized regions of intense electric current in the field-perpendicular plane, whose

aspect ratio increases with perpendicular wavenumber [Loureiro and Boldyrev, 2020]. Current sheets are, indeed, almost ubiquitously observed in direct numerical simulations of three-dimensional MHD turbulence [Zhdankin et al., 2013]. These turbulent current sheets may lead to the local (on the scale of turbulent eddies) magnetic reconnection events in magnetized plasmas [Wan et al., 2015], which, in turn, results in the conversion and dissipation of magnetic energy. Turbulence eddies may modify the dynamics of the classical Sweet-Parker reconnection if they occur within the diffusion region of Sweet-Parker geometry.

The effect of the turbulence on the reconnection in the Sweet-Parker geometry (figure 2.9) has been studied by many researchers [Matthaeus and Lamkin, 1986, Lazarian and Vishniac, 1999, Smith et al., 2004, Lazarian, 2005, Kowal et al., 2009, Servidio et al., 2009, Karimabadi et al., 2013, Ji et al., 2022]. Two origins of the turbulence are usually considered. First, the turbulence may arise spontaneously from the free energy available within the large-scale magnetic shear, which is responsible for driving reconnection. This might be realised through plasmoid interaction. Namely, plasmoids in 2D geometry become flux ropes in 3D, which can interact in a complex way by undergoing kink and coalescence instabilities [Daughton et al., 2011]. The current sheets have a single resonance surface in 2D geometry but may have multiple resonant surfaces in 3D, which may lead to stochastic field lines through overlapping islands [Rechester and Rosenbluth, 1978, Daughton et al., 2011]. Alternatively, Alfvénic turbulence inherent within the global system might drive further turbulence within the diffusion region [Ji et al., 2022].

In the presence of magnetic turbulence, the rate of magnetic reconnection may increase dramatically beyond the Sweet-Parker scale independently of the Ohmic resistivity and the two-fluid effects [Lazarian and Vishniac, 1999, Kowal et al., 2009]. This depends on the initial level of field stochasticity, which arises naturally whenever turbulence is present. However, as reconnection proceeds, the local turbulent cascade may grow stronger and the initial level of stochasticity will matter less and less [Lazarian and Vishniac, 1999].

A full picture of the relationship between reconnection and turbulence is yet to emerge since (i) analytical treatment of turbulence is one of the world-known "big" mathematical problems (analytical solution of the Navier-Stokes fluid equation is one of the seven Millennium Prize problems), and (ii) numerical simulations of turbulence in plasma at large Lundquist numbers in the three-dimensional kinetic description have high computational costs [Ji et al., 2022] (most of the simulations so far have been limited to  $S < 10^9$  in 2D and  $S < 10^4$  in 3D).

There is evidence of secondary reconnection inside filamentary currents of magnetic flux ropes (a confirmation of three-dimensional turbulent reconnection) during reconnection in Earth's magnetopause [Wang et al., 2020]. However, other observations [Torbert et al., 2018] of reconnection in the Earth's magnetotail indicate that the dominant electron dynamics are mostly laminar, despite the presence of turbulence near the reconnection site.

Since there is still no consensus on how the turbulence influences the reconnection process, the validity boundaries for the laminar plasma assumption remain to be drawn.

In this thesis, the turbulence effects are neglected (under "the presumption of innocence").

— Other effects —

There is a number of other effects that might influence the reconnection process: the connection between global (the macroscopic ideal plasma region outside of the reconnection area) and local (the microscopic resistive-diffusion region) scales; the trigger of the reconnection onset; the effect of the three-dimensional and asymmetric geometries; particle acceleration and the energy redistribution (how the magnetic energy converts to the kinetic and thermal energy of the particles during the reconnection), waves generated during the reconnection process. These physical processes are less known than the ones presented before and are beyond the scope of this thesis. The up-to-date understanding of these effects is presented in [Khotyaintsev et al., 2019, Yamada, 2022, Ji et al., 2022].

### 2.2.7 Strong guide field reconnection

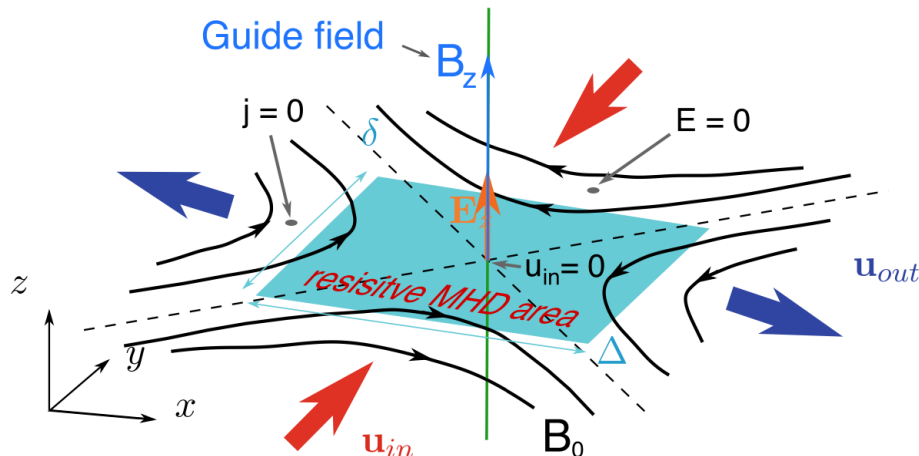


Figure 2.10: Sweet-Parker problem with a guide field  $B_z$ . The diffusion region is represented with the light blue rectangle. The area that surrounds this diffusion region is described by the ideal MHD. Reconnection electric field  $E$ , magnetic field  $B_0$ , and in/outflow velocities  $u_{in/out}$ , are shown in orange, black, and red/blue respectively. The figure is adapted from [Cozzani, 2020].

The Sweet-Parker geometry considers the two anti-parallel magnetic fields in a two-dimensional plane. However, in many cases of interest (such as reconnection in fusion and magnetospheric [Eriksson et al., 2016] plasmas), there is also an essentially uniform magnetic field directed perpendicular to the merging field lines. This latter field is usually termed the "guide field". Figure 2.10 shows the geometry of the guide field Sweet-Parker reconnection, where  $B_0$  is denoted as the reconnection field and  $B_z$  as the guide field. One distinguishes weak  $B_0 \gg B_z$ , moderate  $B_0 \approx B_z$  and strong  $B_0 \ll B_z$  guide field reconnections. In this thesis, we are focused on **the strong guide field reconnection**

in semi-collisional and collisionless plasma regimes (application to nuclear fusion research). This reconnection regime has the following important features:

- The electron pressure term becomes important on the ion sound Larmor radius  $\rho_s = \sqrt{\frac{k_B T_e}{m_i} \frac{1}{\omega_{ci}}}$  (where  $T_e$  is the electron temperature,  $m_i$  is the ion mass,  $\omega_{ci}$  is the ion Larmor frequency) scale-length (the ion skin depth  $\delta_i = c/\omega_{pi}$  is used for the classical Sweet-Parker). The scale length  $\rho_s$  enters the equations because of the requirement that the charge of the ions neutralizes the electron parallel flows. This can only occur for scale lengths smaller than  $\rho_s$  so that the ions are intrinsically coupled with the parallel electron dynamics [Kleva et al., 1995]. Generally, the reconnection rate increases with higher  $\rho_s$  values [Schmidt et al., 2009, Yu et al., 2012b, Granier et al., 2022], which is known as finite ion sound Larmor radius (FLR) effect.
- The Hall term in the generalized Ohm's law can be neglected since the quadrupole field associated with Hall reconnection disappears with a strong guide field [Rogers et al., 2003, Pritchett and Coroniti, 2004, Huba, 2005].
- The analytical theory and numerical simulations [Hesse et al., 2004, Ricci et al., 2004a, Pritchett and Coroniti, 2004, Horiuchi et al., 2014, Yu et al., 2014, Günter et al., 2015] indicate that the reconnection electric field  $E_z$  near the X-line is mainly determined by the electron pressure gradient and electron inertia terms in semi-collisional and collisionless regimes. This conclusion is supported by the recent experimental observations of the reconnection of solar wind plasma in the Earth magnetosphere [Eriksson et al., 2016, Fox et al., 2017, Genestreti et al., 2018]. They found that the reconnection electric field: is (a) well described by the sum of the electron inertial and pressure gradient terms in generalized Ohm's law; and (b) the pressure gradient term dominates the inertial term by roughly a factor of 5:1. Furthermore, the reconnection during sawtooth crashes (an example of a strong guide field reconnection in the semi-collisional plasma regime) has been simulated by a nonlinear two-fluid code [Yu et al., 2015] with the inclusion of the electron inertia and pressure gradients [Yu et al., 2014, Günter et al., 2015] (see also Chapter 5). These simulations show good agreement with the experimentally obtained reconnection rates during the crashes. This confirms the importance of the electron pressure gradient and inertia terms for the correct description of the reconnection.
- The plasmoids are observed in the two-fluid simulations of sawtooth crashes [Yu et al., 2014, Günter et al., 2015]. In these simulations, plasmoids have hardly any effect on the sawtooth reconnection rate [Günter et al., 2015]. The plasmoids form as a transient phenomenon only, while two-fluid effects lead to fast sawtooth reconnection that is independent of the Lundquist number [Günter et al., 2015]. The weak dependence of the reconnection rate on the plasmoid formation might be explained by an effect from the strong guide field. The plasmoids in three dimensions are flux ropes, which can interact in a complex way by undergoing kink and coalescence instabilities [Daughton et al., 2011]. This interaction may lead to the field line

stochastisation [Rechester and Rosenbluth, 1978, Daughton et al., 2011]. However, the strong guide field supports the structure of the flux ropes against the current and pressure gradient-driven instabilities (as screw-pinch becomes stable in comparison to z-pinch [Zohm, 2015, pg 18]). This stabilising effect might be the cause of the weak influence of the plasmoids on the reconnection rate in sawtooth crashes.

- The reconnection rate in the strong guide field is generally slower (up to a factor of three) than the classical reconnection without guide-field [Karimabadi et al., 1999, Hesse et al., 2002, Pritchett and Coroniti, 2004, Huba, 2005, Yamada et al., 2010]. The observed slower rates are attributed to [Yamada et al., 2010]: (i) smaller resistivity for a neutral-sheet current parallel to the guide field, (ii) suppression of plasma flow by the guide field, and (iii) less compressibility of the plasma due to presence of a guide field.

Finally, having introduced the importance of the two-fluid effects and particularities of the strong guide field reconnection, we have prepared ourselves to discuss the main research subject of this thesis.

## 2.3 Sawtooth instability

This section deals with magnetic reconnection events observed in all tokamaks - the sawtooth instability. The description and an explanation of this instability are presented.

### 2.3.1 Notations in toroidal coordinates

First of all, the notations, which are commonly used among tokamak community, are introduced. There are three coordinate systems (figure 2.11): toroidal  $(r, \theta, \phi)$ , cylindrical  $(R, z, \phi)$  or straight field line coordinates  $(\rho, \theta^*, \phi)$ , where  $R$  is the major radius,  $r$  is the minor radius,  $\theta$  is the poloidal angle,  $\phi$  is the toroidal angle and  $z$  is the height above the midplane,  $\rho$  is the radial coordinates, and  $\theta^*$  is the poloidal straight field line angle. The radial coordinate  $\rho$  can be expressed in terms of the poloidal fluxes,  $\Psi$ ,

$$\rho_{pol} = \sqrt{\frac{\Psi - \Psi_0}{\Psi_a - \Psi_0}} \quad (2.34)$$

, where  $\Psi_0$  and  $\Psi_a$  are the poloidal flux on axis and on the last closed plasma surface, respectively. Alternatively,  $\rho$  can be expressed in terms of the toroidal fluxes,  $\Phi$ ,

$$\rho_{tor} = \sqrt{\frac{\Phi - \Phi_0}{\Phi_a - \Phi_0}} \quad (2.35)$$

, where  $\Phi_0$  and  $\Phi_a$  are the toroidal flux on axis and on the last closed plasma surface, respectively.

Figure 2.11b shows poloidal magnetic field  $B_p$  generated by a plasma current  $I$  of a tokamak. The combination of the toroidal  $B_t$  (directed along the minor axis) and poloidal

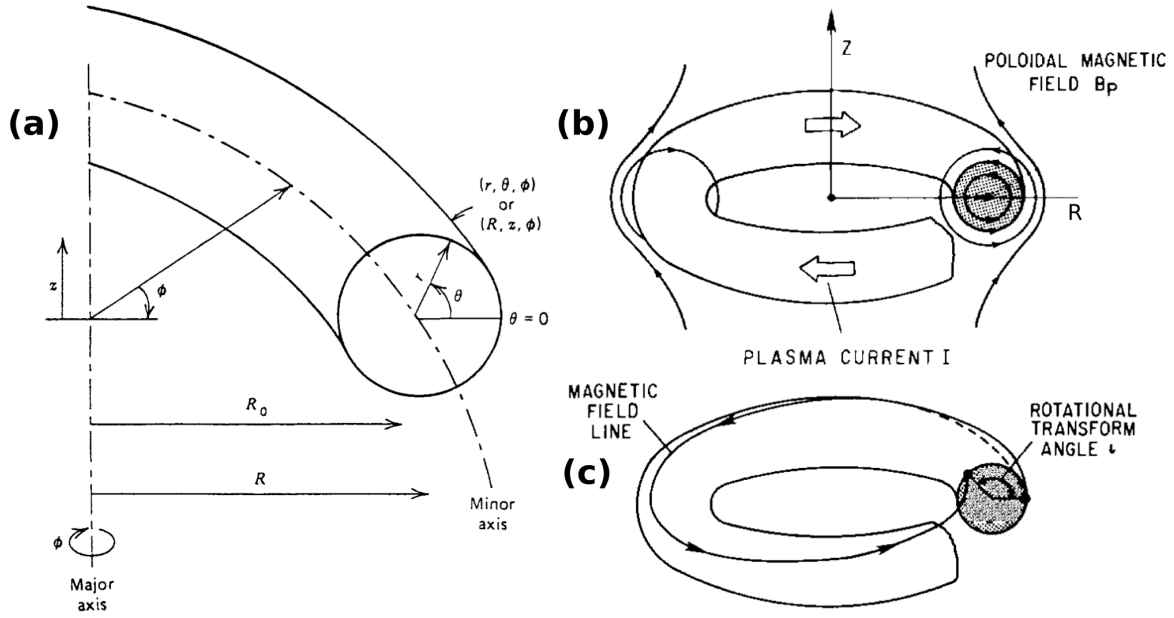


Figure 2.11: Tokamak configuration: (a) shows the notation of the toroidal  $(r, \theta, \phi)$  and cylindrical  $(R, z, \phi)$  coordinate systems; (b) shows the total poloidal field  $B_p$ , which is a combination of the field produced by a plasma current  $I$  and an externally imposed "vertical" field; and (c) shows how the combined effect of toroidal and poloidal magnetic field produces a rotational transform  $\iota$ . The figures are adopted from [Teller, 2012, pg 36] and [Stacey, 2012, pg 57].

magnetic fields gives the helical magnetic field (figure 2.11c). The pitch (also called twist or helicity) of a helical field line can be expressed with the rotational transform  $\iota$ , which is the number of times a field line goes around a torus the short way for each time it goes around the long way:

$$\iota = 2\pi \frac{R \cdot B_p}{r \cdot B_t} \quad (2.36)$$

A tokamak equilibrium consists of nested magnetic surfaces of constant plasma pressure. The rotational transform varies along the minor radius, producing a magnetic shear between the magnetic surfaces (figure 1.2c). The reason of this variation is that the toroidal and poloidal magnetic fields as well as the plasma current are not constant along the minor radius (due to the toroidal geometry:  $B_t(R) \sim B_0 R_0 / R$ , due to the plasma resistivity dependence on the plasma temperature ( $\sigma \sim T^{-3/2}$ ), the plasma current is peaked on the magnetic axis and can be approximated as  $I(r) = \int_0^r j_0 \left(1 - \left(\frac{r}{a}\right)^2\right)^\mu dr$ , which corresponds to the poloidal field  $B_p(r) \sim \frac{\mu_0 I(r)}{2\pi r}$  [Zohm, 2015, pg 19]).

A particular situation occurs when a magnetic surface has the rotational transform  $\iota$  equals to a rational number (like 1, 1/2, 3, 2/3, 3/4, and so forth), which means that the helical field lines close on themselves after a number of turns (for example, in figure 2.12a: the red field line closes on itself after two toroidal turns). These magnetic

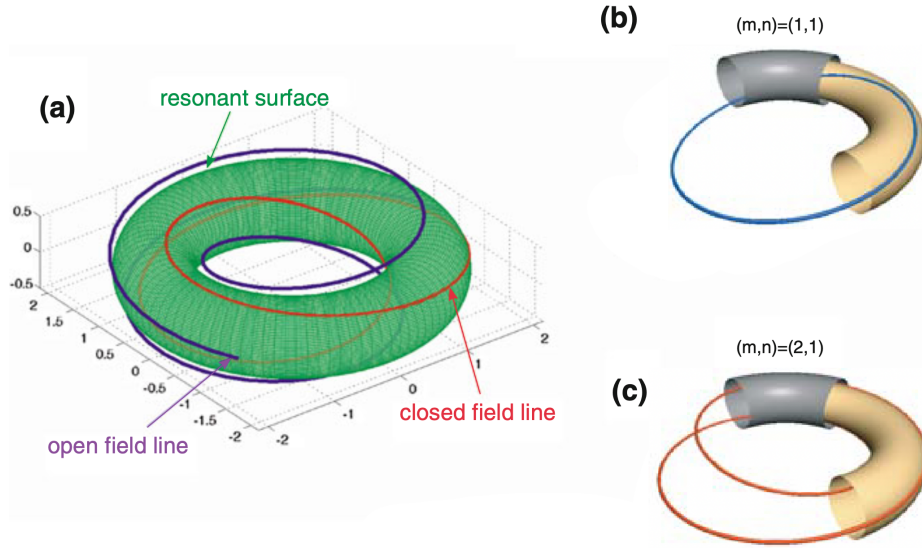


Figure 2.12: (a) Resonant surface (green) and corresponding closed field line (red). The neighboring flux surface is non-resonant and the field line is open (blue). (b) and (c) show a closed field line of (1,1) and (2,1) modes, respectively. The figure is adapted from [Igochine et al., 2015, pg 28].

surfaces are susceptible to a variety of MHD instabilities [Zohm, 2015, Igochine et al., 2015] ranging from barely noticeable types (e.g. classical compressional Alfvén waves) to the ones that are impossible to overlook (e.g. locked tearing mode, which may lead to a plasma disruption and destruction of a wall component of a tokamak).

A seemingly mystical connection between the rational numbers and the MHD instabilities can be qualitatively understood through the two following concepts. First, rational surfaces allow to have different current densities at different places on the same magnetic surface. Furthermore, a  $(m, n)$  rational surface is susceptible to current perturbations that act as a seed perturbation to a  $(m, n)$  tearing mode growth (maximum and minimum of a current perturbation are located on O and X point of a tearing mode, respectively). Second, the magnetic field lines produce tension forces that act against plasma displacements (i.e. when plasma tries to change its form). One can imagine the magnetic field lines as rubber bands surrounding the toroidal surfaces of plasma. A rubber band is harder to deform when it has a longer length (the band circulates around the toroidal surfaces more times). A band has a longer length when the  $m$  poloidal and  $n$  toroidal are high or their ratio is an irrational number. As a result, (i) higher  $(m, n)$  modes have slower growth rates than modes with lower  $(m, n)$ , and (ii) MHD modes are not observed on the non-resonant magnetic surfaces.

The excitation of the MHD instabilities on magnetic surfaces is tightly connected with the operational limits of a tokamak. For tokamak, a quantity that represents the stability of a certain rational surface is called safety factor  $q$  (in the approximation of a straight

cylindrical tokamak):

$$q = \frac{2\pi}{\iota} = \frac{r \cdot B_t}{R \cdot B_p} = \frac{\Delta\phi}{\Delta\theta} = \frac{m \text{ (number of poloidal turns)}}{n \text{ (number of toroidal turns)}} \quad (2.37)$$

Large  $q$  means the twist is gentle (the magnetic surface has better stability), and small  $q$  means that the twist is tight (the magnetic surface has worse stability).

Since most of MHD instabilities are located on the magnetic surfaces with rational number  $q$  (also called resonant surfaces), it is common to name an instability with its poloidal mode number  $m$  and toroidal mode number  $n$ , in short -  $(m, n)$  mode. The resonant surface of an  $(m, n)$  mode is usually notated as  $\rho_{m,n}$  or  $\rho_{q=m/n}$ . Radial displacement due to an instability has displacement amplitude  $\hat{\xi}_r(\rho)$  and can be written as:

$$\xi_r(\rho) = \hat{\xi}_r(\rho) \cdot \cos(m\theta^* - n\phi + \omega t) \quad (2.38)$$

, where  $\omega$  is a real number representing the angular frequency of the mode rotating in the laboratory frame.

### 2.3.2 Phenomenology

The sawtooth oscillations cycle is described as follows. The plasma is heated ohmically (i.e., by collisions that resist the plasma current). Since the current density is peaked on-axis, the core of the plasma is preferentially heated, causing the temperature to peak in the core. Since the resistivity decreases with increasing temperature ( $\eta \propto T^{-3/2}$  for collisional plasma), the core becomes a relatively better electrical conductor than the edge, and the current density further peaks at  $r = 0$ , causing  $q(0)$  to decrease. This leads to a further increase in the local heating rate, a further peaking of the temperature, and a further decrease in  $q(0)$ . When  $q(0)$  drops below unity, a  $q = 1$  magnetic surface forms in the plasma core. On the  $q = 1$  flux surface, the internal kink instability with poloidal mode number  $m = 1$  and toroidal mode number  $n = 1$  (or  $(1, 1)$  mode) is triggered. The  $(1, 1)$  kink mode is often called a precursor mode. Its nonlinear evolution leads to a crash - a rearrangement of the magnetic flux (magnetic reconnection) and flattening of the plasma temperature. The temperature inside the  $q = 1$  surface exhibits a rapid decrease, while outside that surface it exhibits a rapid increase until the original state with relatively flat temperature and  $q(0) > 1$  is restored. The cycle then repeats itself (figure 2.13).

For our study, an important subject is physics during the precursor and crash phases, which will be discussed in the following subsections.

### 2.3.3 Kink mode

Kink instability is a plasma instability that produces helical kinking of a current channel and is driven by excessively large electric currents for a given magnetic flux in the same direction (figure 2.14a). In a tokamak, our focus is the  $(m,n) = (1,1)$  kink mode, which has helical structure of the plasma displacement (figure 2.14b and 2.14c).

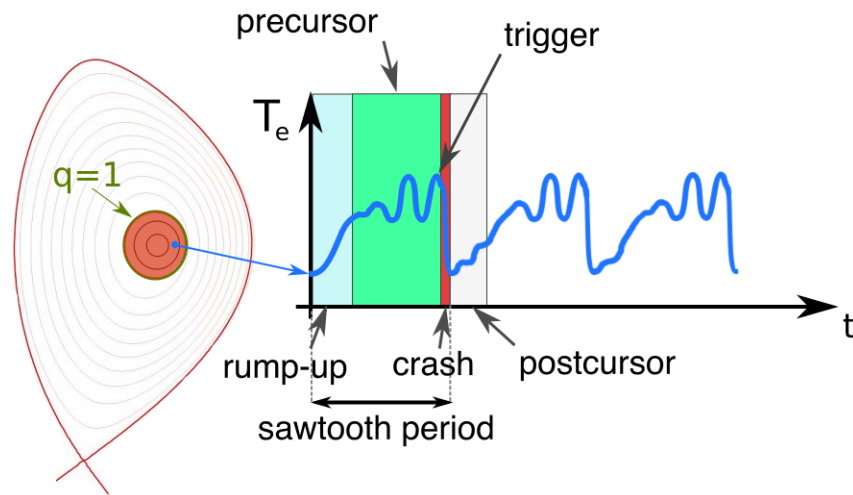


Figure 2.13: An illustration of different stages (rump-up, precursor, trigger and postcursor) of the sawtooth crash.  $T_e$  is the electron temperature,  $t$  is the time.

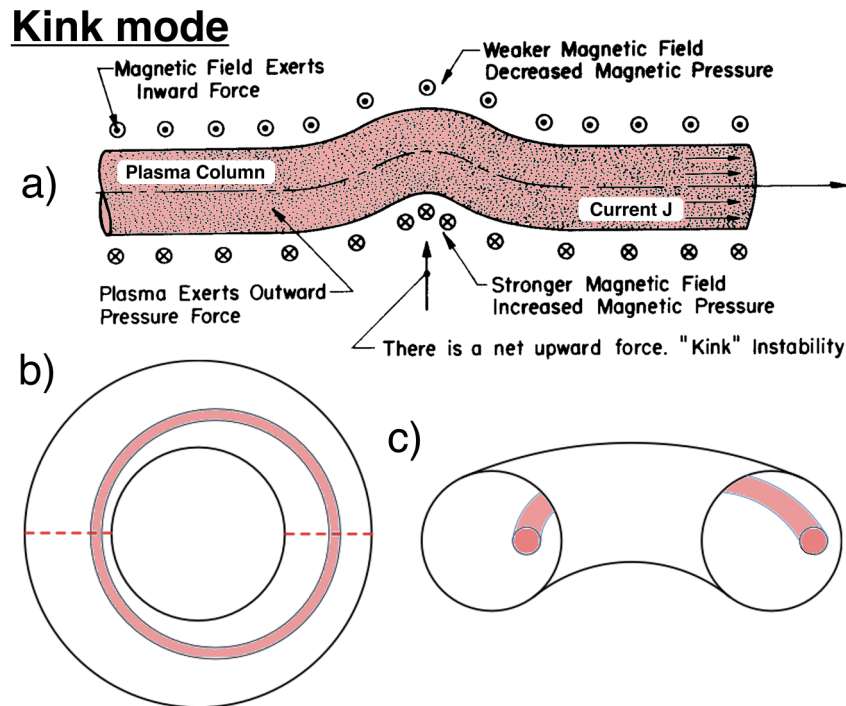


Figure 2.14: An illustration of a kink mode in a plasma column (a), and  $(m,n)=(1,1)$  kink mode in a torus top view (b) and in its poloidal cross-section (c). The figures are adapted from [Krall and Trivelpiece, 1973, pg 15][Chen, 2011, pg 221].

A comprehensive review of the  $(1,1)$  kink stability can be found in [Schnack, 2012], which is an elegant and humorous report written in a language of "mere mortals" (only

simple mathematics for physicists used). This report is both entertaining (and might be even educating) and sad, since this was the last report ever published by Dalton Schnack. In this thesis, we skip the mathematical derivations and discuss only the key physical understanding of (1,1) kink mode stability.

Important analytical results of the (1,1) mode stability with a circular plasma cross-section and a parabolic plasma current profile:

- **Cylindrical geometry, linear and nonlinear, ideal and resistive MHD:** the ideal (1,1) is unstable when  $q(0) < 1$  [Rosenbluth et al., 1973a]. However, the proposed solution disagrees with experimental observations [Schnack, 2012]: the analytical growth rate is too fast, the analytical displacement (nonlinear saturated amplitude of the kink) is too small, and a stable kink mode can be observed even when  $q(0) < 1$ . A solution of the resistive (1,1) mode [Coppi et al., 1976, Ara et al., 1978] can produce: (a) larger amplitudes of the plasma displacement, (b) slower growth rates (both the amplitude and the growth rate are now comparable to the experimental ones), and magnetic reconnection with a growth of (1,1) magnetic island ([Kadomtsev, 1975] speculated, but did not prove, that the reconnection may continue until the magnetic island at the rational surface expels the original magnetic axis producing  $q(0) = 1$  and stabilizing the plasma). Furthermore, the resistive kink can be unstable even when the ideal kink is stable [Ara et al., 1978].
- **Toroidal geometry, linear and nonlinear, ideal and resistive MHD:** toroidal geometry brings two effects [Schnack, 2012]. First, in a semi-collisional or collisionless plasma, some of the particles become trapped on the outboard side of the torus (moving in so-called banana orbits). This leads to non-Maxwellian velocity distributions and modifications of the moment equations that describe the fluid plasma. Second, the toroidal geometry induces a coupling between all the poloidal m-numbers for a given toroidal n-number. An important for us is the coupling between the (1,1) and (2,1) modes. The latter is ideally stable for  $q(a) > 2$  and produces a stabilising effect on the ideal (1,1) mode. Due to this coupling, the ideal (1,1) mode in a torus is linearly stable in the limit  $\beta_p \rightarrow 0$  ( $\beta_p = \frac{\langle p \rangle}{B_p^2/2\mu_0}$ , where p is the plasma pressure,  $B_p$  is the poloidal magnetic field). Instability requires  $\beta_p > 0.3$  [Bussac et al., 1975, Ara et al., 1978, Bussac and Pellat, 1987, Hastie et al., 1987, De Blank, 2008]. However, this result was achieved with a parabolic plasma current profile (strong magnetic shear). For a weak magnetic shear, an ideal (1,1) can be still unstable in a torus with  $\beta_p \rightarrow 0$ . Furthermore, the nonlinear analysis shows the opposite results to the linear one: the pressure gradient (also called the finite ion Larmor-radius (FLR) effect) is lead to the stabilization (reduction of the growth rate) of the (1,1) mode [Ara et al., 1978].

These analytical results bring a qualitative understanding of the (1,1) mode stability. However, this approach is limited to (a) circular cross-section and parabolic current profile, while both the shaping (which is elongation and triangularity) and the current profile are known to affect the mode stability [Lutjens et al., 1992, Martynov et al., 2005]; and (b)

the pure MHD framework, while kinetic effects such as plasma rotation (even though a given plasma flow profile is possible to include in the MHD framework, the evolution of this profile requires kinetic description) and the distribution of fast non-Maxwellian particles can play the major role in determining the stability.

Numerical resistive nonlinear MHD (via small perturbation stability analysis) in a toroidal geometry gracefully analyzes the  $(1,1)$  mode stability for a given equilibrium in any plasma shape. This analysis gives reliable and robust results for the mode growth rate and its amplitude, but only when there are no energetic (non-Maxwellian) particles and no externally induced plasma rotation (no NBI beams) [Chapman, 2010]. To include the latter two effects, one has to couple the MHD and kinetic frameworks. However, this is not an easy task, since the nonlinear kinetic description in the toroidal geometry is mathematically complex and numerically demanding. Luckily, [Porcelli et al., 1996] proposed a much simpler solution (known as the Porcelli model) within the linear  $0D$  MHD framework based on the energy principle. This model includes all the major MHD and kinetic effects and can successfully describe the kink destabilization observed in the experiments [Schnack, 2012]. The limitations of the Porcelli model: (a) it uses tokamak-specific fitting parameters (its prediction for future tokamaks might be not reliable); (b) it can not describe the nonlinear evolution of the mode and the crash event.

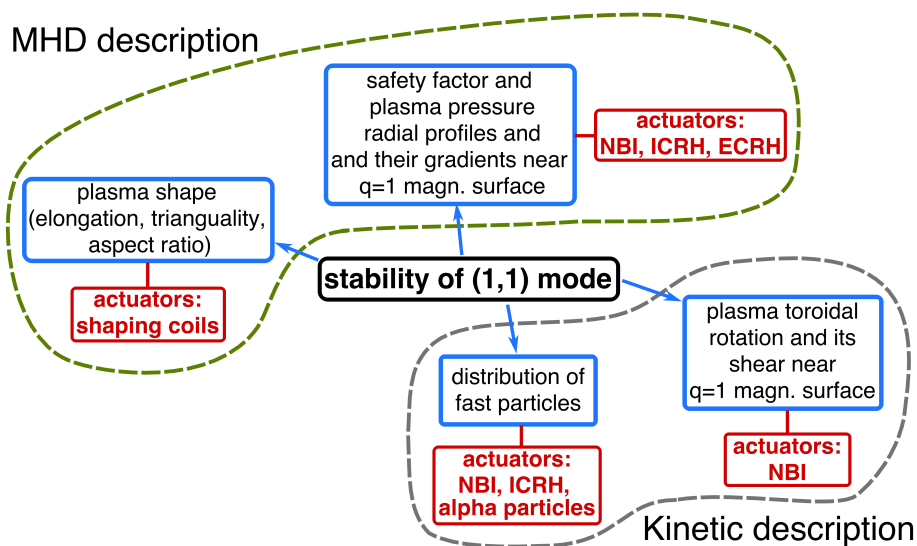


Figure 2.15: Actuators of  $(1,1)$  mode stability grouped into MHD and Kinetic plasma framework. NBI stands for neutral beam injection; ECRH and ICRH stand for electron and ion cyclotron resonance heating, respectively.

To summarize, we present a diagram (figure 2.15) of the  $(1,1)$  mode stability actuators that are available in a tokamak.

### 2.3.4 Trigger problem

Thanks to the Porcelli model, an onset of the  $(1, 1)$  kink mode can be successfully predicted. However, the model is not able to say, when the crash occurs. Even though the crash is commonly attributed to the nonlinear evolution of the kink mode, the exact criteria for the fast reconnection onset is not yet formulated. In the Porcelli model, the time duration between the precursor destabilization and the crash trigger (figure 2.13) is usually set by a fitting parameter based on the experimental data. This fitting is purely empirical and does not include physics. Thus, there is no guarantee that this fitting approach of the Porcelli model will work in future fusion reactors.

The trigger or onset problem can be generally formulated through the following questions [Cassak, 2006]. 1) What suppresses fast reconnection before onset? In other words, how is it possible that the system can be loaded with large amounts of magnetic energy over an extended period of time without significant release of the energy and without triggering the onset? (If the trigger is set off too easily, large amounts of free magnetic energy would not be able to accumulate and a large solar flare, for example, would never occur.) 2) What is the trigger mechanism which switches fast magnetic reconnection on, and what are the critical conditions under which such a transition occurs?

Currently, there is no commonly accepted theory that would answer these questions. Apart from the fusion plasmas, the trigger problem is relevant to magnetospheric substorms, to solar and stellar flares and coronal mass ejections, to various astrophysical events such as in gamma-ray flares in the Crab Nebula and magnetar magnetospheres [Yamada, 2022].

There often exist several promising and competing candidate scenarios to trigger reconnection, but, generally, they fall into one of two categories [Ji et al., 2022]: external drive or macroscopic instabilities, as described later. The former category refers to the case when, even under constant external drive, the onset moment of fast reconnection is determined by internal multiscale dynamics within the reconnecting current sheets (possible triggers are plasmoids and/or two-fluid effects). By contrast, in the latter category, the driving free energy is stored in places such as large-scale flux ropes, which can be destabilized to trigger reconnection. Furthermore, there can be potentially two-way feedback between the macroscale instability and the diffusion region microphysics at the reconnecting current sheets [Ji et al., 2022].

### 2.3.5 Kadomtsev model

Now, we have arrived to the crash phase of Sawtooth instability. The most well-known model of the crash is proposed by [Kadomtsev, 1975] (figure 2.18). Kadomtsev envisioned a sequence of events that begin with  $q(0) > 1$ . As the core of the plasma heats (Ohmically or otherwise) the current density becomes more peaked on the axis, driving  $q(0)$  to be less than unity. This occurs on a relatively slow time scale governed by the heating rate. Then the  $q = 1$  singular surface appears in the plasma, and the resistive internal kink is destabilized. As the nonlinear evolution expels the original magnetic axis, the  $q = 1$

singular surface disappears, and  $q(0)$  is restored to greater than unity. This process occurs on a faster time scale governed by the dynamics of the nonlinear resistive kink.

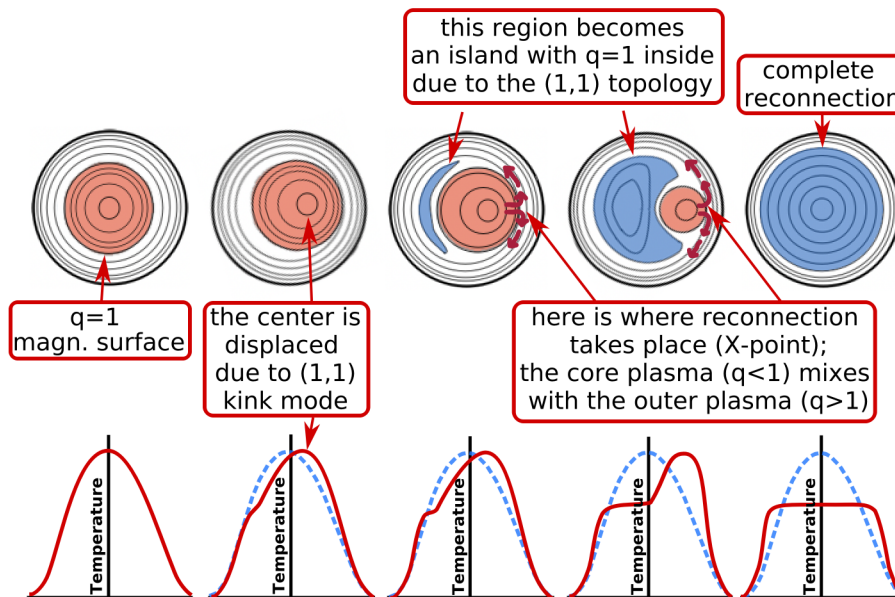


Figure 2.16: A sequence of events during the magnetic reconnection envisioned by Kadomtsev.

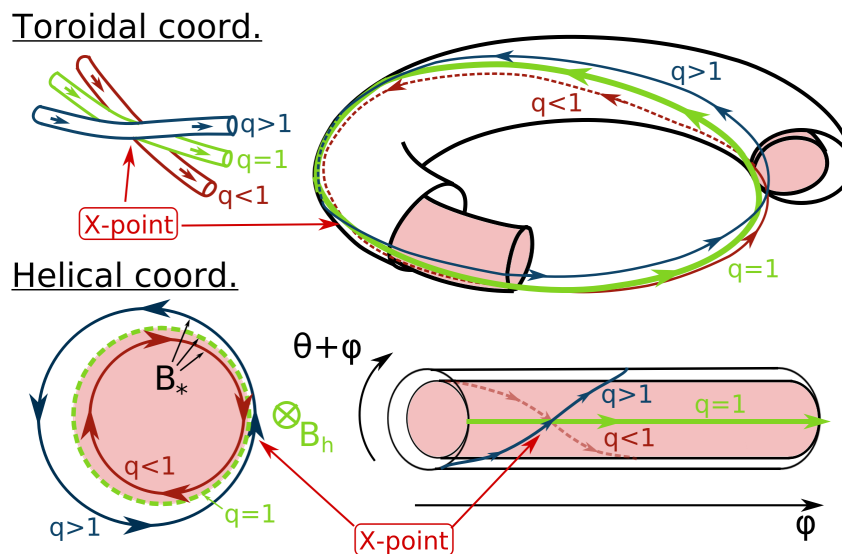


Figure 2.17: Artistic representation of the X-point geometry during magnetic reconnection in a sawtooth crash.

The Kadomtsev reconnection time follows the Sweet-Parker model of forced magnetic reconnection (single-fluid collisional MHD description of plasma) assuming cylindrical geometry and 2D helically symmetrical reconnection geometry (figure 2.18).

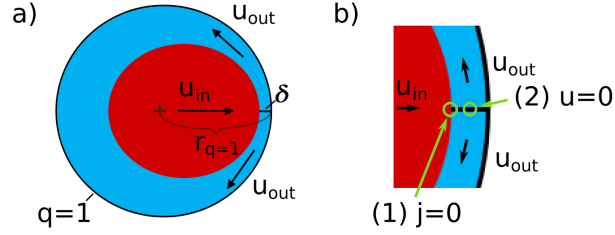


Figure 2.18: Kadomtsev magnetic reconnection process that follows the Sweet-Parker model of forced reconnection.

Safety factor (in a tokamak):

$$q = \frac{r}{R_0} \frac{B_\phi}{B_\theta} \quad (2.39)$$

at  $q = 1$ :

$$B_\theta = \frac{r_{q=1}}{R_0} B_\phi \quad (2.40)$$

only helical component of poloidal magnetic field is reconnected:

$$B_\theta^* \approx B_\theta(1 - q_0) \quad (2.41)$$

Ohm's law:

$$\mathbf{E} + \mathbf{u} \times \mathbf{B} = \eta \mathbf{j} \quad (2.42)$$

In the region (1) in figure 2.18b  $j = 0$ :

$$E = u_{in} B_{in} \quad (2.43)$$

In the region (2) in figure 2.18b  $u = 0$ :

$$E = \eta j \quad (2.44)$$

from 2.43 and 2.44, and substituting  $B_{in} = B_\theta^*$ :

$$j = \frac{u_{in} B_\theta^*}{\eta} \quad (2.45)$$

Ampere's law:

$$\mu_0 \mathbf{j} = \nabla \times \mathbf{B} \approx \frac{B_\theta^*}{\delta} \quad (2.46)$$

Combining equations 2.45 and 2.46:

$$u_{in} = \frac{\eta}{\mu_0 \delta} \quad (2.47)$$

from the energy conservation:

$$\frac{\rho u_{out}^2}{2} = \frac{B_\theta^{*2}}{2\mu_0} \quad (2.48)$$

we have:

$$u_{out} = \frac{B_{\theta}^{*2}}{\sqrt{\mu_0 \rho}} = u_A^* \quad (2.49)$$

where  $u_A^*$  is Alfvén velocity using helical magnetic field. Mass conservation:

$$u_{in} r_1 = u_{out} \delta \quad (2.50)$$

using equations 2.47 and 2.49:

$$\delta = \sqrt{\frac{\eta r_1}{\mu_0 u_A^*}} \quad (2.51)$$

Time to reconnect the distance  $r_1$ :

$$\tau_{r_1} = \tau_K = \frac{r_1}{u_{in}} = \frac{r_1 \mu_0 \delta}{\eta} \quad (2.52)$$

using equation 2.51, we obtain the Kadomtsev reconnection time:

$$\tau_K = \sqrt{\frac{\mu_0 r_1^2}{\eta} \frac{r_1}{u_A^*}} = \sqrt{\tau_R \tau_A^*} \quad (2.53)$$

Kadomtsev's model suggests that the helical flux can be calculated from the flux diagram shown in figure 2.19a. Before the crash the regions  $dr_-$  and  $dr_+$  are covered by equal flux elements  $d\Psi$ . These regions, which are located on the inner and the outer sides of the  $r_1$ , will connect and form a single flux element  $d\Psi$  covering the region  $rdr$  at the radius  $r$ . The reconnection starts at the  $q = 1$  surface, where the initial helical flux reaches its maximum,  $\Psi_{max}$ . The flux element at  $r_1$  will form the new center of the plasma and therefore the central value of the flux after the crash is equal to the maximum value of the flux before the crash.

The poloidal area covered by the poloidal flux element  $d\Psi$  is conserved throughout the crash, that is

$$rdr = r_- dr_- + r_+ dr_+ \quad (2.54)$$

$$\int_0^r r dr = \int_{r_-}^{r_1} r_- dr_- + \int_{r_1}^{r_+} r_+ dr_+ \quad (2.55)$$

$$r^2 = r_-^2(\psi) - r_+^2(\psi) \quad (2.56)$$

**Criticism of the Kadomtsev model:** wrong time scale,  $q(0) < 1$  is observed after the crash, postcursor observed (reconnection is incomplete).

### 2.3.6 Quasi-Interchange model (Jardin model)

The basic mechanism of the Jardin model [Jardin et al., 2020] is that for a sufficiently low central magnetic shear  $q \gtrsim 1$ , any pressure gradient will cause a (1,1) interchange instability to develop. This (1,1) interchange mode nonlinearly produces a central (0,0)

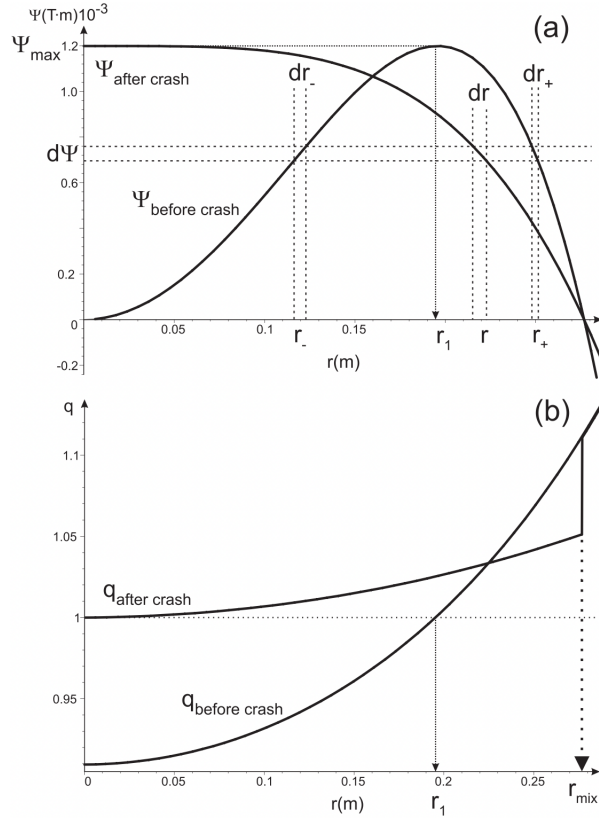


Figure 2.19: The safety factor,  $q(r)$ , and helical magnetic flux,  $\Psi(r)$  profiles before and after the sawtooth crash according to the Kadomtsev reconnection model. The picture is taken from [Merkulov, 2006].

dynamo loop voltage that acts to raise  $q(0)$ . The growth rate for this (1,1) mode has a maximum at  $q(0) = 1$  and decreases as  $q(0)$  increases further. This serves to regulate the process and keep  $q \gtrsim 1$ . If the pressure gradient exceeds a critical value, the resulting dynamo loop voltage will be strong enough to keep  $q \gtrsim 1$  and prevent the crash (also known as flux pumping effect [Krebs et al., 2017]). However, if sufficient central heating is applied to keep peaking the temperature and density profiles so that the pressure gradient exceeds the second critical value, then many high- $n$  modes with  $m = n$  abruptly become unstable, causing a stochastic region to form near the magnetic axis, locally flattening the pressure profiles in the center. This process does not involve magnetic reconnection as the  $q$ -profile remains slightly above unity and shear free, and the modes are non-resonant. In this picture, the role of the (1,1) mode is to regulate the  $q$  profile, and it is  $(m, n)$  with  $m = n > 1$ , which are responsible for the crash.

[Jardin et al., 2020] states that the proposed scenario of the crash is valid above a critical value of  $\beta$  and at sufficiently high  $S$ . At low- $\beta$  and low- $S$  discharges, the Kadomtsev model will apply.

**Criticism of the Jardin model:** The model does not produce local poloidal highly

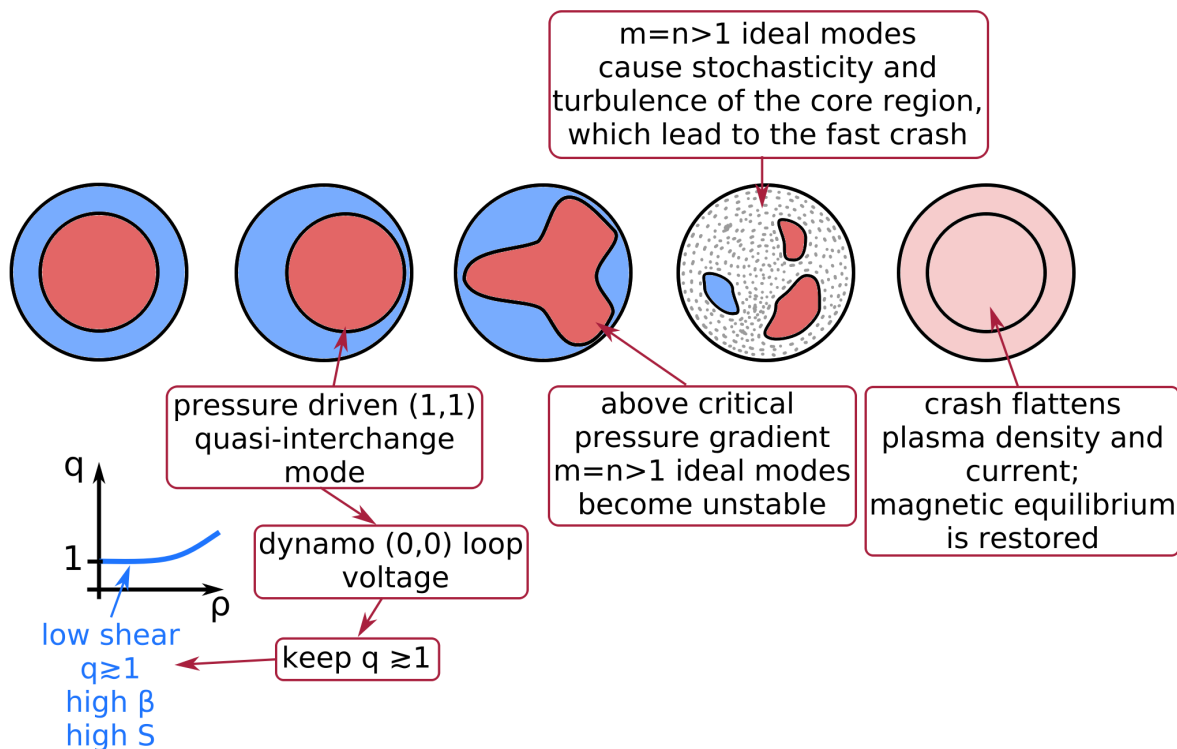


Figure 2.20: An artistic representation of the Jardin model that describes the sawtooth crash evolution.

collective heat outflow, which is observed by ECEI in several tokamaks (for example, the measurements in Chapter 5).

### 2.3.7 Stochastic model

Stochastic model of the sawtooth crash is put forward by authors [Lichtenberg et al., 1992, Nishimura et al., 1999, Igochine et al., 2006a, Igochine et al., 2008, Kolesnichenko and Yakovenko, 2013]. There are different scenarios how the stochastisation may develop. We describe a scenario proposed by [Igochine et al., 2006a, Igochine et al., 2008] as an example. First, the onset of an  $(1,1)$  ideal mode begins when  $q(0) < 1.0$ . The growth of the  $(1,1)$  mode leads to the nonlinear phase of the evolution and the harmonics of the primary mode ( $(2,2)$  and  $(3,3)$  modes) emerge in the system (other helicities may also be considered). At the same time, a bifurcation in the system excites the second mode with an irrational frequency ratio with respect to the primary  $(1,1)$  mode. The low-frequency spectrum becomes filled with a linear combination of these frequencies. The interaction between the modes increases, which causes frequency locking. Such locking induces reconnection. Immediately after the start of the reconnection stochastization develops. Stochastization of magnetic field lines appears only for a very short time period that is the crash phase itself. The island is not destroyed and the mode remains at the same position after the

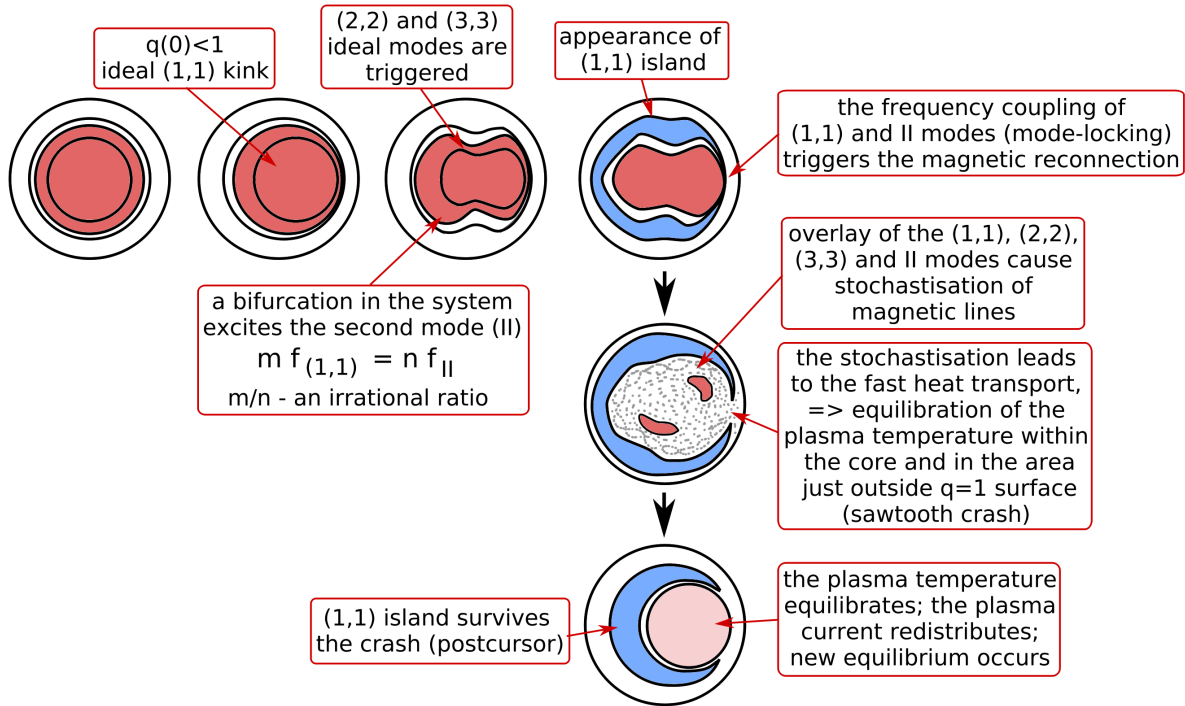


Figure 2.21: An artistic representation of the stochastic model (an example). The model describes the sawtooth crash evolution.

crash, but all of the temperatures are lost during the stochastic phase.

**Criticism of the Stochastic model:** The global stochasticity of the magnetic field may not be the dominant mechanism for the transport of the core heat, since the heat ejection pattern is high collective (for example, the measurements in Chapter 5).

### 2.3.8 Ballooning model

Involvement of ballooning modes in the evolution of the sawtooth crash in high- $\beta$  plasmas was discussed by the authors [Park et al., 1995, Nagayama et al., 1996, Nishimura et al., 1999, Munsat et al., 2007, Park, 2019]. The crash starts by magnetic reconnection, triggered by nonlinear evolution of the (1,1) ideal kink mode. The (1,1) magnetic reconnection process induces nonlinearly unstable high- $n$  ballooning modes ( $m/n \neq 1/1$ ). The (1,1) magnetic island modifies the pressure profiles and generates unstable states for ballooning modes. Due to ballooning modes, a region of hot plasma at the bad curvature side of the tokamak (low field side) will bulge out. The ballooning modes can break the helical symmetry and thereby induce magnetic stochasticity. The stochasticity leads to the rapid radial heat transport in the plasma core area. The temperature in the core equalizes before the completion of the magnetic reconnection. The (1,1) island remains after the crash.

[Nishimura et al., 1999] suggested that high- $n$  ballooning modes affect the processes in the thin current layer of the magnetic reconnection. For example, the ballooning modes

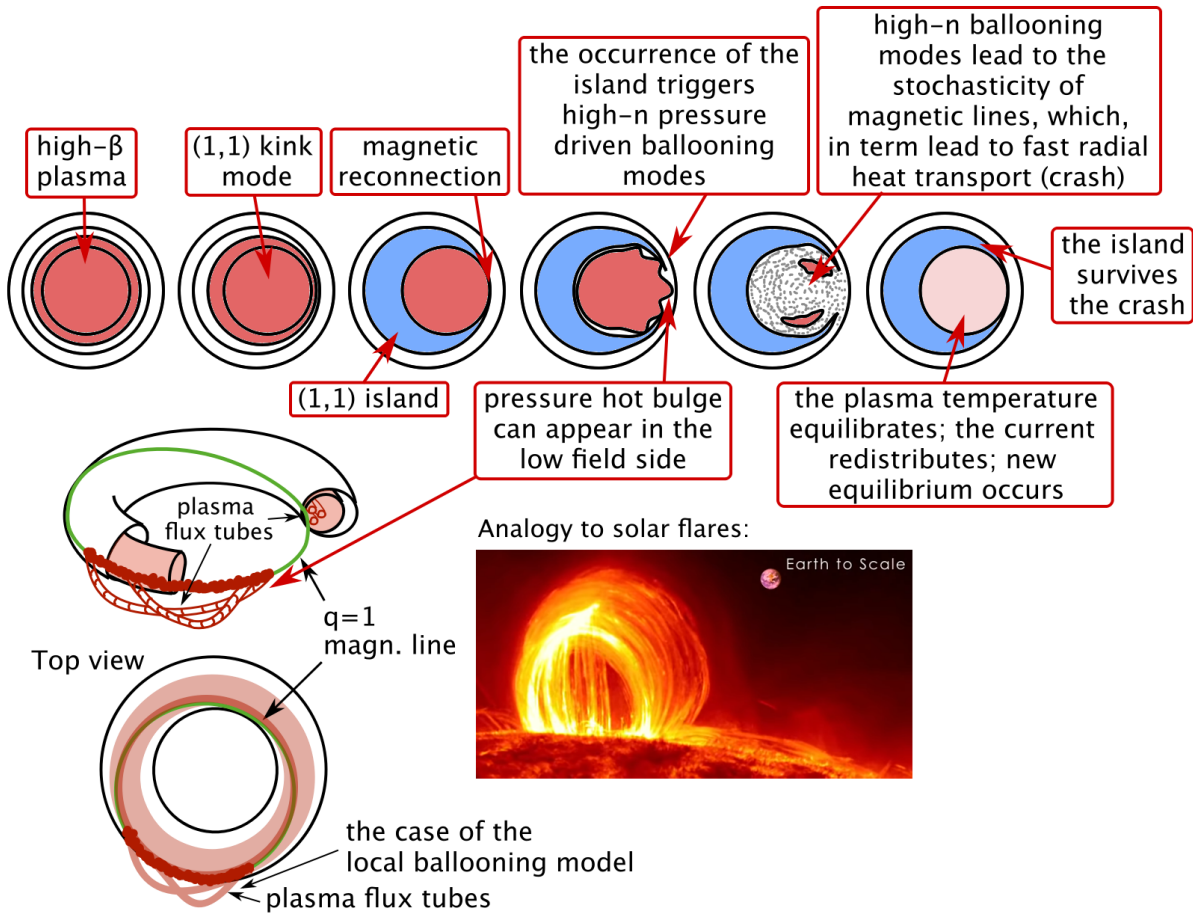


Figure 2.22: Artistic representation of the ballooning model. The model describes the sawtooth crash evolution.

displaced across this current layer can destroy effects such as electron inertia.

**Criticism of the Ballooning model:** The crash process is not modelled. There are no modern toroidal high- $n$  simulations. During the conducted simulations in the past, the heat propagation has not been modelled.

### 2.3.9 Postcursor

Sawtooth crashes in ASDEX Upgrade are always exhibiting a postcursor mode (a mode that exists after the crash or "survives" the crash). A postcursor is also observed in other tokamaks (JET [Westerhof et al., 1989], TEXTOR [Udintsev et al., 2005], TCV [Sauter et al., 2002] EAST [Hussain et al., 2021]). This means that the magnetic reconnection is incomplete. Currently, there is no consensus on why the reconnection is incomplete. This topic is beyond the scope of this thesis.

## 2.4 Summary

In this chapter, we introduced the classical Sweet-Parker model of magnetic reconnection. The model well describes the low  $S$  ( $S < 10^4$ ) collisional plasmas, but fails to describe fast reconnection in semi-collisional and collisionless plasma. Later, we learn that two-fluid effects (Hall, electron pressure gradient and inertia), plasmoid instability and stochasticity of magnetic lines (induced by turbulence) can increase the reconnection rate to be comparable with the observed one (in space and laboratory plasmas). Then, we moved on to the guide field reconnection and its example - the reconnection during the sawtooth crash, which is the focus of this thesis. For this reconnection type, two-fluid effects (electron pressure gradient and inertia, Hall can be neglected) are the main candidates to explain the experimental reconnection rate. In contrast, plasmoids do not play a big role, and an effect from the stochastisation and the ballooning modes does not yet have an experimental confirmation.



# Chapter 3

## Diagnostic

*A noiseless patient spider,  
I mark'd where on a little promontory  
it stood isolated,  
Mark'd how to explore the vacant vast  
surrounding,  
It launch'd forth filament, filament,  
filament, out of itself,  
Ever unreeling them, ever tirelessly  
speeding them.*

---

Walt Whitman

In this chapter, a brief description of the experimental diagnostics used in this thesis is presented. The emphasis is given to the post-processing of the measured data. Digital filters and the specificity of their application in this research are discussed.

### 3.1 ASDEX Upgrade

All the experimental work in this thesis has been executed at the Axially Symmetric Divertor Experiment Upgrade (ASDEX Upgrade or AUG) [Herrmann and Gruber, 2003], a midsize divertor tokamak located at the Max-Planck-Institute for Plasma Physics in Garching, Germany. The aim of ASDEX Upgrade is to prepare the physics base for ITER and DEMO. For this purpose, essential plasma properties, primarily plasma density, plasma beta and the wall load (specifically, divertor heat flux), are matched to the conditions in a future fusion power plant. The technical specification of the ASDEX Upgrade is summarized in table 3.1.

There are about 40 types of diagnostics available in ASDEX Upgrade. Our research deals with measurements of MHD activity in the plasma core. For this purpose, four diagnostic have been mainly used: magnetic coils, soft X-ray, 1D and 2D electron cyclotron emission.

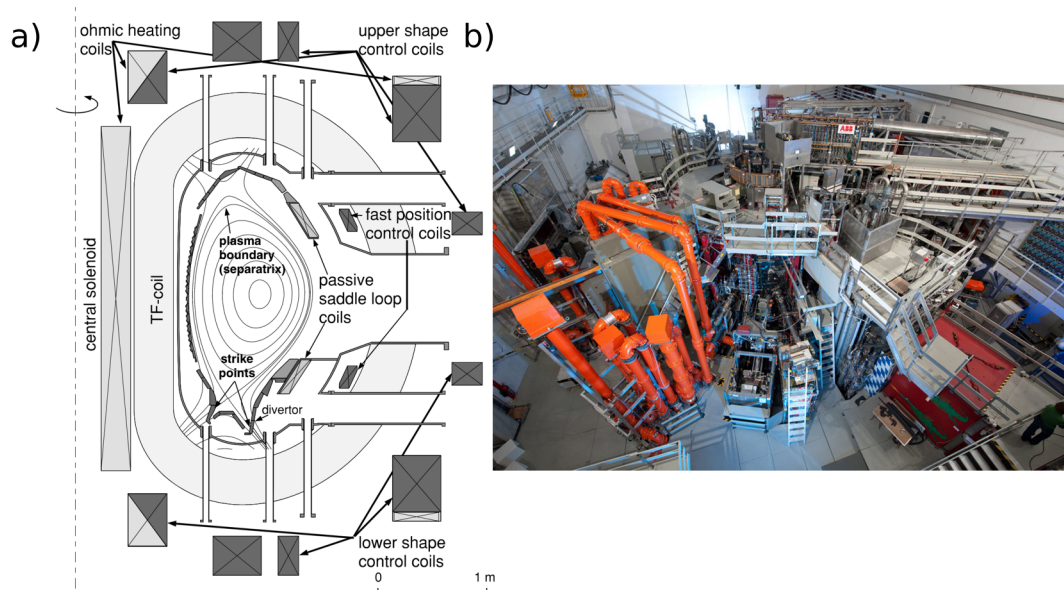


Figure 3.1: (a) Poloidal cross-section of ASDEX Upgrade [Herrmann and Gruber, 2003]; (b) a photo of ASDEX Upgrade by [Steger, 2017].

| Parameter                     | Value                              |
|-------------------------------|------------------------------------|
| Major plasma radius ( $R_0$ ) | 1.65 m                             |
| Minor plasma radius ( $a$ )   | 0.5 m                              |
| Plasma volume                 | 13 m <sup>3</sup>                  |
| Toroidal field ( $B_t$ )      | 1.5 – 3.2 T                        |
| Plasma current ( $I_p$ )      | 0.4 – 1.6 MA                       |
| Pulse length                  | 10 s                               |
| Plasma gas                    | D, H, He                           |
| Plasma ion temperature        | < 10 keV                           |
| Plasma density                | < $3 \cdot 10^{20} \text{ m}^{-3}$ |
| Energy confinement time       | < 0.2 s                            |
| Normalized beta $\beta_N$     | < 2.5                              |
| Plasma heating:               |                                    |
| Ohmical                       | $\leq 1 \text{ MW}$                |
| Neutral beam injection        | $\leq 20 \text{ MW}$               |
| Ion-Cyclotron                 | $\leq 6 \text{ MW}$                |
| Electron-Cyclotron            | $\leq 6 \text{ MW}$                |

Table 3.1: Technical specification of the ASDEX Upgrade tokamak [Herrmann and Gruber, 2003].

Even though the measurements in tokamaks are usually a rather tedious affair with many devils in the subtle details, the nature of our measurements is rather benevolent

(sawtooth instability is clearly visible in the all diagnostics, and the core plasma is optically thick for the ECE, relativistic effects can be neglected). Thus, in this work, we avoid meeting the devils and only briefly describe the measurement principles of the diagnostics used in this thesis. The emphasis is given to the signal processing of the already measured signal (post-processing).

## 3.2 Magnetic coils

In order to detect a rotating mode, the Mirnov diagnostic is used. A rotating perturbation is described by a time-varying magnetic field and therefore induces a voltage in the Mirnov coil (or pick-up coil) according to

$$U_{coil} = N_{coil} \cdot \frac{\partial}{\partial t} \int_S \mathbf{B} \cdot d\mathbf{S} \quad (3.1)$$

with  $N_{coil}$  the number of turns of the coil winding. The Mirnov coils, measuring the temporal change of the poloidal magnetic field due to their orientation, are installed inside the vacuum vessel. Figure 3.2 shows the poloidal cross section of the vessel and the coils inserted therein on the right.

One poloidal set of Mirnov coils is depicted in green and labelled with e.g. "C09-XX". This set is the Mirnov diagnostic used in this work for modelling and evaluating the measurements. The toroidal position of the poloidal set of "C09-XX" is the green line at the location "south" in the left picture of figure 3.2. The measured amplitude  $U_{coil} \sim \frac{\partial B_\theta}{\partial t}$  is proportional to the frequency of the rotating mode so that the mode amplitude is gained by dividing the signal by the frequency of the oscillation. The temporal resolution of the diagnostic is up to  $0.5 \mu s$ . In our work, Mirnov coils are used as a tool to determine the frequency of precursor and postcursor modes (before/after a sawtooth crash).

Apart from that, Mirnov coils with a combination of toroidal saddle coils allow identifying poloidal and toroidal mode numbers  $(m, n)$ . The procedure of this identification is well described in [Igochine et al., 2015, pg 53].

## 3.3 Soft X-ray

Soft X-ray radiation is emitted by photons in the energy range from approximately 250 eV to 100 keV. In a tokamak, if the plasma electron temperature is greater than 200 eV and the amount of impurities is low the influence of recombination radiation may be ignored. In this situation, the continuous spectrum is determined generally by bremsstrahlung, which arises due to the scattering of free electrons by plasma ions. However, ASDEX Upgrade has a tungsten (W) plasma-facing wall, which leads to the presence of W in the plasma. The recombination radiation of this high-Z impurity may exceed significantly the bremsstrahlung level if plasma has a high temperature and sufficient W concentration.

In ASDEX Upgrade, the soft X-ray emission is measured by a set of diodes. Each diode observes the emission along a line of sight (LOS), providing line integrated measurements

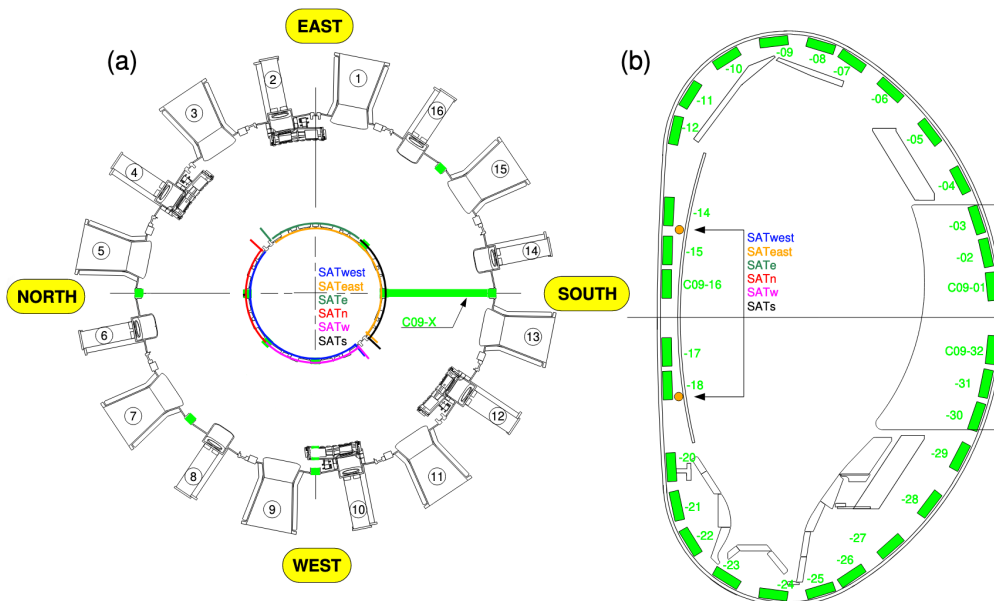


Figure 3.2: Toroidal (a) and poloidal cross-section (b) of ASDEX Upgrade with the Mirnov coils in green, the poloidal cross-section shows the flange contour with 30 Mirnov coils "C09-XX" corresponding to the green section at the location "south" in the toroidal cross-section. Six saddle coils SAT\* are located in the high field side of the tokamak, around the central solenoid.

of the plasma emissivity. The soft X-ray diagnostic in ASDEX Upgrade consists of 15 miniature heads with separate pinholes and chips, assembled to 8 cameras named F, . . . , M resulting in a total of 209 LOSs (figure 3.3). The temporal resolution of the diagnostic is up to  $0.5 \mu\text{s}$ .

The time evolution of the X-ray flux provides information about MHD activity during a discharge. In our work, Soft X-ray diagnostic is used as a tool to determine the frequency of precursor and postcursor modes (before/after a sawtooth crash).

Tomography inversion is a technique that permits the reconstruction of the local emissivity from the line integrated brightness. Tomography is a naturally ill-conditioned problem, which means that the reconstructed profile is not a unique solution and the solution's behaviour does not change continuously with the changes in the measurements (in other words, a small perturbation in the measurements can cause unacceptably large errors in the tomographic reconstruction). Unfortunately, 209 LOS of SXR in ASDEX Upgrade is not sufficient to confidently reconstruct the highly local reconnection region of sawtooth crashes (it is sufficient for a good reconstruction of the precursor evolution [Vezinet et al., 2016]).

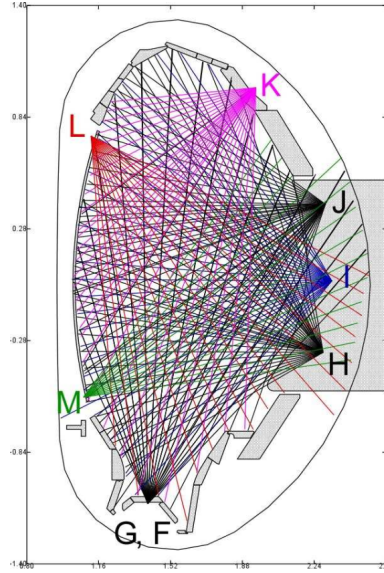


Figure 3.3: Shown is the projection of the Soft X-ray lines of sight to the poloidal cross-section, in which the camera pinhole is located. All cameras are plotted in one figure. The component of the lines-of-sight perpendicular to this plane (i.e., in toroidal direction) is very small. The divertor cameras G and F have identical poloidal positions. The figure is taken from [Igochine et al., 2010b].

### 3.4 ECE

Electron Cyclotron Emission radiometry is a diagnostic that measures the radial electron temperature profile  $T_e$  in tokamaks. The physical principle of the diagnostic is explained as follows. Electrons gyrate in the presence of the applied magnetic field and emit electromagnetic radiation. This radiation is emitted at the characteristic electron cyclotron frequency  $\omega_{ce}$  and its low  $n$  harmonics [Hutchinson, 2002, pg 155]:

$$\omega = \omega_{ce} = n \frac{eB_{tot}}{m_e} \quad (3.2)$$

where  $e$  and  $m_e$  are electron charge and mass at rest,  $B_{tot}$  is the sum poloidal and toroidal magnetic field and  $c$  is the speed of light. Since in a tokamak  $B_{tot}$  is dominated by the toroidal magnetic field  $B_{tor}$ , which depends on  $1/R$ , the emitted frequency can be associated with a distinct radial position  $R$  and a spatially resolved measurements is possible:

$$\omega = n \frac{eB_0 R_0}{m_e R} \quad (3.3)$$

where  $B_0$  is the toroidal magnetic field at the plasma center  $R_0$ . Normally, the plasma within the core is optically thick for the electron cyclotron frequency and its harmonics. At this frequency, plasma behaves like a black body and follows the Planck curve. The electron emission in plasmas occurs at long wave length, therefore, the intensity distribution

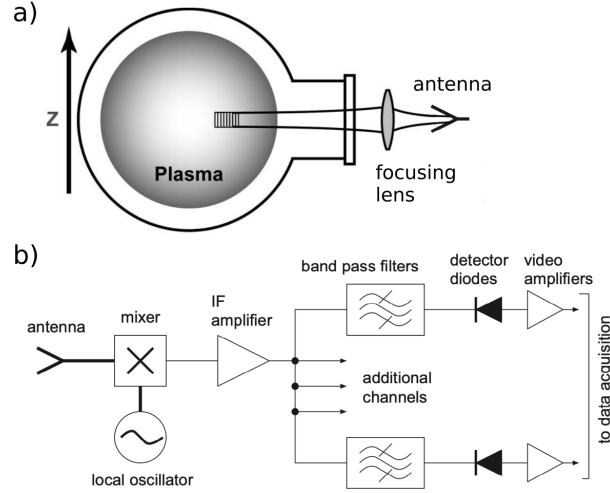


Figure 3.4: Schematic diagram of the physical layout of ECE system is shown in (a). A schematic of a broadband multichannel heterodyne radiometer for ECE measurements is shown in (b). The figures are adapted from [Munsat et al., 2010, Rathgeber, 2013].

$I_n(\omega)$  can be described by the Rayleigh-Jeans law. In this case, the radiation temperature reflects the electron temperature [Hutchinson, 2002, pg 155]:

$$I_n(\omega) = \frac{\omega^2 T_e}{8\pi^3 c^2} \quad (3.4)$$

Thus, the temperature profile is obtained as:

$$T_{rad}(\omega) \sim T_e(\omega) = 8\pi^3 c^3 \frac{I_{BB}}{\omega^2} \quad (3.5)$$

The calibration of the measurements is done between the wave intensity  $I_{BB}$  and the detector output voltage  $V$  ( $V \propto I_{BB}$  due to the detection scheme of figure 3.4, where the detector diode voltage is proportional to the IF power into the diode). The calibration thus includes antenna pattern, power losses in waveguides, mixer conversion efficiency, IF gain and detector diode sensitivity.

The radiation temperature equals the electron temperature of plasma ( $T_{rad}(\omega) = T_e(\omega)$ ) only within the black body approximation. At low densities, especially at the plasma edge near or outside the separatrix, the plasma is optically thin and the assumption of a black body is not valid. However, this limitation is of no concern in our work, since all our measurements have been conducted in the plasma core, where plasma is optically thick and the black body approximation is applicable. Another limitation of the ECE is the so-called "cut-off" [Hartfuss et al., 1997a][Hutchinson, 2002, pg 177]. Only waves with a frequency higher than the cut-off frequency can propagate in the plasma otherwise they are reflected inside the plasma volume and do not reach the receiver outside the plasma. In modern tokamaks, the first harmonic of the electron cyclotron radiation is usually below

the plasma cut-off frequency, that is why the second harmonic is commonly used for the ECE measurements.

In a modern ECE diagnostic, multichannel heterodyne receivers [Hartfuss et al., 1997a] are used to measure the plasma radiation (figure 3.4). These receivers permit the simultaneous measurement of ECE at different frequencies and absolute temperature calibration. In the heterodyne system, a single or two-stage down-converter is required to process the high-frequency signals to a convenient intermediate frequency (IF) for final detection. The down-converter consists of a fixed frequency local oscillator (LO) and a mixer. The mixer converts high-frequency radiation to lower frequencies by combining the signal with the constant LO signal in a nonlinear element to produce sum and difference frequencies. The difference frequency is usually a lower intermediate frequency (IF) which can be easily amplified and frequency separated, and have other signal processing performed on it.

The profile ECE diagnostic at ASDEX Upgrade uses a heterodyne radiometer with 60 available channels. It measures the second harmonic radiation with a 1 MHz sampling rate. For a standard 2.5 T field configuration, the radial resolution of the edge channels is about 5 mm. The intermediate frequency bandwidth for each edge channel is 300 MHz. With an IF bandwidth of 600 MHz the core channels have a spatial resolution of about 12 mm. Profile ECE is absolutely calibrated. In our work, 1D ECE diagnostic is used, first, as a tool to determine the frequency of precursor and postcursor modes (before/after a sawtooth crash); second, as a cross-calibration of the plasma temperature between 1D and 2D ECEI.

The measurement principles of the 2D ECE (or ECE-Imaging) system are the same as for the 1D system. The systems differ in the area that they can measure. 1D ECE diagnostic provides a profile of the radiation temperature along with a single line of sight (LOS), while 2D ECE diagnostic uses several LOS and provides with 2D picture (image) of plasma radiation temperature.

### 3.4.1 ECEI

The optical system of the electron cyclotron emission imaging (ECEI) diagnostic of ASDEX Upgrade is shown in figure 3.5a. In addition to radial resolution, which is provided as in all ECE systems through frequency selectivity, the ECEI also has poloidal resolution. This is accomplished by quasi-optical imaging of the observation field onto an array of 16 mixer diodes through a system of three lenses. A single local oscillator (LO) is fed via a quasi-optical arrangement of mirrors and lenses to the same mixer array. The shaping of plasma radiation is done by three lenses. The first two lenses are common for both ECEI and ECE systems, while the third one is used only for ECEI and is moveable to bring the EC radiation of various radial regions into focus at the detector array. Several notch filters are applied to filter out the 140 GHz from ECRH to avoid overloading the mixer diodes with ECRH stray radiation. A dichroic plate, placed immediately before the detector array, acts as a high-pass filter to select the upper sideband. The optics next to the LO is used to make the LO beam elongated and optimally cover all the 16 detector diodes (corresponding to 16 lines of sights (LOS) or 16 vertical positions of plasma measurements). In these diodes

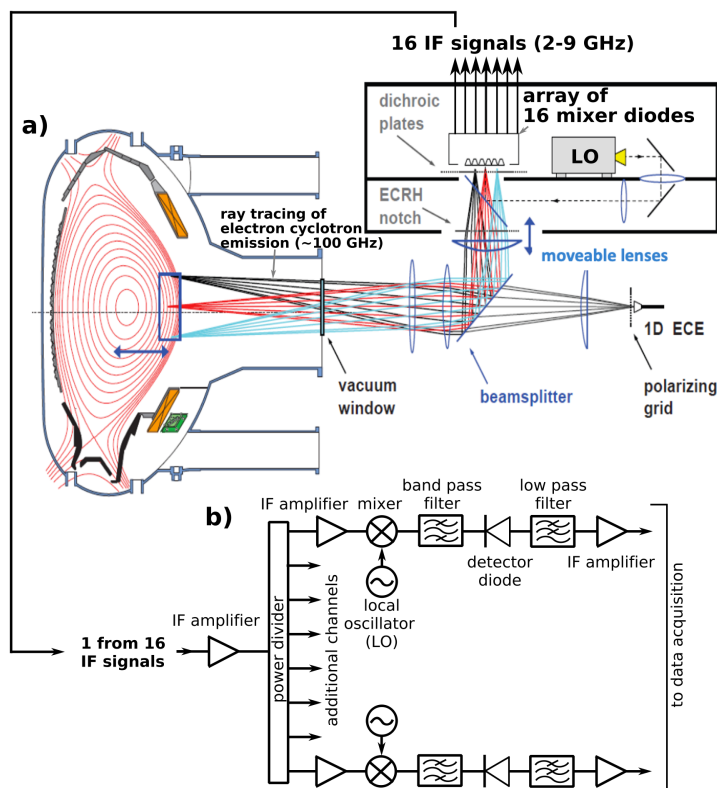


Figure 3.5: Overview of the optical path constructed with a lens set up of ECE and ECE imaging systems is shown in a). The first two lenses after the vacuum window are common for both ECE and ECE imaging. The beam splitter separates the signal into two portions. The portion of the signal that is reflected goes into the arrays of mixer diodes for the ECE Imaging. With the movable lens, it is possible to shift the focus in the plasma. The schematic layout of the ECE-Imaging electronics is shown in b). The signal is downconverted two times. The first time at the array, by mixing the plasma and the local oscillator (LO) signals (shown in a)). The emission from plasma comes from 16 lines of sight (LOS). In each LOS, the signal of microwave frequency ( $\sim 100$  GHz) downconverted to the signal of the intermediate frequency (IF,  $\sim 1 - 8$  GHz). Afterwards, the downconverted signal is divided into 8 portions, as shown in (b). These portions are mixed with 8 local oscillator signals in the second downconversion step. The resulting signals are band pass filtered, determining the bandwidth  $B_{IF}$  and hence the radial resolution of ECE-Imaging. After detection, the signals are low pass filtered, determining the video bandwidth  $B_V$  and hence the time resolution of ECE-Imaging. The figure is adapted from [Classen et al., 2007, Classen et al., 2010, Vanovac, 2019].

the LO and plasma beams are mixed. The mix results in the sum and difference of LO and plasma beams frequencies. The difference frequency is a lower intermediate frequency (IF). This is the first stage of the frequency down-conversion. The 16 intermediate down-converted signals are then amplified and passed to the IF electronics. One of sixteen IF

modules is shown in 3.5b. In the module, the signal is divided into 8 different channels and down-converted for the second time. This differentiation allows separating the signals by their radial origin in the plasma so that these 8 channels correspond to the 8 radial positions. Thus, we obtain a window of the radiation temperature measurements with 16 vertical lines each having 8 radial positions (16x8=128 signals). The IF bandwidth  $B_{IF}$  is 700 MHz, which limits the radial resolution of the diagnostic to about 12 mm. In the next step the signals are low pass filtered with the video bandwidth, which is usually half of the sampling frequency (set to 200 kHz in our measurements), and then digitized.

### 3.4.2 Noise

In thermal equilibrium, under the assumption that the plasma is optically thick, the radiation temperature coincides with the electron temperature. The error bars of the measurements are determined by the statistical fluctuations of the signal, received by the ECE radiometer. These fluctuations are associated with black-body noise because the emission from the plasma is a superposition of many incoherent waves and is called thermal noise and it has a Gaussian distribution. This wave noise dominates over the instrumental noise in both ECE and ECEI diagnostics of ASDEX Upgrade. The level of thermal noise is determined by the spatial  $B_{IF}$  and temporal  $B_V$  bandwidths of the system [Hartfuss et al., 1997a]:

$$\frac{\delta T}{T} = \sqrt{\frac{2B_V}{B_{IF}}} \quad (3.6)$$

It can be seen from equation 3.6 that increasing  $B_V$  (better time resolution) and decreasing  $B_{IF}$  (better spatial resolution) increases the thermal noise level.  $B_V$  and  $B_{IF}$  settings of ECEI in ASDEX Upgrade are 200 kHz and 700 MHz, respectively. This translates into a relative root mean square (r.m.s.) noise level of 2.4 %.

### 3.4.3 Digital filtering of the noise

As one can see from equation 3.6, the signal-to-noise ratio can be improved by choosing the lowest possible video bandwidth and highest possible IF bandwidth, observing simultaneously the signal bandwidth and the required radial resolution. The video bandwidth can easily be adapted to the observed signal bandwidth by a fast sampling of the video signal, followed by digital filtering. However, there are cases when this option is unavailable. For example, when an already measured signal has to be used and analyzed. In that case, digital signal processing is useful to employ.

In this thesis, digital filters are used to reduce the thermal noise in the ECE images of the measured sawtooth crashes. More than 500 crashes were analyzed. The reduction of the noise and, thus, making the studied physical phenomena more visible helps both in speeding up the manual interpretation of the measurements and in creating a computer routine to automate the analysis.

A filter profile that we need can be portrayed through the following points:

- **Filter purpose:** maximize the signal-to-noise ratio of the studied phenomena (the movement of the plasma core) in the ECE images.
- **The signal to be measured (phenomena of observation):** the (1,1) mode rotation, localization and dynamics of sawtooth crashes.
- **The noise to be filtered:** thermal noise (white noise), Gaussian distribution.
- **Filter requirements:** temporal resolution preserving (no lowpass filter); available in the existing libraries (Python, Matlab) as free and open-source; simple to implement; the signal distortion produced by the filter is negligible in comparison to the signal amplitude of the studied phenomena; zero group delay.

The measured signals can be represented in 1D and 2D data sets (figure 3.13). The one-dimensional data is the radiation temperature measured at a particular plasma point versus the measurement time. The two-dimensional data is a grid of the 8x16 ECE channels (or an image with 8x16 pixels) at a particular time point. In a grid, each channel benefits from the surrounding channels when the phenomenon of observation is bigger than the distance between the channels. A "misbehaving" channel can be recovered from the "courtesy" (i.e. by interpolation) of the surrounding ones. In the literature, the digital filters for 1D and 2D data are split into two theoretical fields - Digital Signal Processing and Digital Image Processing, respectively. We will follow suit.

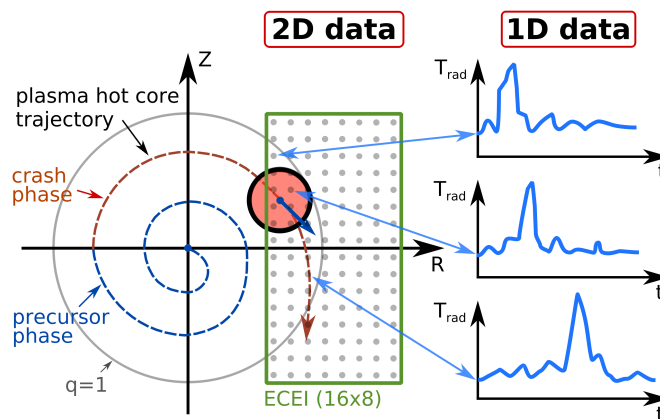


Figure 3.6: The difference between the 1D and 2D measured data.

### — Filters for 1D data —

One dimensional filters can be classified in many ways as can be seen in the textbook on the subject [Lyons, 1997, Proakis, 2001, Vaseghi, 2008, Smith, 2013, Lathi and Green, 2014, Tan and Jiang, 2018, de Cheveigné and Nelken, 2019]. However, I could not find a classification suitable for the goals of this thesis. Therefore, an unconventional classification of the 1D digital signal filters is proposed in figure 3.7 (based on the literature listed in

the first sentence of the paragraph). For a good description of each filter group from this figure, the reader refers to: moving interval in time domain [Lyons, 1997, pg 411][Smith, 2013, pg 261], eigenvalue [Henry and Hofrichter, 1992], transforms [Tan and Jiang, 2018, pg 91,143] [Lyons, 1997, pg 45,361][Proakis, 2001, pg 147][Smith, 2013, pg 551], Bayesian [Candy, 2016][Vaseghi, 2008, pg 107], and adaptive [Brown and Hwang, 1997][Tan and Jiang, 2018, pg 421][Proakis, 2001, pg 823,880][Vaseghi, 2008, pg 193]. Types of noise: [Vaseghi, 2008, pg 35].

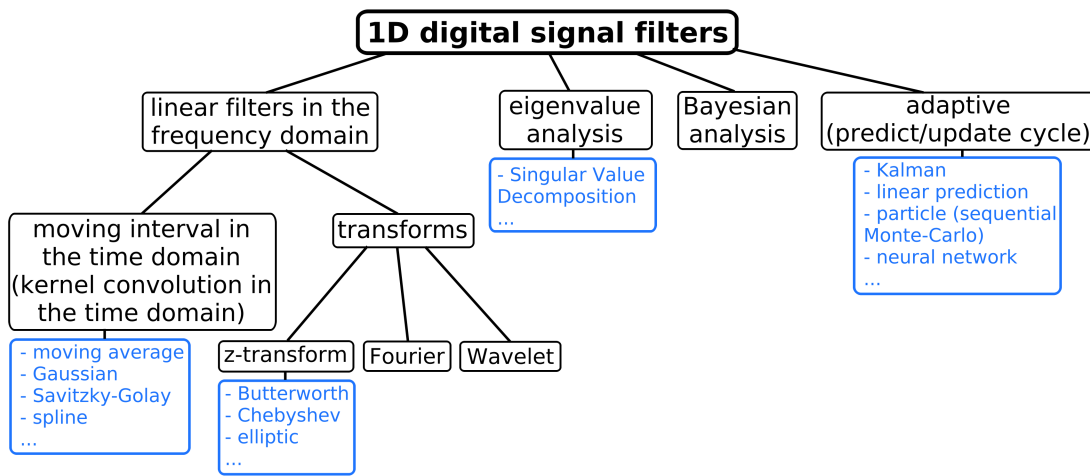


Figure 3.7: Classification of 1D digital noise filters.

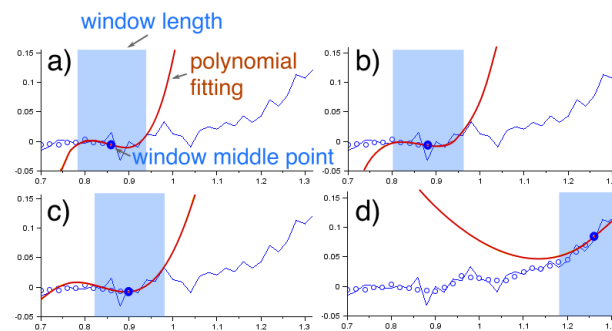


Figure 3.8: An illustration of Savitzky-Golay filter.

In our study, the measured signal has a much larger amplitude than the noise, so a small ”decorative” smoothing of the noise would suffice. Complex filters (such as z-transform, the Bayesian and adaptive group; see figure 3.7) usually have better noise cancellation but are time-consuming to implement and have elusive principles of work. Furthermore, any digital filter apart from its main function brings a distortion of a signal [de Cheveigné and Nelken, 2019]. The signal distortion from the complex filters is imperceptible and has to be analyzed. Thus, Bayesian, Wavelet, z-transform and adaptive filters are found to be too complex (time-consuming) to implement for our goals.

The following filters have been tested: Savitzky-Golay [Schafer, 2011], Singular Value Decomposition (SVD), and Fourier filters. Fourier filters brought clearly visible distortion of the observed signal. Generally, SVD accumulates signal in the top significant eigenmodes. It does not reduce noise in the individual eigenmodes. In some cases, only few eigenvectors matter, then one can expect an increase of the signal-to-noise ratio in those few top significant eigenmodes. For our data, SVD filter was found to be ineffective to increase the signal-to-noise ratio. Savitzky-Golay was found to be "good enough" for us: reduce the noise, produce no visible distortion, preserve temporal resolution and has clear principles of work.

The Savitzky-Golay filter uses least squares to regress a small window of your data onto a polynomial, then uses the polynomial to estimate the point in the center of the window (illustrated in figure 3.8). Finally, the window is shifted forward by one data point and the process repeats. This continues until every point has been optimally adjusted relative to its neighbours. The filter is defined by two values - window size and the order of the polynomial fitting.

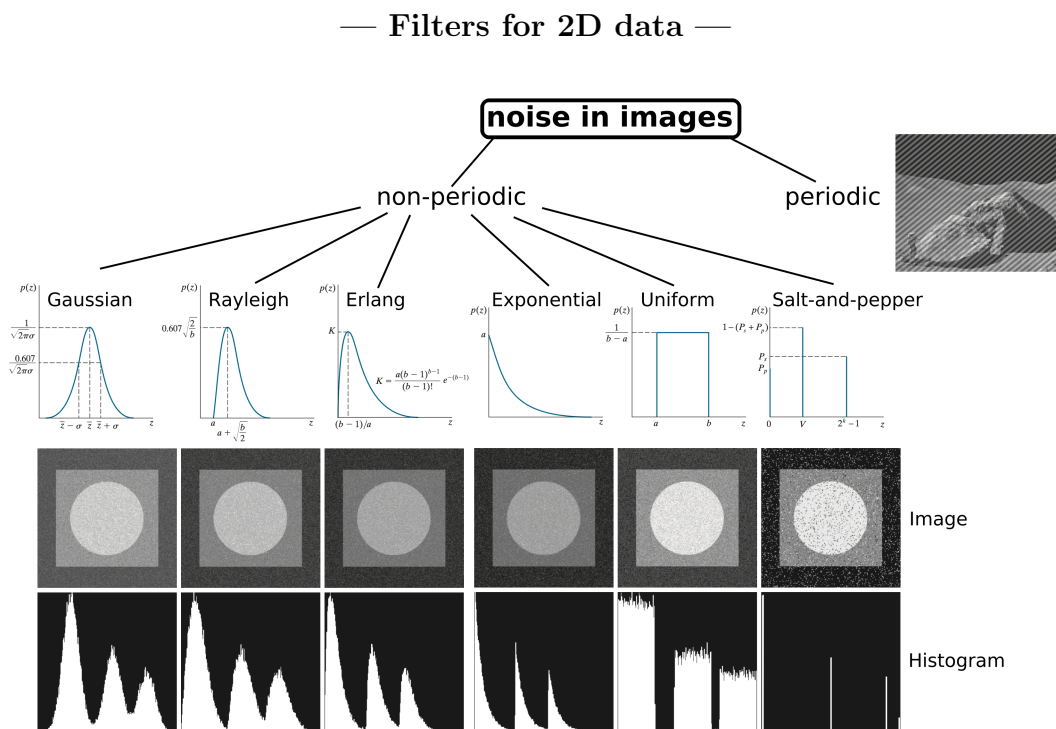


Figure 3.9: Most common types of noise in images. The figure is adapted from [Gonzalez and Woods, 2018, pg 317]

Image restoration (or denoising) filters are well described in [Smith, 2013, pg 373][Tan and Jiang, 2018, pg 652][Aja-Fernández and Vegas-Sánchez-Ferrero, 2016, Gonzalez and Woods, 2018]. The common procedure of image denoising is, first, determining the noise type (this can be done via the image histogram as shown in 3.9), then choosing a kernel

filter (also called convolution matrix or mask) and its size suitable for the noise type. For our application, the filter classification can be limited to two types (figure 3.10): (a) mean filters, which are used for Gaussian and uniform noise; (b) order-statistic filters, which are used for salt and pepper noise (useful if we have a broken channel in the ECEI grid). These two types can be modified with the adaptive scheme, that is used to preserve the edges (or reduce distortion or artifacts sometimes produced in the edges).

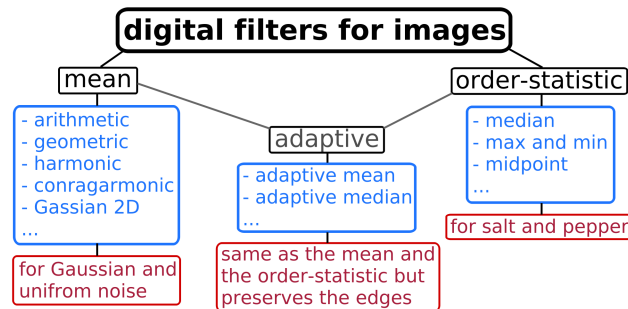


Figure 3.10: A classification of the commonly used denoising image filters.

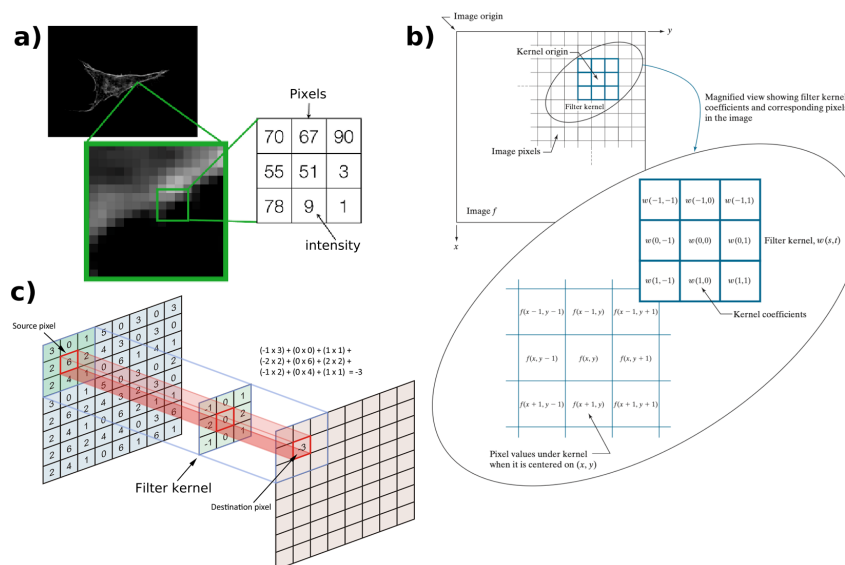


Figure 3.11: An explanation of the working principle behind denoising image filters. An image is a matrix of pixels (a). A linear denoising filter consists of a filter kernel and the kernel function (b). They act on the original image through convolution of the kernel and the image matrices. An example of a convolution (c). The figures are adapted from [Gonzalez and Woods, 2018, pg 155] and [Con, 2017].

The working principle behind a linear denoising filter is shown in figure 3.11. An image consists of pixels and each pixel may be represented with a value (figure 3.11a). The grid of these pixels is the original matrix that we want to modify to reduce the noise. This

procedure is done with a convolution process via a kernel (figure 3.11b). The size and the kernel function determine the output of the convolution (i.e. the denoising effect that a given filter produces). An example of the application of a filter kernel is shown in figure 3.11c.

For our data, which has the Gaussian noise, the following image filters have been tried: Gaussian, bilateral, total variation, mean arithmetic and geometric (all these filters are available as free and open-source in the python library `scipy-ndimage`). Two kernel shapes have been used: 3x3 square and 3x3 cross. Only the Gaussian filter (kernel has the Gaussian distribution) is found to be suitable for our goals, the other filters produced undesirable image artifacts (which may lead to misinterpretation of the physics) along with the denoising.

The Gaussian filter is well described in [Gonzalez and Woods, 2018, pg 166]. In brief, the kernel function has the form  $w(r, \sigma) = const \cdot e^{-\frac{r^2}{2\sigma^2}}$ , where  $r$  is the distance from the kernel center,  $\sigma$  is the standard deviation of the Gaussian distribution. The kernel usually has the size of the original image matrix with  $\sigma$  determining the efficient radius of this kernel (the contribution of the pixels further than  $3\sigma$  is negligible). The Gaussian kernel calculates the weighted average of the pixel values that are inside the kernel. The weights are determined by the distance from the kernel center and the standard deviation  $\sigma$  value. The pixels close to the kernel center contribute most significantly to the resulting value.

An example of the application of the Savitzky-Golay filter and the Gaussian Image filter is presented in figure 3.12.

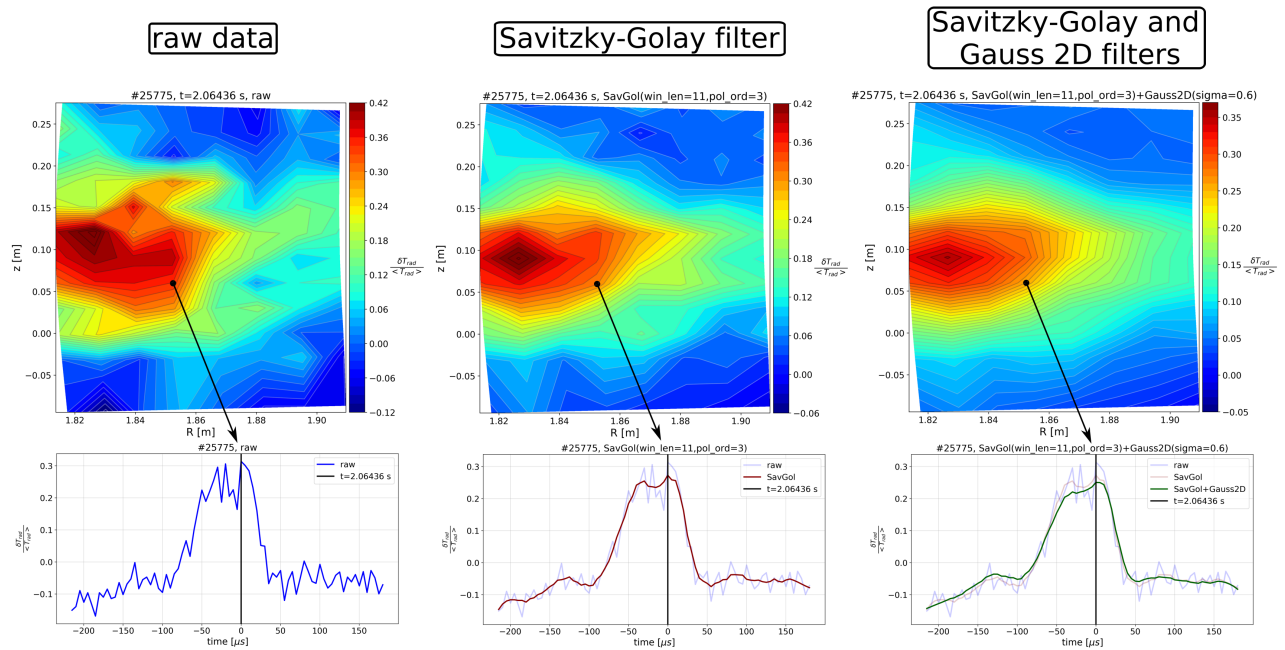


Figure 3.12: An example of the application of Savitzky-Golay and Gauss 2D filters to the ECEI data.

### 3.5 Summary

As a summary, in figure 3.13 we present the toroidal view of ASDEX Upgrade with the diagnostics and their purposes used in this thesis.

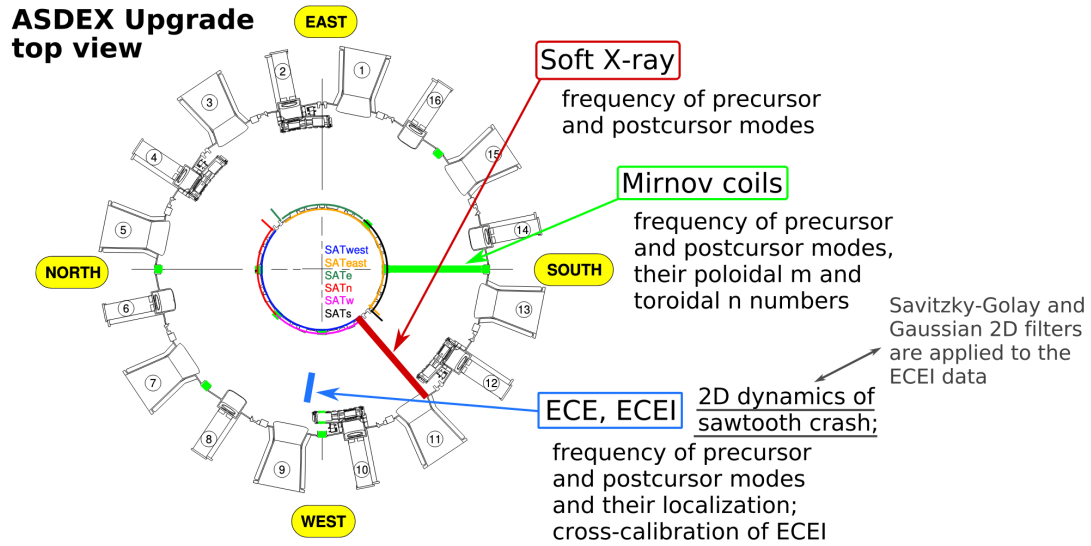


Figure 3.13: Toroidal locations of the used diagnostics and their application in our work.



# Chapter 4

## Global nature of magnetic reconnection during sawtooth crash

(Chapter is adapted from the paper published in the JPP [Samoylov et al., 2022a])

*Doubt is an uncomfortable condition,  
but certainty is a ridiculous one.*

---

Voltaire

This chapter discourses about the toroidal localization of the magnetic reconnection during sawtooth crash.

### 4.1 Introduction

During a sawtooth crash, experimental observations clearly show that the hot plasma core ( $q \leq 1$ ) rapidly expels into the outer layers ( $q > 1$ ). At the same time, it is still unclear whether the crash is symmetric along the helical axis (global, everywhere along the  $q = 1$  helical line) or helically localised (local, in a particular place at the  $q = 1$  line). A graphical representation of these two possibilities is shown in figure 4.1. While most of the research published on sawtooth instability assumes that the crash occurs globally, there are multiple publications that report an observation of helical localisation of the crash [Nagayama et al., 1996, Munsat et al., 2007, Park, 2019]. The ballooning effect [Park et al., 1995] and secondary instabilities [Bussac et al., 1984, Bussac and Pellat, 1987, Gimblett and Hastie, 1994] were suggested [Munsat et al., 2007] as a cause of the local reconnection.

To study the localization of the reconnection processes in a torus, a three-dimensional consideration is necessary. In the following, we list the existing sawtooth crash models (these models are described in section 2.3) with their dimensional descriptions of the phenomenon:

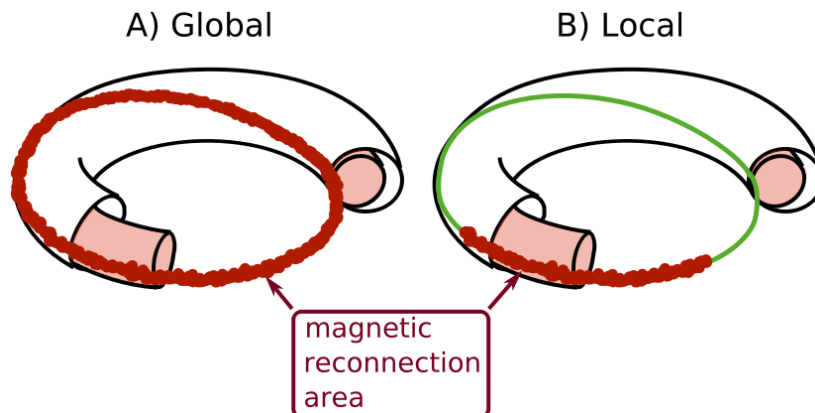


Figure 4.1: An artistic representation of the difference between global and local sawtooth crash. The global crash is shown in "A)" - where magnetic reconnection occurs everywhere along the  $q = 1$  magnetic line. The local crash is shown in "B)" - where magnetic reconnection occurs only on a particular local place along the  $q = 1$  magnetic line.

- Kadomtsev [Kadomtsev, 1975]: 2D ("2D" denotes a plasma model that has a two-dimensional poloidal and axisymmetric toroidal description; "3D" denotes a plasma model that is described with three-dimensional geometry), global
- Ballooning [Bussac and Pellat, 1987, Park et al., 1995]: 3D, global and local are possible
- Quasi-interchange:
  - Wesson [Wesson and Campbell, 2011]: 2D, global
  - Jardin [Jardin et al., 2020]: 3D, global
- Stochastic [Lichtenberg et al., 1992, Igochine et al., 2006b, Igochine et al., 2008] [Yu et al., 2015]: 3D, global

To simulate a sawtooth crash numerically, one needs to use two-fluid, non-linear MHD codes in 3D geometry, which is a numerically expensive task. To reduce the numerical load it is a common approach to neglect the contribution of high toroidal mode numbers, which makes the reconnection global. The authors are aware of only three numerical studies on the ballooning effect influence on sawtooth crash with an assumption of the local magnetic reconnection: Ref. [Baty et al., 1992] (one fluid MHD), Ref. [Park et al., 1995] (MH3D code [Park et al., 1992], one fluid MHD) and [Nishimura et al., 1999] (one fluid MHD, heat conduction parallel to the magnetic field is ignored). The authors are not aware of any recent numerical studies that simulate helically local magnetic reconnection during a sawtooth crash and include all important physical effects (two-fluid MHD, non-linear, plasma resistivity, high toroidal mode number, realistic Lundquist number ( $S > 10^7$ )).

In the following sections, we (i) assess the possibilities of the localized crash measurements in ASDEX Upgrade; and (ii) analyse the experimental data with a purpose to detect global/local crash events.

## 4.2 Can a toroidally localized crash be measured?

During a sawtooth crash, there is an opening through which magnetic lines from the plasma core ( $q < 1$ ) reconnect with magnetic lines in the outer plasma layers ( $q > 1$ ) (shown in red in figure 4.1). The hotter core plasma mixes with colder plasma in the outer layers through this opening to form a "heat bridge". The heat manifests itself in the cyclotron radiation, which can be measured. To find out what the difference between the heat distribution in the local and global crash cases (and afterwards potentially to confirm this difference experimentally), we conduct a numerical study.

To simulate the heat redistribution during a sawtooth crash, we used the GRILLIX code [Stegmeir et al., 2018]. The GRILLIX code is able to solve the heat diffusion equation in axisymmetric cylindrical geometry with a constant in time magnetic field profile:

$$\frac{dT}{dt} = \chi_{\parallel} \nabla_{\parallel}^2 T + \chi_{\perp} \nabla_{\perp}^2 T \quad (4.1)$$

We assume a local sawtooth crash with a three-dimensional Gaussian heat source along the  $q = 1$  helical magnetic line (figure 4.2: a). The source has the following dimensions (full width at half maximum):  $\approx 5.8 \text{ cm}$  in  $r_x$  and  $r_y$  coordinates (a typical size of X-point during sawtooth crash in ASDEX Upgrade),  $\approx 50^\circ$  of toroidal angle along  $q = 1$  magnetic line. Realistic plasma parameters and dimensions were used: tokamak major radius  $R_0 = 1.65 \text{ m}$ , radius of  $q = 1$  magnetic surface  $r_{q=1} = 0.15 \text{ m}$ ) as well as a realistic ratio of parallel and perpendicular heat transport coefficients  $\frac{\chi_{\parallel}}{\chi_{\perp}} = 2 \cdot 10^8$  (estimated in Appendix B). The used  $q$  profile is shown in figure 4.2: b. The code is limited to a constant in time  $q$  profile, which is a good assumption for the initial phase of the heat redistribution. Thus, we are able to simulate the initial phase of the sawtooth crash when the reconnection just starts. As we will show, this simulation is sufficient to make a conclusion about the heat redistribution at the first stage of the crash.

In figure 4.2(a), we show two poloidal cross-sections of a tokamak (marked as "A" and "B"), which are located toroidally 180 degrees apart. We observe both cross-sections during our simulation: in "A" we locate the centre of the heat source, whereas in "B" we observe the speed and manner of the heat redistribution. The result of this simulation is shown in figure 4.2(c). The helically localised heat source redistributes itself in a helically symmetric manner during  $\approx 100 \text{ ns}$  time due to the high heat conductivity of electrons along the magnetic field lines. Variation of the safety factor profile from  $q_0 = 0.6$  (high magnetic shear) to  $q_0 = 0.999$  (low magnetic shear) does not change the result. The result is also robust with respect to the toroidal extent of the localized reconnection zone along the  $q = 1$  line (heat source in 4.2a). Even in the case of a narrow "single point" reconnection width, the result remains the same.

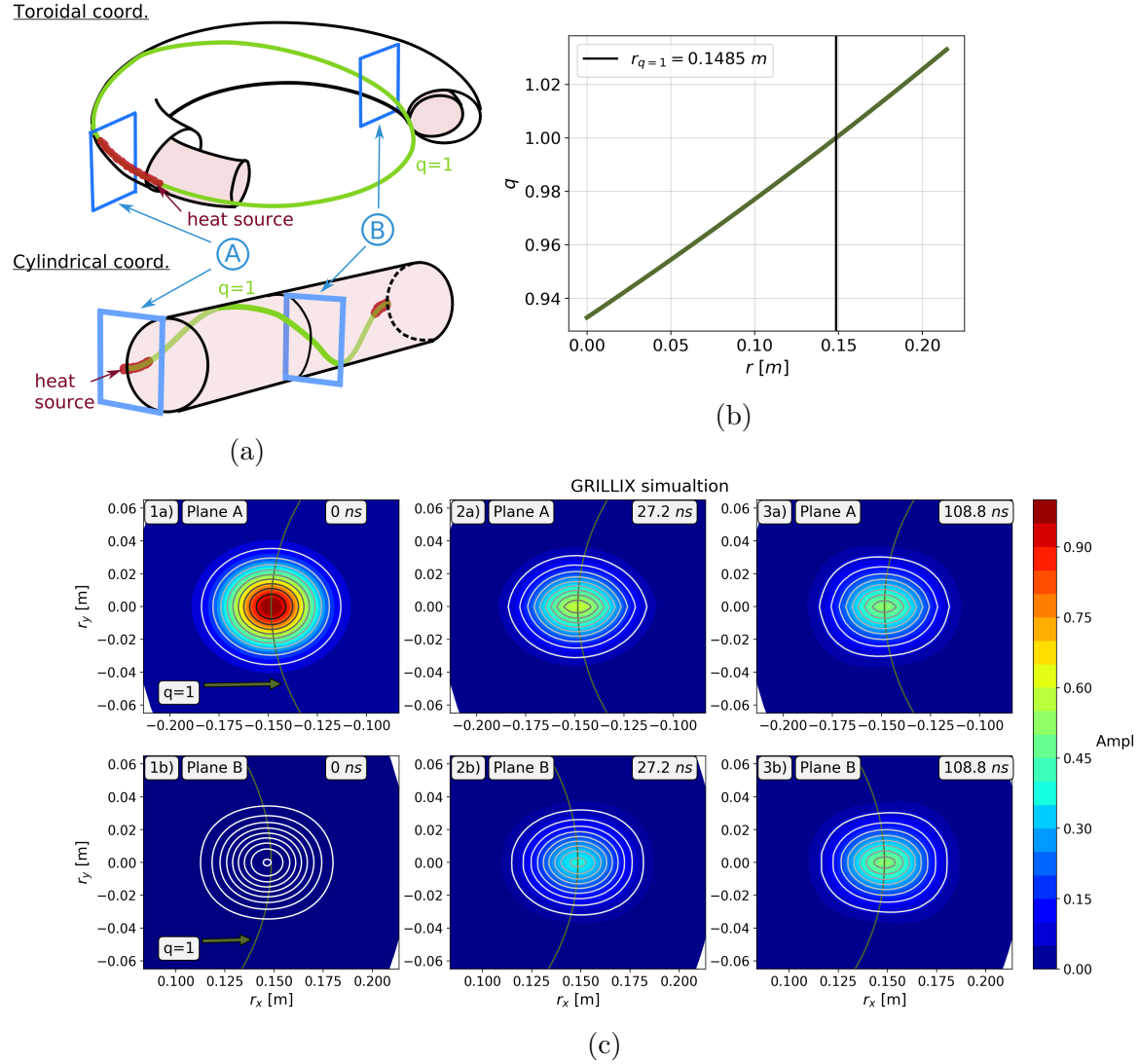


Figure 4.2: Simulation of heat distribution at the beginning of a sawtooth crash with GRILLIX. In (a), an artistic representation of the geometry is shown. The observed planes (Plane "A" and "B") are located toroidally 180 degrees apart with the heat source localised in the plana "A". In (b), the used safety factor  $q$  profile is shown. In (c), the result of the simulation is shown.

As we mentioned earlier, the GRILLIX simulation of the heat distribution assumes a constant magnetic field, which is not the case during a sawtooth crash. However, the time scales of the heat distribution ( $\tau_{heat\ dist.} \approx 0.1 \mu s$ ) and the crash ( $\tau_{crash} \approx 100 \mu s$  in ASDEX Upgrade) differ dramatically ( $\frac{\tau_{crash}}{\tau_{heat\ dist.}} = 1000$ ). This means that magnetic reconnection during the crash is practically a static process compared to the heat distribution. In other words, the electron temperature on slowly reconnected field lines would be almost immediately equilibrated. This rationale justifies the assumption of a constant magnetic

field made in the GRILLIX.

In present-day tokamaks, there is no diagnostic tool for core MHD activity with sufficient temporal resolution to trace the process of heat equilibration at a nano-second scale. To observe the localised heat redistribution, one needs to have a diagnostic with a temporal resolution in the order of tens of nanoseconds. However, the fastest temporal resolution currently available is  $\approx 1 \mu s$  (in the current paper, the temporal resolution of the used diagnostic has been increased to  $5 \mu s$  in order to reduce the signal noise). As a result, we cannot distinguish between a global and a local magnetic reconnection experimentally, which is the main conclusion from our GRILLIX simulation. Our current diagnostics would detect global heat redistribution (figure 4.1(a)) even when the magnetic reconnection is local (figure 4.1(b)).

### 4.3 Statistical analysis of sawtooth crashes

The previous section showed that the helically symmetric heat distribution along the torus is on a faster time scale than is accessible by the state-of-the-art diagnostics for tokamaks. For that reason, we concluded that we are unable to distinguish between local and global reconnection as long as the local reconnection leads to an outflow of heat to (initially) unperturbed field lines just outside  $q = 1$ . However, another group [Munsat et al., 2007] has reported experimental evidence of the helically (i.e. both toroidally and poloidally) localised sawtooth crash observation, contradicting our initial conclusion. The authors of Ref. [Munsat et al., 2007] state that there is no clear physical understanding of the local crash phenomenon. They refer to a hybrid ballooning mode and/or effect of a secondary instability as a possible cause. We interpret the reported local crash observation as a radial displacement of the hot core plasma region, which is observed by ECEI and inferred as local magnetic reconnection. The explanation would require an unknown helically localised magnetic confinement structure during the crash that we have not modelled with GRILLIX. This leads us to two cases of local magnetic reconnection. To clearly distinguish between these cases, we introduce an artistic representation of the magnetic reconnection in helical coordinates in figure 4.3, where three cases are shown:

1. Global magnetic reconnection without ballooning effect, shown in figure 4.3(a)
2. Local magnetic reconnection without ballooning effect (case observed in GRILLIX simulation in the previous section), shown in figure 4.3(b)
3. Local magnetic reconnection with ballooning effect, where some plasma fluxes are displaced to the area outside  $q = 1$  magnetic surface in a helically confined region (case possibly observed in the Ref. [Munsat et al., 2007]), shown in figure 4.3(c)

We assume the local displacement of plasma fluxes outside  $q = 1$  magnetic surface in a helically confined region (figure 4.3(c)) as given hypothesis. In this section, we will use

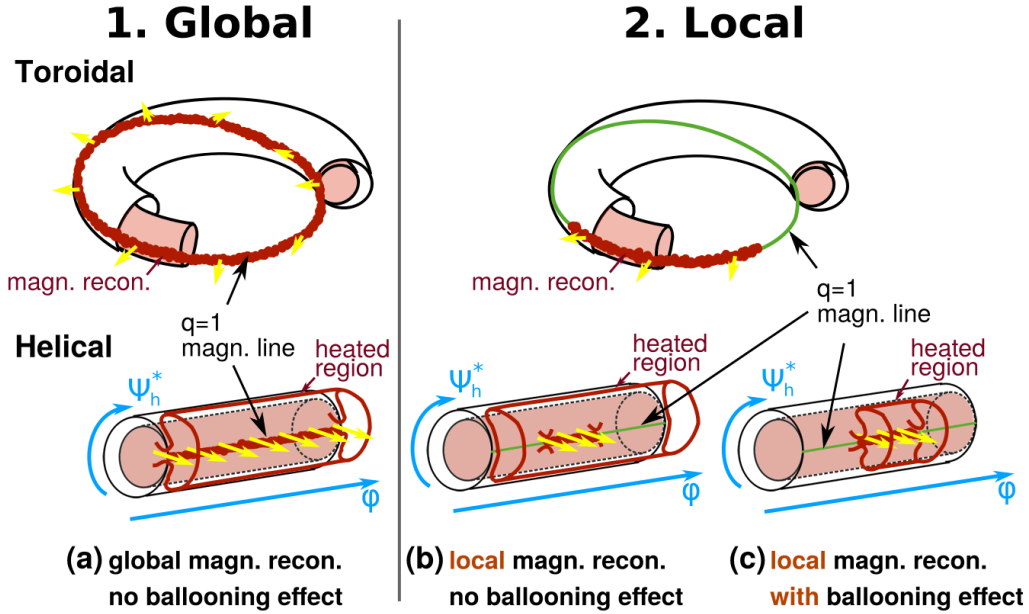


Figure 4.3: Artistic representation of the considered sawtooth crashes: global magnetic reconnection without ballooning effect, local magnetic reconnection without ballooning effect (b) and with ballooning effect (c) (some plasma fluxes are displaced to the area outside  $q=1$  magnetic surface prior to the local magnetic reconnection). The helical coordinates are used to clearly show the difference between the three cases.

the term "local sawtooth crash" with the reference to the hypothesis. The cases (a) and (b) in figure 4.3 are indistinguishable for our diagnostic and observed as "global" crash. To test this hypothesis, we checked whether we can experimentally observe the described local sawtooth crash in ASDEX Upgrade.

Ideally, one would need to compare the observations from several diagnostics at different tokamak toroidal angles (different poloidal cross-sections of the tokamak) to experimentally distinguish between global and local sawtooth crashes. On ASDEX Upgrade, there are four diagnostics that may be used to study core MHD activity: ECE, ECEI, SXR and Mirnov coils (for a description of these diagnostics and their usages to study MHD modes, please refer to [Igochine et al., 2015]; and for a more thorough overview of ECEI, refer to [Tobias et al., 2009, Classen et al., 2010]). It is not possible to determine the localisation of the crash with Mirnov coils. Although the SXR diagnostic has been shown to be good for studying the pre-crash phase of sawtooth instability [Vezinet et al., 2016] and has a toroidal separation by  $\sim 45^\circ$  from the ECE diagnostic (ECE and ECEI are located at the same poloidal plane), it does not have a sufficient number of lines of sight to resolve the crash phase. Thus, the SXR diagnostic cannot be combined with ECEI to distinguish local and global crashes.

Another approach to the problem is using statistical analysis. Namely, we can count how many times we see the crash in the ECEI window for a certain (1,1) mode rotation frequency. Thus, we can estimate the probability of a sawtooth crash observation in the

ECEI window for a certain (1,1) mode frequency. For different (1,1) mode frequencies, we can then plot the dependence of the observation probability on the frequency of the mode. This dependence will look different for local and global sawtooth crashes, as the observation probability of the global crash will be higher than the probability of the local one. The dynamics of sawtooth crash in ASDEX Upgrade can be studied thanks to the sufficient temporal ( $\Delta t_{ECEI} = 5 \mu s$ ) and spatial two-dimensional (12 by 40 cm, 8 by 16 channels) resolutions of the ECEI diagnostic. Examples of two sawtooth crashes measured in ASDEX Upgrade, one inside and one outside of the ECEI window, are shown in figure 4.4. A similar statistical approach has been applied by [Munsat et al., 2007] in TEXTOR tokamak, where the authors analysed 47 sawtooth crashes but all with the same rotation mode frequency. Under the assumption that the toroidal and poloidal centre of the localised reconnection zone occurs at a random location on the  $q = 1$  surface, the authors estimated the probability of the crash occurring within the ECEI observation window as:

$$P_{obs\ in\ ECEI} = \frac{\Delta\theta_{ECEI} + \Delta\theta_{rec} + \Delta\phi_{rec}}{2\pi} \quad (4.2)$$

where  $\Delta\theta_{ECEI}$  is the poloidal coverage of the ECEI window, and  $\Delta\theta_{rec}$  and  $\Delta\phi_{rec}$  are the poloidal and toroidal angular widths, respectively, of the reconnection zone. Taking the  $P_{obs\ in\ ECEI}$ ,  $\Delta\theta_{ECEI}$ ,  $\Delta\theta_{rec}$  from the experimental data ( $P_{obs\ in\ ECEI} \approx 50\%$ ,  $\Delta\theta_{ECEI} \approx 60^\circ$ ,  $4^\circ < \Delta\theta_{rec} < 14^\circ$ ), the authors estimated the toroidal angle of reconnection zone localisation to be  $\Delta\phi_{rec} \approx 108^\circ - 126^\circ$ .

In the ASDEX Upgrade tokamak we:

1. reproduced the observation of TEXTOR by measuring the same experimental parameters ( $P_{obs\ in\ ECEI}$ ,  $\Delta\theta_{ECEI}$ ,  $\Delta\theta_{rec}$ ).
2. expanded the study by analysing sawtooth crashes at different mode frequencies (in TEXTOR, the crashes were analysed only at a single frequency). Thus, we can determine the experimental dependency of the crash observation on the mode frequency  $P_{obs\ in\ ECEI}(\nu_{mode})$  and compare it with the theoretical prediction for local and global crashes.

To understand whether we can use eq. 4.2 to theoretically estimate  $P_{obs\ in\ ECEI}(\nu_{mode})$  in ASDEX Upgrade, we will first discuss its applicability. Eq. 4.2 is derived for sawtooth crashes that have a duration of at least one toroidal turn of the mode. In both tokamaks, ASDEX Upgrade and TEXTOR, it is challenging to experimentally determine the precise crash duration due to the influence of the (1,1) mode rotation on the measured signal, the non-linear character of the phenomenon, and the limited toroidal coverage of available plasma diagnostics. In the best scenario, one can determine the upper limit of the crash duration. The sawtooth crashes analysed in Ref [Munsat et al., 2007] had a (1,1) mode frequency of  $f_{mode} = 6.5\ kHz$ . As the author assumed that the crash evolves linearly on the timescale of one toroidal turn, the crash duration was assumed to be  $t_{crash} = \frac{1}{f_{mode}} \approx 150\ \mu s$ .

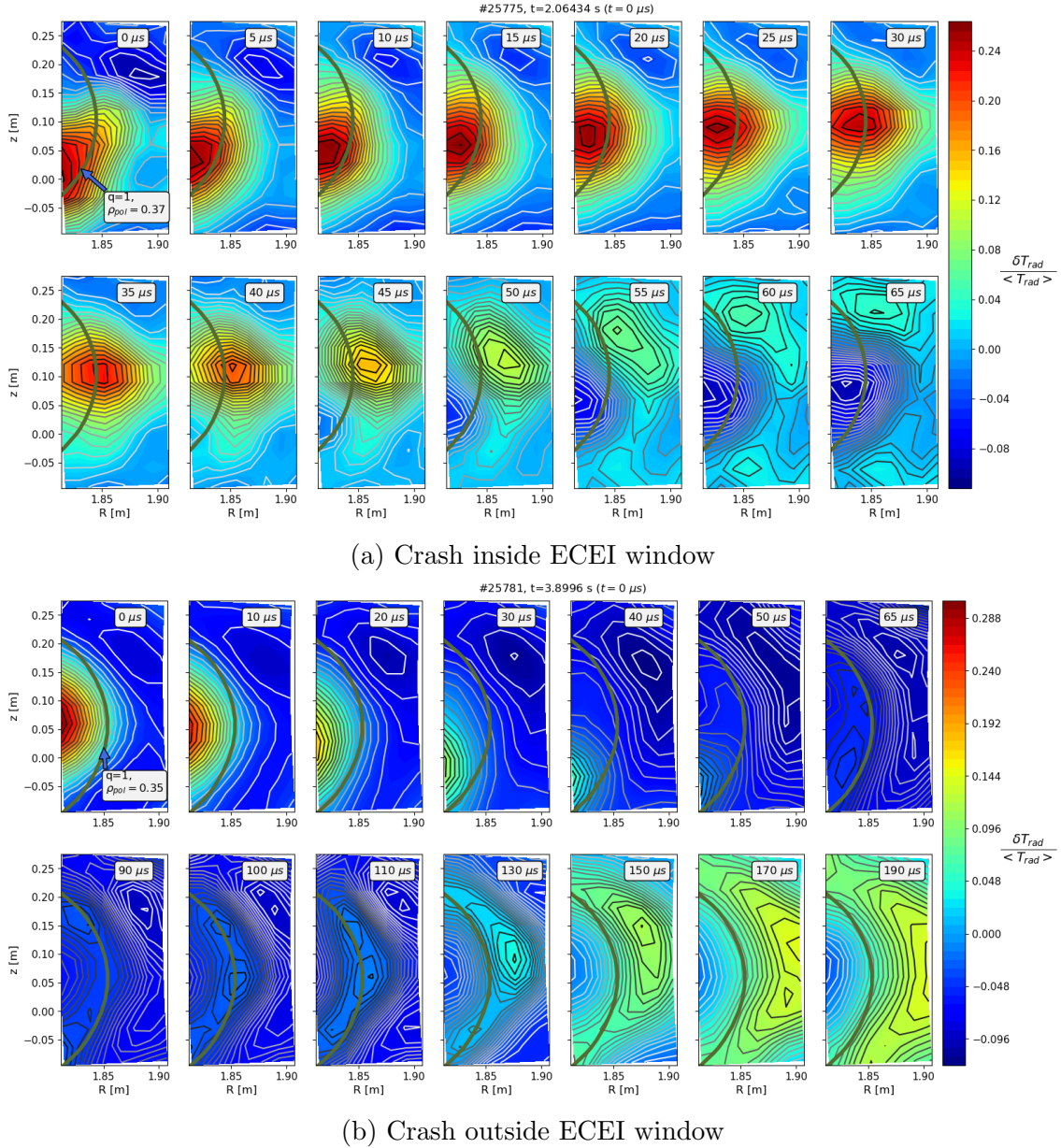


Figure 4.4: Examples of two sawtooth crashes measured with the ECEI diagnostic in ASDEX Upgrade: (a) inside and (b) outside of the ECEI window.  $\delta T_{rad} / \langle T_{rad} \rangle$  is normalized fluctuation of electron radiation temperature.  $R$  and  $z$  correspond to major radius and vertical axis of the tokamak respectively.

Our experimental database of sawtooth crashes in ASDEX Upgrade has  $(1,1)$  mode frequencies in a range of 0.5 to 11.5  $kHz$ . The frequency of the  $(1,1)$  mode and the velocity of toroidal plasma rotation are mainly determined by the NBI sources (the values for different shots are shown in Table C.2 of Appendix C). All crashes in the database have

a crash time duration of less than one toroidal turn of the plasma. We estimate the upper limit of the crash time from the shortest mode period that is available in the database:  $t_{crash}^{ASDEX} \leq \frac{1}{\max(f_{mode})} \approx 90 \mu s$ . Therefore, eq. 4.2 is not applicable for most of our data (it is marginally applicable only for the highest mode frequency).

To estimate  $P_{obs \text{ in ECEI}}(f_{mode})$  for the whole frequency range, we instead build a numerical model that simulates the observation of a sawtooth crash by ECEI. The position of the magnetic reconnection should be randomly set for each run of the model. Then, by running the model multiple times, one receives the statistical observation for a given (1, 1) mode frequency, poloidal/toroidal angles of the reconnection zone, and ECEI window size.

Our statistical model provides a two-dimensional description of a sawtooth crash (figure 4.5, B). It describes the magnetic reconnection of the crash as an opening in the  $q=1$  magnetic line (red region in figure 4.5) through which the hot plasma core expels to the outer magnetic surfaces ( $q > 1$ ). The opening size is described by the toroidal angle  $\Delta\chi_{rec}$  and poloidal angle  $\Delta\theta_{rec}$  (figure 4.5, B and C).  $\Delta\chi_{rec} = 120^\circ$  is taken from Ref [Munsat et al., 2007], which is the only experimentally reported toroidal angle value of the local sawtooth crash known to us.  $\Delta\theta_{rec}$  is evaluated from the 2D temperature profiles received from the ECEI. The angle corresponds to the size of the opening in the  $q = 1$  magnetic surface through which heat expels from the core to the outer magnetic surfaces ( $q > 1$ ). An example of this opening can be observed in figure 4.4a, time frames 25 – 40  $\mu s$ . The value  $\Delta\theta_{rec} \approx 15^\circ$  is obtained as the average from several sawtooth crashes. The blue horizontal line in figure 4.5 represents the ECEI window coverage. It covers the poloidal angle  $\Delta\theta_{ECEI} \approx 90^\circ$  (evaluated from the experimental data) of the  $q = 1$  magnetic surface. The (1, 1) mode rotates relative to the ECEI window with a constant frequency  $f_{mode}$ . The time duration of one simulation run corresponds to the upper limit of the sawtooth crash duration, that we estimated earlier ( $t_{crash}^{ASDEX} \approx 90 \mu s$ ). The time step of the model corresponds to the ECEI temporal resolution ( $dt_{ECEI} = 5 \mu s$ ). If during the simulation run the red crash zone crosses the ECEI coverage (blue horizontal line), then the crash is observed by the ECEI diagnostic. At the start of each model run, for the local crash we set randomly: a) the initial toroidal angle  $\phi_{q=1}$  that is between the lowest field side of the mode and the ECEI plane; and b) initial localization of the magnetic reconnection centre on the  $q = 1$  magnetic line. For the global crash, only the  $\phi_{q=1}$  parameter is used, since  $\Delta\chi_{rec} = 2\pi$ . For each given mode frequency  $f_{mode}$  we make  $N = 10^5$  simulation runs. We then count how many times we observe the crash in the ECEI window  $N_{obs}$ . Lastly, we receive the probability of observation from  $P_{obs \text{ in ECEI}}(f_{mode}) = \frac{N_{obs}}{N}$ . For a summary of input parameters of the model, please refer to appendix C.

Our experimental statistics include data from 167 sawtooth crashes from 6 plasma discharges. For a summary of plasma parameters, please refer to appendix C. The frequency of the (1,1) mode is obtained from SXR and Mirnov coils diagnostics. In all the analysed sawtooth crashes, there is a post-cursor (a mode that exists after the crash or "survives" the crash). Therefore, we have obtained data of the mode frequency from just before the crash ( $f_{mode}^B$ ) and directly after the crash ( $f_{mode}^E$ ). For the statistical analysis we took an average frequency value ( $\frac{f_{mode}^B + f_{mode}^E}{2}$ ). To note, for our data, the difference between  $f_{mode}^B$

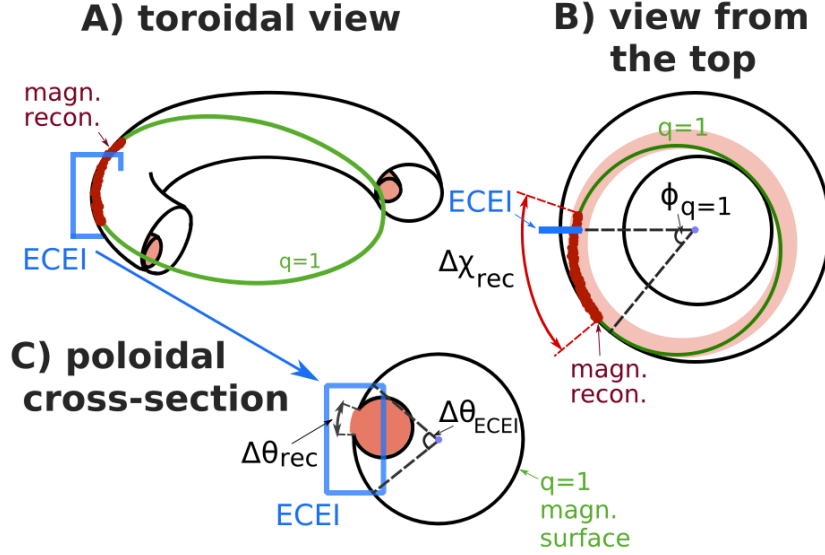


Figure 4.5: Artistic representation of the statistical model of sawtooth crash from toroidal 3D (A), top (B) and poloidal cross-section (C) views. The magnetic reconnection size is described with toroidal  $\Delta\chi_{rec}$  and poloidal  $\Delta\theta_{rec}$  angles.  $\phi_{q=1}$  is toroidal angle between the lowest field side of the mode and the ECEI plane at the beginning of the model run.  $\Delta\theta_{ECEI}$  is poloidal coverage of the  $q = 1$  magnetic surface.

and  $f_{mode}^E$  lays within 10% and the choice of the mode frequency for the analysis ( $f_{mode}^B$ ,  $f_{mode}^E$  or  $\frac{f_{mode}^B + f_{mode}^E}{2}$ ) did not significantly affect the final statistic or change the conclusions. Two digital filters were applied during the ECEI analysis for noise reduction: Savitzky-Golay [Schafer, 2011] and 2D Gaussian [SciPy-ndimage, 2021]. figure 4.4 displays the data after application of these two filters.

The comparison between the experimental and the numerically predicted  $P_{obs\ in\ ECEI}(f_{mode})$  is shown in figure 4.6. The error of the experimental data corresponds to the standard error of the Gaussian type statistic ( $standard\ error = \frac{standard\ deviation\ \sigma}{\sqrt{sample\ n\ observations}}$ ). As discussed earlier, eq. 4.2 is marginally applicable only for the highest (1,1) mode frequency of 11 kHz. The calculated statistic for this frequency is shown by the red column. The result from Ref. [Munsat et al., 2007] is shown by the black column, although it is beyond the applicability of eq. 4.2 since in ASDEX Upgrade the duration of the crash is faster than one toroidal turn of the mode. The red and black columns have the same probability, because eq. 4.2 does not consider the rotation frequency of the (1,1) mode. Local and global results from the numerical simulation are shown by the yellow and blue columns respectively. Overall, our experimental statistic fits the global model better over the whole frequency range, except for the 3.5 – 4.5 kHz. This discrepancy is likely due to an insufficient statistical number of observations for this frequency range. The used crash duration of 90  $\mu s$  is the upper limit in ASDEX Upgrade. With a lower value of the crash duration, the probability of the crash observation decreases for both local

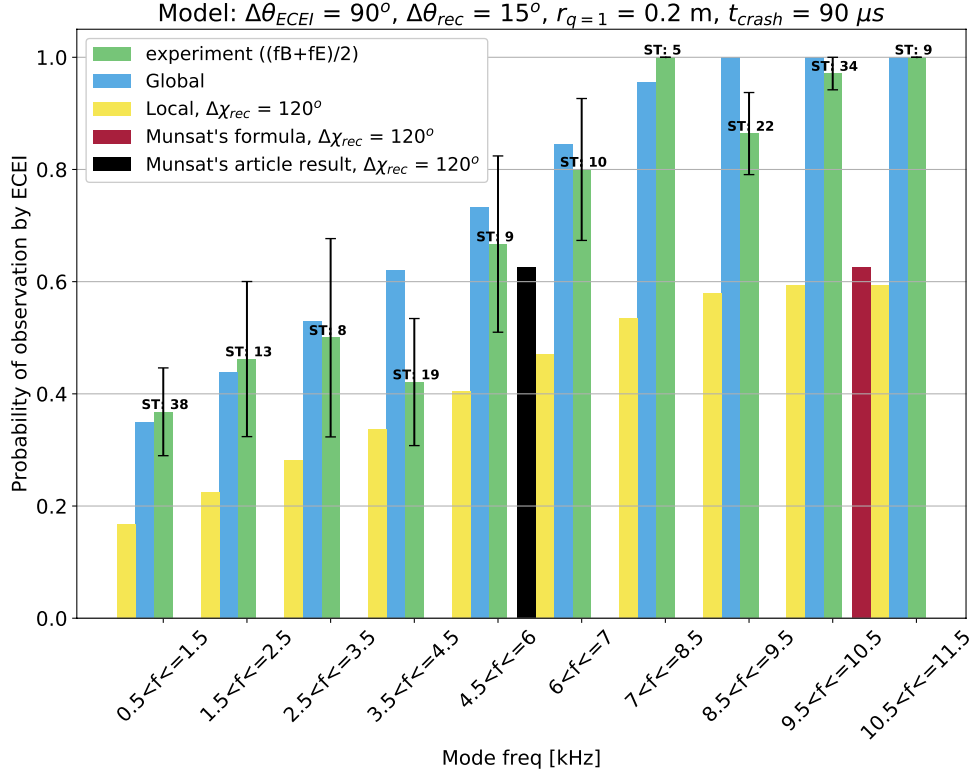


Figure 4.6: Probability of sawtooth crash observation in the ECEI window with the dependence on the (1,1) mode frequency  $P_{obs \text{ in ECEI}}(f_{mode})$ . In green are the experimental measurements in ASDEX Upgrade. The results from the global and local crash statistical model are shown in blue and yellow colours, respectively. The result calculated with eq. 4.2 is shown: a) in red for the frequencies where the equation is valid; b) in black for the frequency used in Ref. [Munsat et al., 2007].

and global crashes. Therefore, shorter crash duration enlarges the statistical distinction between experimental results and the local statistic (figure 4.6), and makes the global crash model resemble the experimental observation even more.

To summarise, local Sawtooth crash (localised displacement of plasma fluxes outside the  $q = 1$  magnetic surface (figure 4.3(c)) was not observed in ASDEX Upgrade. The observation of a local crash in TEXTOR [Munsat et al., 2007] has been done for a single frequency of the (1,1) mode (6.5 kHz). It is difficult to draw a conclusion between the local and global crashes from this single point as one can see in figure 4.6. The comparison across several frequencies leads to a more robust conclusion than with a single frequency. We observe only global (figure 4.3a) or local (figure 4.3b) magnetic reconnection scenarios, which, as we discussed in the previous section, are indistinguishable from each other for the current state of the art tokamak diagnostic due to insufficient temporal resolution. The numerical simulations show that with reduction of  $\Delta\chi_{rec}$  (figure 4.5B), the difference in probability of the crash observation by ECEI grows between global and local cases. An

increase of  $\Delta\chi_{rec}$  leads to a smaller difference between the global and local cases. The difference vanishes at  $\Delta\chi_{rec} = 360^\circ$ .

## 4.4 Summary

In this chapter, we studied the helical localisation of magnetic reconnection during sawtooth crashes in ASDEX Upgrade. Most research conducted on sawteeth to date either considered that a sawtooth crash has 2D nature (helically symmetric) or have not addressed the question of possible helical asymmetry. However, there are numerical [Park et al., 1995, Nishimura et al., 1999] and experimental [Nagayama et al., 1996, Munsat et al., 2007] works with a sawtooth crash helically localised in the toroidal plane.

First, we numerically studied the possibility of an experimental measurement for the helical localisation of the magnetic reconnection. We have modelled the heat propagation at the initial stage of sawtooth crash with the GRILLIX code [Stegmeir et al., 2018] using experimental plasma parameters. The result of this modelling showed that the heat redistributes helically along the torus on a much faster time scale ( $0.1 \mu s$ ) than is accessible by the state-of-the-art diagnostics of tokamaks (currently, the minimal accessible value is  $1 \mu s$ ; in this paper, the temporal resolution of  $5 \mu s$  is used in order to reduce the signal noise). Thus, one cannot distinguish between the global and local magnetic reconnection experimentally, because of the extremely fast redistribution of the heat along the magnetic field lines.

Second, we investigated experimental evidence of local magnetic reconnection reported in TEXTOR [Munsat et al., 2007]. The authors of Ref. [Munsat et al., 2007] conducted a statistical analysis of Sawtooth crashes with ECEI diagnostic. Their analysis assumes a toroidally localised heat distribution during the crash. We took the hypothesis as given and conducted a statistical analysis of crashes in ASDEX Upgrade with ECEI diagnostic for a broad range of (1,1) mode frequencies (0.5 - 11.5 kHz). Our analysis showed good agreement with the global sawtooth crash scenario and did not reveal evidence for the local heat redistribution. Observations in TEXTOR were conducted with a singular (1, 1) mode frequency (6.5 kHz) and the analysis was done with an assumption that crash has a time duration of one toroidal turn of the mode. Due to these two factors, it is hard to distinguish between local and global crashes (see figure 4.6, the data for the mode frequencies from 6 to 7 kHz) in the measurements conducted by [Munsat et al., 2007].

We conclude that even though one cannot exclude an event of local magnetic reconnection and the resulting fast redistribution of heat along the field lines, these events will be indistinguishable from global reconnection in all present-day ECE diagnostics.

# Chapter 5

## Velocimetry analysis of sawtooth crashes

(Chapter is adapted from the paper published in the NF [Samoylov et al., 2022b])

*I should find  
Some way incomparably light and deft,  
Some way we both should understand,  
Simple and faithless as a smile and  
shake of the hand.*

---

T. S. Eliot

In this chapter, we analyze the velocimetry of the plasma radiation temperature during sawtooth crashes in ASDEX Upgrade. Namely, the radial velocities and angular frequencies of the plasma core during the crash phase are obtained from the ECEI measurements. The radial velocities are compared with nonlinear two-fluid simulations.

### 5.1 Introduction

During a sawtooth crash, the radial motion of the plasma core corresponds to the growth of the  $(m, n) = (1, 1)$  magnetic island on the opposite side to the displaced plasma core, as shown by the Kadomtsev model [Kadomtsev, 1975] and the numerical simulations [Yu et al., 2015]. This island grows due to the magnetic reconnection as no other physical mechanisms can explain heat redistribution perpendicular to the magnetic equilibrium flux surfaces at such a fast time scale. Therefore, the radial velocity  $V_{rad}$  of the plasma core during the crash can be used as a characteristic rate of the magnetic reconnection. Furthermore, the experimentally obtained  $V_{rad}$  values can be directly compared with the values obtained from a numerical simulation of sawtooth crash, which, in this work, is done with the nonlinear two-fluid code TM1 [Yu et al., 2015]. This comparison validates

the sufficiency of the implemented physics in the code to model the magnetic reconnection during sawtooth crashes.

Even though, the ECEI measurements of the sawtooth crash has been conducted before in several tokamaks (in TEXTOR [Park et al., 2006, Munsat et al., 2007], HT-7 [Wan et al., 2009], ASDEX-Upgrade [Igochine et al., 2010a], DIII-D [Yu et al., 2012a], HL-2A [Jiang et al., 2015], EAST [Azam et al., 2015] and KSTAR [Nam et al., 2018]), to our knowledge, the described approach of obtaining the radial velocity and comparing it directly with the simulation is done for the first time. This novel and simple approach provides a good platform for studying the dynamics of magnetic reconnection dynamics and for numerical codes validations.

## 5.2 Description of the measurement and the simulation

The dynamics of sawtooth crashes in ASDEX Upgrade can be studied thanks to the sufficient temporal ( $\Delta t_{ECEI} = 5 \mu s$ ) and spatial two-dimensional (radial/vertical field 12 by 40 cm, respectively, resolved with 8 by 16 channels) resolution of the ECEI diagnostic. An example of a sawtooth crash measured by the ECEI is shown in figure 5.1a. The blue arrows indicate the plasma core movement during the crash phase. Namely, the point with the maximum electron temperature is traced.

In general, plasma dynamics in tokamaks has three-dimensional (3D) nature. However, the ECEI measurements are limited to a two-dimensional (2D) "slice" of the plasma radiation and possible 3D effects on the measurement and interpretation should be discussed. During a sawtooth crash, the non-ideal internal kink (or interchange) mode is always more unstable than the ideal one. Thus, we think that the mentioned 3D effects may occur due to the magnetic reconnection along the helical field. Even though these 3D effects may affect the measurements and interpretation of the plasma core rotation (and angular frequency), they do not play a role in the measurements of the radial movement as this movement is perpendicular to the magnetic surface and can be separated from the poloidal and toroidal rotation. Additionally, this independence of the radial velocity permits the comparison among crashes with different angular frequencies.

A schematic explanation of the radial velocity  $V_{rad}$  calculation is shown in figure 5.2 for two time frames. In each time frame, the position of the plasma core is detected:  $(R_1, Z_1)$  and  $(R_2, Z_2)$ . The corresponding normalized poloidal flux  $\rho$  and poloidal angle  $\theta^*$  are received from the magnetic equilibrium:  $(R_i, Z_i) \rightarrow \rho_i, \theta_i^*$ . In this way, Cartesian coordinates are mapped to flux coordinates. In the latter coordinate system, the radial velocity is calculated as

$$V_{rad} = \frac{(R_{Sep} - R_{Ax})(\rho_2 - \rho_1)}{\Delta t} \quad (5.1)$$

where  $R_{Sep}$  and  $R_{Ax}$  are radial coordinates of the separatrix (taken at the outer midplane at  $z = z_{axis}$ ) and the central axis, respectively;  $\Delta t$  is the time between the two considered

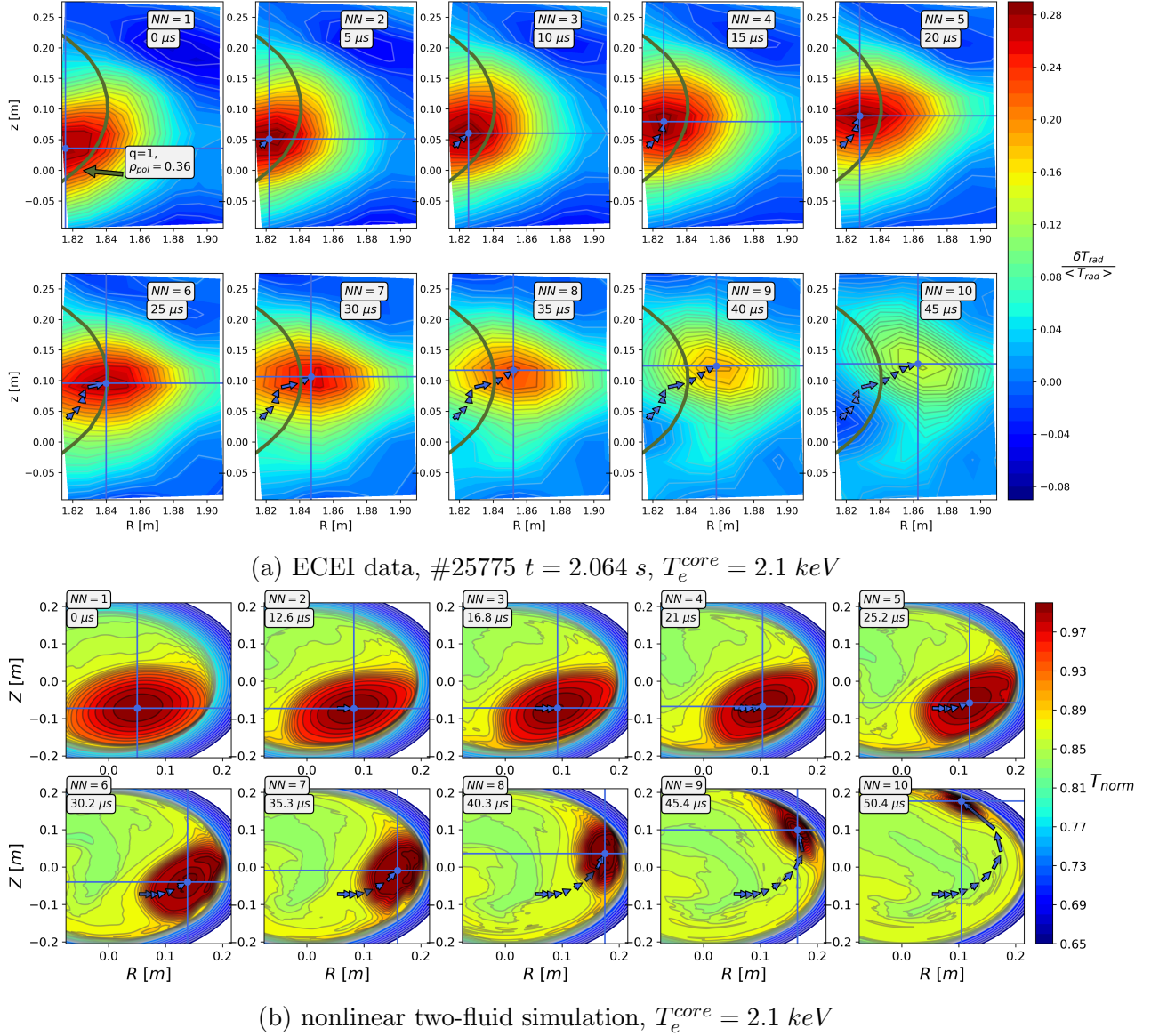


Figure 5.1: Tracing of plasma core movement during sawtooth crashes is shown for: (a) crash in ASDEX Upgrade measured with ECEI diagnostic and (b) nonlinear two-fluid simulation. Normalized fluctuation of electron radiation temperature  $\delta T_{rad}/\langle T_{rad} \rangle$  is used in the ECEI plot. Normalized absolute electron temperature is used in the nonlinear simulation.  $R$  and  $Z$  correspond to the major radius and the vertical axis of the tokamak, respectively. The blue arrows trace the movement of the plasma core. Two digital filters were applied to the ECEI data for noise reduction: Savitzky-Golay [Schafer, 2011] and 2D Gaussian [SciPy-ndimage, 2021].

time frames. The angular frequency  $\omega$  of the plasma core during the crash is calculated as:

$$\omega = \frac{\theta_2^* - \theta_1^*}{\Delta t} \quad (5.2)$$

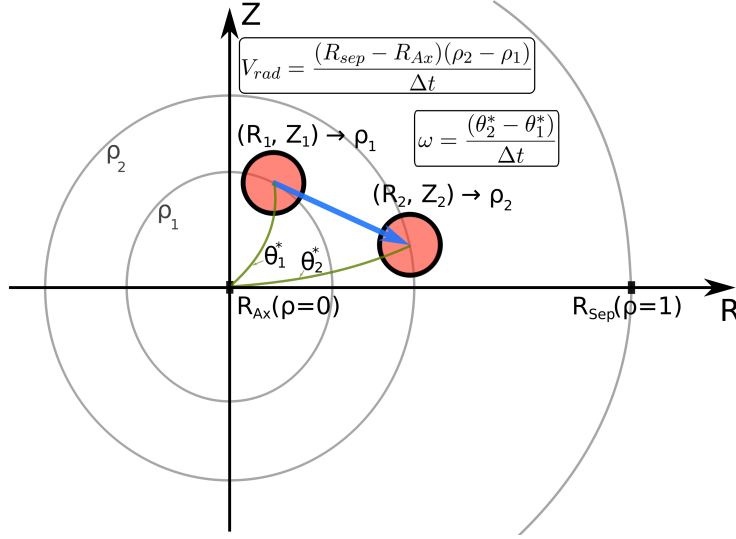


Figure 5.2: Schematic representation of radial velocity  $V_{rad}$  and angular frequency  $\omega$  calculations during a sawtooth crash is shown for two time frames. The red circle represents the point of the maximum electron temperature of the plasma. Cartesian coordinates  $(R_i, Z_i)$  of the red circle) are mapped to the flux coordinates: normalized poloidal flux  $\rho_i$  and poloidal angle  $\theta_i^*$ , where  $i$  is a time frame index.  $R_{sep}$  and  $R_{Ax}$  are radial coordinates of the separatrix and the central axis for the unperturbed equilibrium, respectively.  $\Delta t$  is the time duration between the two considered time frames.

We note that  $V_{rad}$  and  $\omega$  can be alternatively obtained using a Cartesian coordinate system with the coordinate centre on the magnetic axis. Flux and Cartesian coordinates are identical for the nonlinear two-fluid simulation since the code uses cylindrical tokamak geometry with circular cross-sections. The flux coordinates (straight field line mapping on a cylinder) have been chosen in this paper since it allows direct comparison between the experimental data and the simulation.

This study consists of 6 well-diagnosed crashes from 3 discharges. It is a far more frequent observation that the crash is observed in the ECEI window only partially (for example, a crash begins inside the window, but ends outside). Apart from that, only "fast" crashes (crash time duration is less than one toroidal turn of the plasma) are considered. They allow better study of magnetic reconnection dynamics than "slow" crashes (crash duration is more than one toroidal turn of the plasma). From the analyzed 200 "fast" crashes, only 6 ended in the view of the ECEI diagnostic and are suitable for the velocimetry analysis. The plasma parameters of the analyzed crashes are given in appendix D.

The nonlinear MHD code TM1 [Yu et al., 2015] is capable of simulating the sawtooth crash phase with realistic plasma parameters: Lundquist number  $S$  in the order of  $10^8$  (based on the total magnetic field); the ratio between the parallel and perpendicular heat conductivities  $\chi_{\parallel}/\chi_{\perp} = 10^9$ ; plasma resistivity, electron pressure gradient and electron inertia terms are included in the generalized Ohm's law. The code is shown to successfully simulate the sawtooth crash time [Günter et al., 2015]. The input parameters correspond

to the experimental parameters range of the considered six sawtooth crashes. Toroidal magnetic field is  $B_t = 2.5 T$ . Minor radius is  $a = 0.5 m$ , major radius is  $R = 1.75 m$ . Values for plasma electron densities  $n_e$  and temperatures  $T_e$  are taken from the experimental data. The plasma density is assumed constant along the radius, which also corresponds to the experimental situation. The radial profile of the equilibrium safety factor  $q$  is monotonic with the  $q = 1$  surface located at  $r = 0.31a$ . Three simulations have been conducted to cover the experimental parameter range: 1)  $T_e^{core} = 2.1 keV$ ,  $n_e = 8.6 \cdot 10^{19} m^{-3}$  (the parameters correspond to sawtooth crashes from shots #25775 at times 2.064 and 2.480 seconds); 2)  $T_e^{core} = 3.0 keV$ ,  $n_e = 8.8 \cdot 10^{19} m^{-3}$  (the parameters correspond to the sawtooth crash from shot #25782 at time 2.320 seconds); 3)  $T_e^{core} = 4.5 keV$ ,  $n_e = 8.8 \cdot 10^{19} m^{-3}$  (the parameters correspond to the sawtooth crash from shot #25782 at time 3.143 seconds). In magnetic reconnection research, the Lindquist number is commonly based on the reconnecting magnetic field [Ji and Daughton, 2011]:  $S^* = \tau_R / \tau_A^*$ , where  $\tau_R$  is the resistive time;  $\tau_A^*$  is the Alfvén time of the reconnecting magnetic field ( $\tau_R$  and  $\tau_A^*$  are defined in appendix B). In our study,  $S^* = 2.95 \cdot 10^5$ ,  $4.97 \cdot 10^5$  and  $9.2 \cdot 10^5$  for the three cases with  $T_e^{core} = 2.1, 3$  and  $4.5$ , respectively. There is no initial plasma rotation in the simulations. The rotation is generated during the crash phase by the Lorentz force due to the magnetic field and plasma current density perturbations [Yu et al., 2015].

The simulation result and its plasma core velocimetry tracing are shown in figure 5.1b. We note that the relative electron temperature is used for the experimental data (figure 5.1a), whereas the absolute normalized temperature is used for the nonlinear simulation. The velocimetry comparison between the relative and the absolute temperatures is valid since in both cases we trace the point of the maximum temperature amplitude. This temperature point is distinct and has the same location in both absolute and relative temperature plots.

## 5.3 Comparison of the experimental data with the simulation

### 5.3.1 Displacement

The full sawtooth cycle typically consists of precursor, crash and postcursor phases [Igochine et al., 2010a]. The precursor displacements, which result from a  $(m/n) = (1/1)$  MHD instability, have been thoroughly studied by [Vezinet et al., 2016] in ASDEX Upgrade. Postcursor is an MHD mode that observed after the crash (i.e. a mode that "survives" the crash). The postcursor and its displacement are beyond the scope of this chapter. The sawtooth crash phase is the sole focus of our study.

A schematic trajectory of the plasma core during a sawtooth period is shown in 5.3a. This trajectory consists of precursor (marked blue) and crash (marked red) parts. The ECEI observation field is shown as a green rectangle. The size of the ECEI window can cover only part of the  $q = 1$  surface as one can observe from the measurements in figure 5.1a. This limitation does not allow us to observe the full crash dynamics. Since only

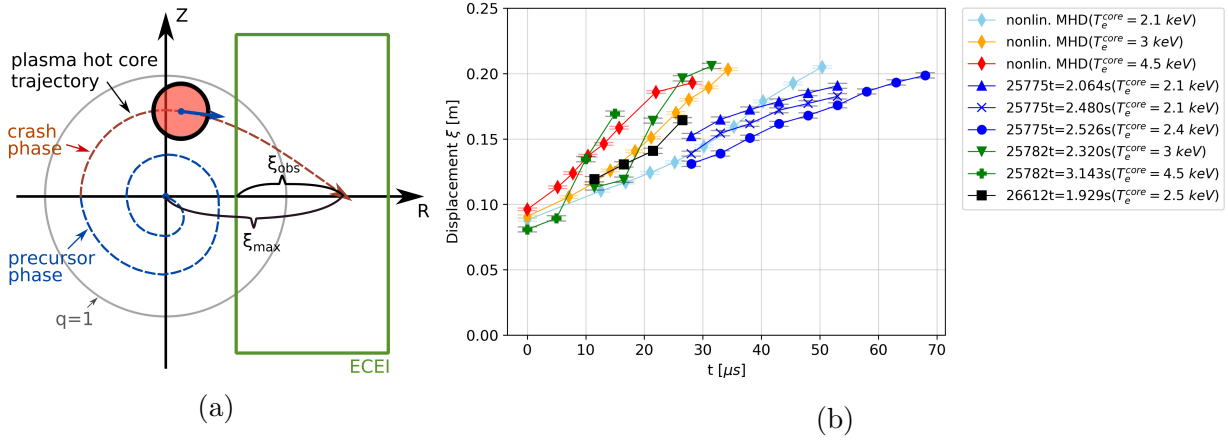


Figure 5.3: An artistic representation of the plasma core trajectory during a sawtooth crash is shown in (a). The red circle represents the point of the maximum electron temperature of the plasma. The dashed line shows the trajectory of the red circle during the precursor (marked in blue) and crash (marked in red) phases. The green rectangle represents a coverage area of the ECEI diagnostic window. The cartoon shows that only a part of the complete sawtooth crash is observed in the ECEI window due to its limited coverage area.  $\xi_{obs}$  is the radial displacement of the red circle observed inside the ECEI window.  $\xi_{max}$  is the maximal radial displacement of the red circle counting from the magnetic axis. The experimental displacements of the plasma core, which are measured for six crashes in ASDEX Upgrade, are shown in plot (b). These experimental displacements are used as the criterion for the correct comparison between the experimental results and the three two-fluid simulations of a complete sawtooth crash. The displacement of the first taken simulation time point corresponds to the minimum displacement detected in the experiment ( $\approx 8$  cm). The experimental points are shifted in time for the comparison with the simulation points of similar core plasma temperature  $T_e^{core}$ .

part of the sawtooth crash phase is observed, thus only part of the numerical simulation should be used. The plasma core displacement, which is shown in figure 5.3b, is used as the criterion for the correct comparison between the experimental data and the simulation. The simulation of the crash begins when the displacement equals zero. For the appropriate comparison with the experiment, we did not use the simulation data where the simulation displacement is smaller than the experimental displacement. As one can see in figure 5.3b, the displacement of the first taken simulation time point corresponds to the minimum displacement detected in the experiment ( $\approx 8$  cm). This first taken simulation point is assigned as  $0 \mu$ s time point (figure 5.1b: time frame NN = 1) for convenient comparison with the experiment data. The experimental points in figure 5.3b are shifted in order to compare them with the simulation points of similar core plasma temperature  $T_e^{core}$  (the temperature values are given in the legend).

## 5.3.2 Angular frequency

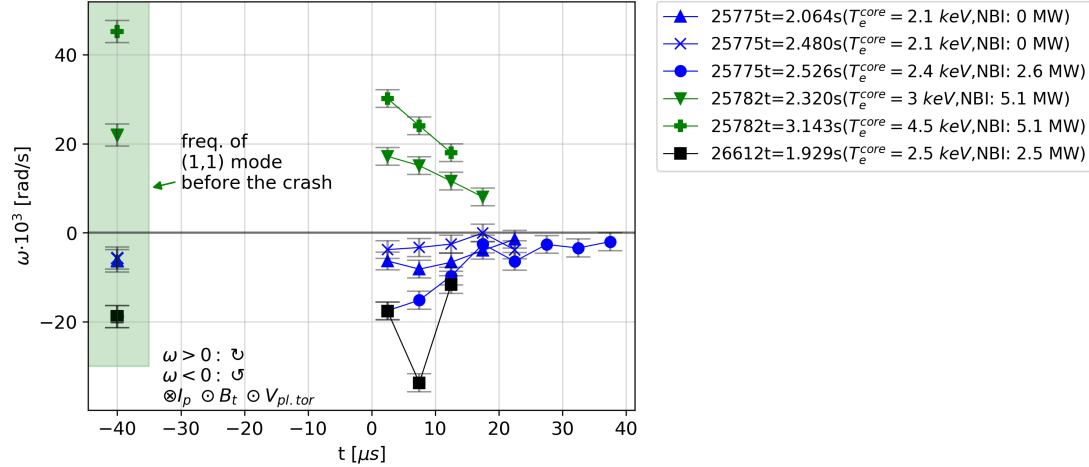


Figure 5.4: The figure shows the temporal evolution of the angular frequency  $\omega$  during sawtooth crashes obtained from the experimental data. The (1, 1) mode angular frequencies just before the crash are shown at the  $-40\mu\text{s}$  time point, which is an arbitrarily chosen time point for an indication that this frequency corresponds to the time before the crash. The power of the neutral beam injection (NBI) for each crash is given in the legend. For both the experiment and the simulation, plasma current  $I_p$  is directed into the paper, toroidal magnetic field  $B_t$  and the toroidal plasma rotation  $V_{pl.tor}$  directed out of the paper in the poloidal plane. Positive angular frequency  $\omega > 0$  is in a clockwise direction in the poloidal plane, and negative  $\omega < 0$  is in the counter-clockwise direction.

Generally, the plasma rotation during the crash phase can be described with four terms:

- Intrinsic rotation, which is usually defined as a nonzero toroidal plasma velocity in the absence of any auxiliary injected torque (note that intrinsic rotation has manifested itself both as rotation in the absence of any auxiliary input and as a finite offset in the plot of rotation velocity versus torque [DeGrassie et al., 2007]). Physically, it is a phenomenon of plasma self-organization, by which the properties of plasma microturbulence produce a macroscopically measurable effect. Intrinsic rotation may evolve during the crash phase due to changes in the plasma temperature profile. To date, the nature of intrinsic rotation is not completely understood.
- Torque from neutral beam injection (NBI).
- Torque from the neoclassical toroidal viscosity (damping of plasma flow due to spatial nonuniformity of magnetic field) [Shaing et al., 2010].
- Torque generated by the Lorentz force during the plasma current rearrangement in the core [Yu et al., 2015].

From these four terms, only the last term is implemented in the TM1 code. Based on the lack of necessary physical effects in the code, we conclude that the comparison of the nonlinear MHD simulation to the experiment is not justifiable. Thus, we present only the experimental results.

The temporal evolution of the angular frequency  $\omega$  during sawtooth crashes is shown in Fig. 5.4 for the experimental data. The (1, 1) mode angular frequencies just before the crash are shown at the  $-40\mu s$  time point, which is an arbitrarily chosen time point for an indication that this frequency corresponds to the time before the crash. Two crashes from #25782 discharge (marked in green) have sufficient NBI power and their rotation is mainly determined by NBI and is expected to be constant during the crash. These two crashes exhibit deceleration of the (1, 1) mode in the negative (counter-current) direction during the crash phase. This deceleration may be explained by the torque induced by the Lorentz force. On the other hand, the three crashes from #25775 (marked blue) discharge experience deceleration of the (1, 1) mode in the positive (co-current) direction during the crash phase. Lastly, the remaining crash from #26612 discharge (marked in black) has a non-stationary, "jumpy" behaviour of the angular frequency. The torque evolution in the mentioned crashes from #25775 and #26612 discharges likely originates from a complex interplay of several physical effects, which is beyond the scope of the current study.

### 5.3.3 Radial velocity

The comparison of the analyzed radial velocities and their average values during the sawtooth crashes is shown in figure 5.5. The average radial velocity lays in the range  $1.5 - 6 km/s$  in the experimental data, and in the range  $2.3 - 3.8 km/s$  in the numerical simulation. From this comparison, we conclude that the simulation gives realistic values of the outward movement. Both, the simulation and the experiment, show non-monotonous rises and falls of the radial velocity during the crash. Moreover, one can observe a distinct jump in the amplitude of the velocity for the shots #25782 and #26612. This shows that the reconnection process can have different phases and is not necessarily identical in similar conditions.

The observed sawtooth crash phenomenon is a driven magnetic reconnection in a semi-collisional plasma. In order to correctly describe this process, nonlinear two-fluid simulation should be used along with the inclusion of electron pressure gradient and electron inertia terms in generalized Ohm's law [Bhattacharjee et al., 2005]. These two terms are no longer negligible in comparison with the resistive term in semi-collisional plasma. The structure of current layers, which is associated with electron pressure gradient and electron inertia, allows to significantly speed up semi-collisional and collisionless magnetic reconnection [Wesson, 1990, Porcelli, 1991, Kleva et al., 1995] in comparison to magnetic reconnection in a collisional plasma.

The characteristic parameter of the electron pressure gradient contribution is the ion sound Larmor radius  $\rho_s = \sqrt{\frac{k_B T_e}{m_i} \frac{1}{\omega_{ci}}}$ , where  $T_e$  is the electron temperature,  $m_i$  is the ion mass,  $\omega_{ci}$  is the ion Larmor frequency. It has been shown [Schmidt et al., 2009, Yu et al.,

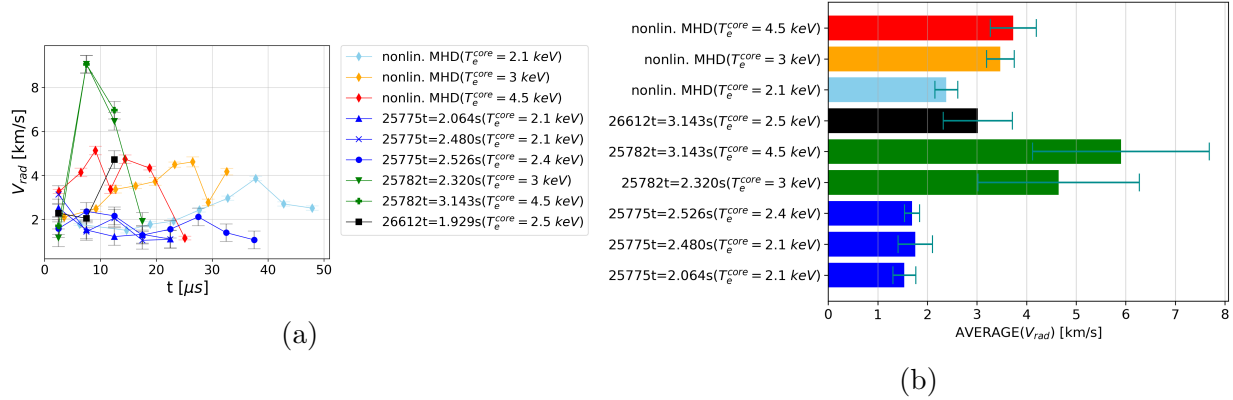


Figure 5.5: Radial velocities  $V_{rad}$  during the sawtooth crash phase for 6 crashes in ASDEX Upgrade and three two-fluid simulations are shown in (a). The corresponding average values of these velocities are shown in (b).

2012b, Granier et al., 2022] that the reconnection rate increases with higher  $\rho_s$  values, which is known as finite ion sound Larmor radius (FLR) effect. Since  $\rho_s \sim \sqrt{T_e}$ , we investigate a possible dependency of the average radial velocity  $AVG(V_{rad})$  (which characterizes the magnetic reconnection rate) on the core electron temperature  $T_e^{core}$ . The average radial velocity dependence on the core electron temperature is shown in figure 5.6a for the three simulation runs and for the experimental data. From this figure, one can conclude that the simulation matches with the experiment in terms of behavior ( $AVG(V_{rad})$  grows with the increase of  $T_e^{core}$ ) and quantity (the absolute values of  $AVG(V_{rad})$ ).

Another interesting value to investigate and compare with the nonlinear simulation is the duration of the sawtooth crash. Unfortunately, it is challenging to experimentally determine the precise full duration of a crash in ASDEX Upgrade due to the influence of the (1,1) mode rotation on the measured signal, the nonlinear character of the phenomenon, and the limited toroidal coverage of available plasma diagnostics. In other words, we cannot robustly determine the moment when the precursor phase ends and the crash phase begins. In this study, instead of the full crash time, we use the time during which the crash was partially observed in the ECEI diagnostic (see figure 5.1a and figure 5.3a) and denote it as  $\tau_{crash}^{part. obs.}$ . The beginning of the partial crash corresponds to the appearance of the center of the plasma core within the ECEI window (figure 5.1a, NN=1); and the end corresponds to the time of the maximum core displacement (figure 5.1a, NN=10). Consequently, only part of the crash time is used in the two-fluid simulations for comparison with the experiment. The criterion for the correct comparison is the plasma displacement as defined in section 5.3.1. The beginning of the simulation corresponds to the minimal experimental plasma displacement, the end corresponds to the maximal displacement of the plasma core in the simulation.

The experimentally observed crash times  $\tau_{crash}^{part. obs.}$  are compared with the three two-fluid simulation results in figure 5.6b, where  $\tau_{crash}^{part. obs.}$  is plotted against the core plasma temperature  $T_e^{core}$ . Additionally, the results have been compared to the crash time  $\tau_K =$

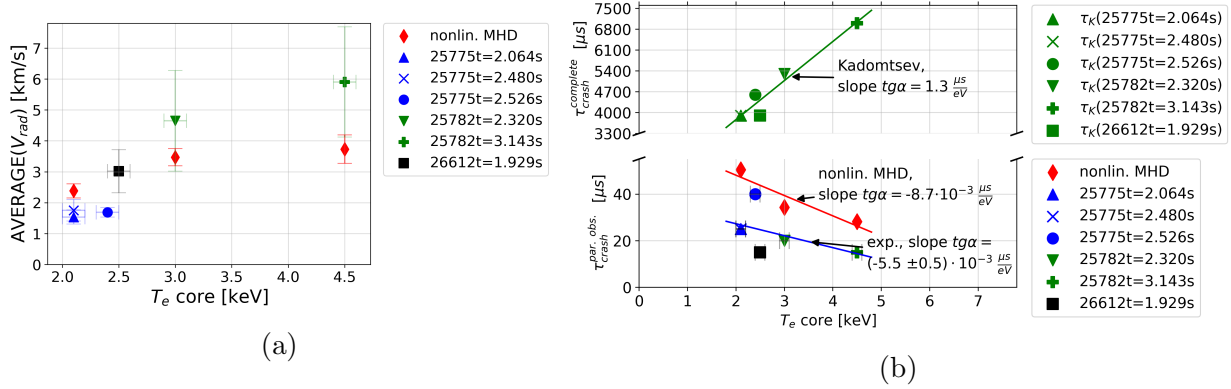


Figure 5.6: The dependence of the averaged radial velocity  $AVG(V_{rad})$  on the plasma core electron temperature  $T_e^{core}$  during sawtooth crashes is shown in (a). The dependence of the duration of partially observed sawtooth crashes  $\tau_{crash}^{part. obs.}$  on the plasma core electron temperature  $T_e^{core}$  is shown in (b). Both the experimental and the two-fluid simulation data are used in (a) and (b) plots. Kadomtsev times of complete crash  $\tau_K$  are calculated using the experimental parameters from the six crashes and are shown in (b). Straight lines represent a linear fit to the data. Slopes of the fitted lines of the Kadomtsev times are significantly different and the values are two orders of magnitude higher compared to the experimental results and the two-fluid simulations. To show all data, the upper part of the (b) plot has a different time scale than the lower part. Error bars of the averaged radial velocity measurements are statistical standard errors. Error bars of the core electron temperature are measurement errors.

$\sqrt{\tau_{RD}\tau_A^*} \sim T_e^{\frac{3}{4}}$  (where  $\tau_{RD}$  is resistive-diffusion time,  $\tau_A^*$  is Alfvén time for the reconnecting magnetic field; formulae are given in Appendix B) from the Kadomtsev model [Kadomtsev, 1975]. This model is the most known model of sawtooth crash. The Kadomtsev model describes the crash as a complete magnetic reconnection, where the regions with identical helical fluxes are connected to each other in a consequent manner. The Kadomtsev times of complete  $\tau_K$  crashes are calculated using the data (plasma densities, temperatures, displacements, poloidal magnetic fields, radii of  $q = 1$  magnetic surface) from the 6 experimental crashes and are shown in figure 5.6b. Linear dependency has been used to fit the data points of the Kadomtsev time, the experiment, and the two-fluid simulation. The experimental data has been linearly fitted six times, dropping a different data point for each fit and leaving five data points for the fit. The variation of six linear fits shows that the slope of the fitted line was varied in the range from  $-7.3 \cdot 10^{-3}$  to  $-3.5 \cdot 10^{-3} \frac{\mu s}{eV}$  with the mean value  $-5.5 \cdot 10^{-3} \frac{\mu s}{eV}$  and the standard error  $-0.5 \cdot 10^{-3} \frac{\mu s}{eV}$ . The latter means that the negative slope of the experimental data is a robust result. The simulation points match the experimental data qualitatively and quantitatively. The prediction based on the Kadomtsev model gives wrong dependencies and its crash time values differ by two orders of magnitude (see a jump in a time scale in the upper part of figure 5.6b) compared to the experiment. Thus, our study shows clearly that single-fluid Sweet-Parker

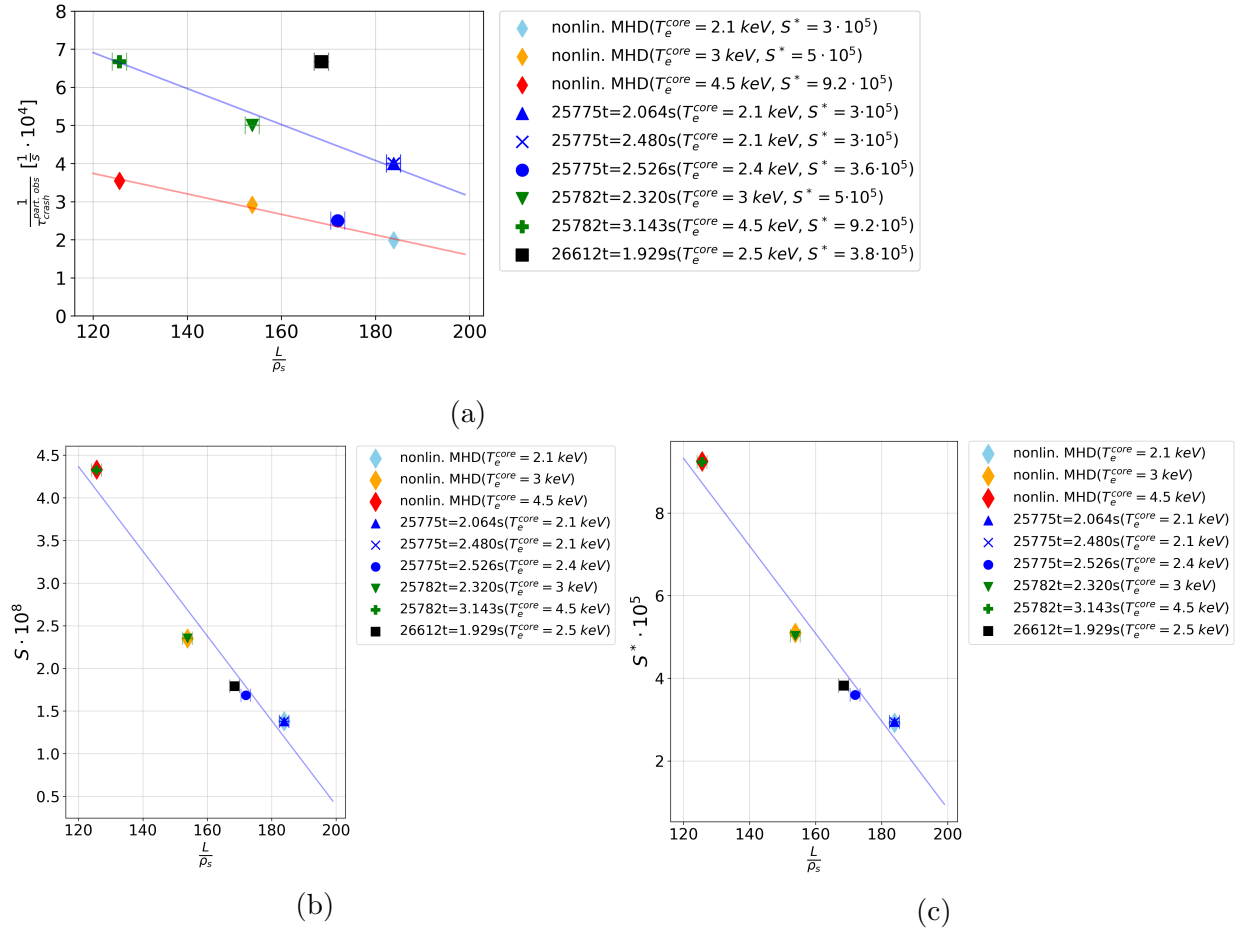


Figure 5.7: Reconnection rate  $\frac{1}{\tau_{crash}^{part. obs.}}$  of the partially observed crashes against the normalized system size  $\frac{L}{\rho_s}$  is displayed in (a). Two Lundquist numbers are plotted against the normalized system size  $\frac{L}{\rho_s}$ : (b) based on the toroidal magnetic field  $S = \frac{\tau_R}{\tau_A}$  and (c) on the reconnected magnetic field  $S^* = \frac{\tau_R}{\tau_A^*}$ . The data are shown for, both, the experiment and the two-fluid simulations.

type reconnection [Parker, 1957, Sweet, 1958] (which the Kadomtsev crash is based on) is not observed in the experiment. On the other hand, nonlinear simulations agree well with the experimental results. Thus, the physical model used in the simulation includes the necessary physics for a correct description of magnetic reconnection during a sawtooth crash.

Finally, in the magnetic reconnection research, two parameter spaces are usually investigated: first, the magnetic reconnection rate versus the characteristic system size  $L$  [Shay et al., 1999, Fitzpatrick, 2004, Olson et al., 2021]; and, second, the Lundquist number  $S$  versus the normalized system size  $\frac{L}{\rho_s}$  [Ji and Daughton, 2011, Huang and Bhattacharjee, 2013, Ji et al., 2022] (which is called the phase diagram and shown in figure 5.8).

To enable the comparison of the magnetic reconnection during the sawtooth crashes with the reconnection in other systems, we have plotted these both parameter spaces: the former is shown in figure 5.7a and the latter in figure 5.7b. The reconnection rate is defined as  $\frac{1}{\tau_{crash}^{part. obs.}}$ , the characteristic size of the system during the crash as  $L = \pi r_{q=1}$ . Two Lundquist numbers are plotted against the normalized system size  $\frac{L}{\rho_s}$ : based on the toroidal magnetic field  $S = \frac{\tau_R}{\tau_A}$  in figure 5.7b and on the reconnected magnetic field  $S^* = \frac{\tau_R}{\tau_A^*}$  in figure 5.7c ( $\tau_R$ ,  $\tau_A$  and  $\tau_A^*$  are defined in appendix A). While we think that  $S^*$  is more physically relevant, the  $S$  can be used for the comparison in figure 5.8. The figures 5.6b and 5.7a contain similar information, although the former figure is plotted for easier comparison among fusion research results and the latter for the magnetic reconnection research. The parameters of the phase diagram (figure 5.7b) are located in the "multiple X-line collisionless" regime according to [Ji and Daughton, 2011] (figure 5.8). In this regime, the reconnection is dominated by the two-fluid physics [Ji and Daughton, 2011].

## 5.4 Summary

Radial velocities  $V_{rad}$  and angular frequencies  $\omega$  of the plasma core during the sawtooth crash phase have been measured for the first time with ECEI diagnostic. In this study, only "fast" sawtooth crashes (crash time duration is less than one toroidal turn of the plasma) are considered.

A change in angular frequency during the crash phase is observed in all measured crashes. Deceleration of the (1, 1) mode during the crash phase is observed in both positive (co-current) and negative (counter-current) directions. An explanation of this angular frequency behaviour is beyond the scope of our study as it requires a physical model that includes the intrinsic, neoclassical viscosity, NBI and Lorentz force torques.

The radial velocities and their average values  $AVG(V_{rad})$  (representing the rate of magnetic reconnection) have been compared to the nonlinear two-fluid simulations. The comparison has shown good qualitative and quantitative agreement of the results. The variations of  $AVG(V_{rad})$  and observed crash durations are explained by the finite ion-sound Larmor effect (a contribution of the electron pressure gradient term in the generalized Ohm's law). Additionally, the observed crash durations have been compared to the time

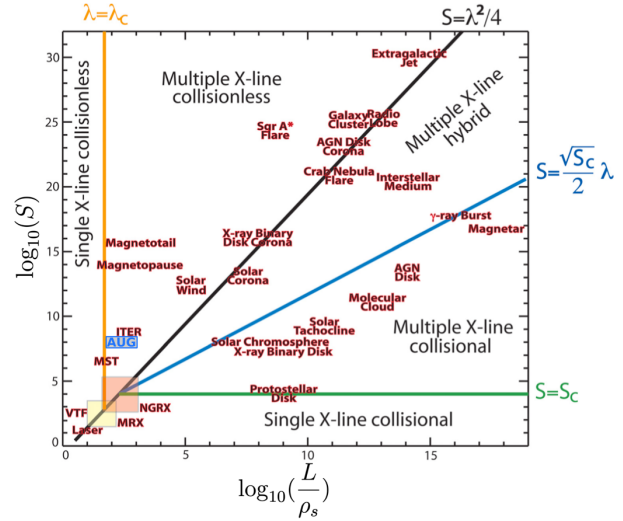


Figure 5.8: Phase diagram of magnetic reconnection [Ji and Daughton, 2011]. The Lundquist number  $S$  of the reconnected flux is plotted against the normalized system size  $\lambda = \frac{L}{\rho_s}$  in the logarithmic scales. Sawtooth crashes in ASDEX Upgrade (AUG) are located in the multiple X-line collisionless regime.

---

scaling of the Kadomtsev model (which is a Sweet-Parker type, single-fluid, magnetic reconnection in a collisional plasma). The predictions based on the Kadomtsev model gave wrong dependencies and two orders of magnitude difference for the crash time compared to the experiment. The latter is a confirmation that a two-fluid description, which contains electron pressure gradient and electron inertia effects, is required to correctly model magnetic reconnection during the sawtooth crash. Finally, to make our experimental and numerical results applicable within the magnetic reconnection research, the normalized system size is plotted as a parameter of the reconnection rates and the Lundquist numbers.



# Chapter 6

## Conclusions

*Do not spoil what you have by  
desiring what you have not.*

---

Epicurus

This thesis focuses on magnetic reconnection that occur during sawtooth instability. The theoretical understanding of this phenomenon is built upon a magnetohydrodynamic fundament (Chapter 2). The classical single-fluid Sweet-Parker reconnection, which is valid in collisional plasmas, is revisited within a two-fluid framework with the purpose to describe reconnection in plasma with low collisionality, where the Sweet-Parker reconnection rate is too slow to account for observations in space and laboratory plasmas. The effects from Hall, electron inertia and pressure gradient terms in generalized Ohm's law are examined in application to reconnection in semi-collisional and collisionless plasmas. These terms are able not only to significantly change the structure of magnetic field lines during reconnection but also to substantially speed up the reconnection rate making the rate similar to values observed in nature. When the external magnetic field that is much larger than the reconnected fields (= strong guide field reconnection) is applied perpendicular to the Sweet-Parker geometry, the inertia and pressure gradient of electrons are concluded to be the most important terms to correctly describe reconnection rate in semi-collisional and collisionless plasmas. Then, sawtooth instability cycle is reviewed with the focus on the crash phase, which is a strong guide field magnetic reconnection. After discussing the theoretical background, we have introduced our experimental setup: the ASDEX Upgrade tokamak and the diagnostics used in this thesis (Chapter 3). Having tools to diagnose and a theoretical image to perceive the measurements, we have studied the following two topics:

- **Helical localisation of magnetic reconnection during sawtooth crash** (Chapter 4)

Most research conducted on sawteeth to date either considered that a sawtooth crash has 2D nature (helically symmetric) or has not addressed the question of possible

helical asymmetry. However, there are numerical [Park et al., 1995, Nishimura et al., 1999] and experimental [Nagayama et al., 1996, Munsat et al., 2007] works with a sawtooth crash helically localised in the toroidal plane.

First, we have numerically studied the possibility of an experimental measurement for the helical localisation of the magnetic reconnection. We have modelled the heat propagation at the initial stage of a sawtooth crash with the GRILLIX code [Stegmeir et al., 2018] using experimental plasma parameters. The result of this modelling showed that the heat redistributes helically along the torus on a much faster time scale ( $0.1 \mu s$ ) that is accessible by the state-of-the-art diagnostics of tokamaks (currently, the minimal accessible value is  $1 \mu s$ ; in this paper, the temporal resolution of  $5 \mu s$  is used in order to reduce the signal noise). Thus, we have concluded that the global and local magnetic reconnection are experimentally indistinguishable, because of the extremely fast redistribution of the heat along the magnetic field lines.

Second, we have investigated experimental evidence of local magnetic reconnection reported in TEXTOR [Munsat et al., 2007], where the authors conducted a statistical analysis of Sawtooth crashes with ECEI diagnostic. Their analysis assumes a toroidally localised heat distribution during the crash. We took the hypothesis as given and conducted a statistical analysis of crashes in ASDEX Upgrade with ECEI diagnostic for a broad range of  $(1, 1)$  mode frequencies ( $0.5 - 11.5$  kHz). Our analysis showed good agreement with the global sawtooth crash scenario and did not reveal evidence for the local heat redistribution. Observations in TEXTOR were conducted with a singular  $(1, 1)$  mode frequency ( $6.5$  kHz) and the analysis was done with an assumption that crash has a time duration of one toroidal turn of the mode. Due to these two factors, we reason that the proposed distinction between local and global crashes for a singular  $(1, 1)$  mode frequency [Munsat et al., 2007] cannot be made with the ECEI diagnostic.

We conclude that even though one cannot exclude an event of local magnetic reconnection and the resulting fast redistribution of heat along the field lines, these events will be indistinguishable from global reconnection in all present-day ECE diagnostics.

- **Velocimetry analysis of sawtooth crashes** (Chapter 5)

Radial velocities  $V_{rad}$  of the plasma core during the sawtooth crash phase have been measured for the first time with ECEI diagnostic. These measurements introduce a novel approach for studying magnetic reconnection during sawteeth since the radial velocity characterises the rate of the reconnection. The radial velocities and their average values  $AVG(V_{rad})$  (representing the rate of magnetic reconnection) have been compared to nonlinear two-fluid simulations. The comparison has shown good qualitative and quantitative agreement of the results. The variations of  $AVG(V_{rad})$  and observed crash durations are explained by the finite ion-sound Larmor effect (a contribution of the electron pressure gradient term in the generalized Ohm's law).

Additionally, the observed crash durations have been compared to the time scaling of the Kadomtsev model (which is a Sweet-Parker type magnetic reconnection in

a collisional plasma). The predictions based on the Kadomtsev model gave wrong dependencies and two orders of magnitude difference for the crash time compared to the experiment. The latter is a confirmation that a two-fluid description, which contains electron pressure gradient and electron inertia effects, is required to correctly model magnetic reconnection during the sawtooth crash.

Finally, to make our experimental and numerical results applicable within the magnetic reconnection research, the normalized system size is plotted as a parameter of the reconnection rates and the Lundquist numbers.

# Appendix A

## Typical core plasma parameters in ASDEX Upgrade

### Given values

| Parameter  | Value                             |
|--|-----------------------------------|
| Major plasma radius ( $R_0$ )  | 1.65 m                            |
| Minor plasma radius ( $a$ )  | 0.5 m                             |
| Characteristic system size ( $L$ )                                       | 1.0 m                             |
| Toroidal field ( $B_{t0}$ )  | 2.5 T                             |
| Plasma current ( $I_p$ )   | 1.0 MA                            |
| Plasma gas   | D                                 |
| Ion mass $m_D$   | $3.34 \cdot 10^{-27}$ kg          |
| Effective charge number of ions $Z_{eff}$                                | 1.0                               |
| Plasma ion and electron temperature ( $T_e \approx T_i$ )                | 4 keV                             |
| Plasma density $n_e \approx n_i \approx n_D$                             | $8 \cdot 10^{19}$ m <sup>-3</sup> |
| Flux normalize radius of $q = 1$ ( $\rho_{q=1}$ )                        | 0.3                               |
| Radius of the $q = 1$ magn. surf. ( $r_{q=1}$ )                          | 0.15 m                            |
| The safety factor on the magnetic axis ( $q_0$ )                         | 0.9                               |
| Characteristic frequency of the (1, 1) mode ( $\nu_{(1,1) mode}$ )       | 6 kHz                             |
| Coloumb logarithm $\ln \Lambda$  | 17.5                              |
| Core perpendicular plasma coefficient $\chi_{\perp}$ [Luda et al., 2020] | $0.2 \frac{m^2}{s}$               |

Table A.1: Plasma parameters in the core of ASDEX Upgrade used for calculations

### Global characteristic plasma parameters

pressure Pa

$$p \approx p_i \approx p_e = n_e k_B T_e \approx 5 \cdot 10^4 \text{ Pa} = 0.5 \text{ bar} \quad (\text{A.1})$$

plasma beta ( $\beta$ )

$$\beta = \frac{p}{B_{t0}^2/(2\mu_0)} \approx 0.02 \quad (\text{A.2})$$

Poloidal magnetic field at  $q = 1$ :

$$B_\theta(r_{q=1}) \approx \frac{r_{q=1}B_\phi}{R_0} \approx 0.2 \text{ T} \quad (\text{A.3})$$

Helical magnetic field at  $q = 1$  [Wesson and Campbell, 2011, pg 354]:

$$B_\theta^*(r_{q=1}) \approx (1 - q_0)B_\theta(r_{q=1}) \approx 0.02 \text{ T} \quad (\text{A.4})$$

The classical Spitzer-Härm thermal diffusivity [Spitzer and Härm, 1953]:

$$\chi_{\parallel}^{SH} = 3.16v_{th,e}\lambda_e = 3.6 \cdot 10^{29} \frac{T_e[\text{keV}]^{5/2}}{n_e[\text{m}^{-3}]} \left[ \frac{\text{m}^2}{\text{s}} \right] \approx 1.4 \cdot 10^{11} \text{ m}^2/\text{s} \quad (\text{A.5})$$

The formula is known to give overestimated values. The corrected version by [Chang and Callen, 1992]:

$$\chi_{\parallel}^{CC} = \frac{\chi_{\parallel}^{SH}}{\sqrt{1 + \left(3.16 \frac{v_{th,e}}{\nu_{ei}L_c}\right)^2}} \left[ \frac{\text{m}^2}{\text{s}} \right] \approx 1.9 \cdot 10^7 \text{ m}^2/\text{s} \quad (\text{A.6})$$

where  $L_c$  is the connection length (taken as  $L_c = L = 1.0 \text{ m}$ ).

Classical Spitzer resistivity [Wesson and Campbell, 2011, pg 71,736]:

$$\eta_{Sp} = 1.65 \cdot 10^{-9} \frac{\ln \Lambda}{T_e^{3/2}[\text{keV}]} [\text{Ohm} \cdot \text{m}] = 3.6 \cdot 10^{-9} [\text{Ohm} \cdot \text{m}] \quad (\text{A.7})$$

Lundquist Number  $S$ :

$$S = \frac{\tau_{RD}}{\tau_A} \approx 1.5 \cdot 10^9 \quad (\text{A.8})$$

Lundquist Number  $S^*$  of the reconnected magnetic lines:

$$S^* = \frac{\tau_{RD}}{\tau_A^*} \approx 1.4 \cdot 10^7 \quad (\text{A.9})$$

### Characteristic frequencies

Electron and ion plasma (circular) frequencies (the true frequencies are expressed as  $\nu = \frac{\omega}{2\pi}$ ):

$$\omega_{pe} = \sqrt{\frac{n_e e^2}{\epsilon_0 m_e}} \approx 5 \cdot 10^{11} \text{ rad/s} ; \nu_{pe} \approx 80 \text{ GHz} \quad (\text{A.10})$$

$$\omega_{pi} = \omega_{pD} = \sqrt{\frac{n_D(Z \cdot e)^2}{\epsilon_0 m_D}} \approx 8.3 \cdot 10^9 \text{ rad/s} ; \nu_{pi} = 1.3 \text{ GHz} \quad (\text{A.11})$$

$$\omega_{ce} = \frac{eB_0}{m_e} \approx 4.4 \cdot 10^{11} \text{ rad/s} ; \nu_{ce} \approx 70 \text{ GHz} \quad (\text{A.12})$$

$$\omega_{ci} = \frac{eB_0}{m_D} \approx 1.2 \cdot 10^8 \text{ rad/s} ; \nu_{ci} \approx 19 \text{ MHz} \quad (\text{A.13})$$

$$\omega_{(1,1) \text{ mode}} = 2\pi\nu_{(1,1) \text{ mode}} \approx 3.8 \cdot 10^4 \text{ rad/s} ; \nu_{(1,1) \text{ mode}} = 6 \text{ kHz} \quad (\text{A.14})$$

Electron-ion collision frequency [Chen, 2016, pg 415]:

$$\nu_{ei} = 2 \cdot 10^{-6} \frac{Zn_e [cm^{-3}] \ln \Lambda}{T_e^{\frac{3}{2}} [eV]} [s^{-1}] = 1.1 \cdot 10^4 \text{ s}^{-1} \quad (\text{A.15})$$

### Characteristic velocities

Thermal velocity of electrons and ions:

$$v_{th,e} = \sqrt{\frac{k_B T_e}{m_e}} \approx 2.7 \cdot 10^7 \text{ m/s} \quad (\text{A.16})$$

$$v_{th,i} = v_{th,D} = \sqrt{\frac{k_B T_D}{m_D}} \approx 4.4 \cdot 10^5 \text{ m/s} \quad (\text{A.17})$$

Ion sound speed from [Chen, 2016, pg 91]:

$$C_{s,i} = \sqrt{\frac{\gamma_e k_B T_e + \gamma_i k_B T_i}{m_i}} \approx 8.8 \cdot 10^5 \text{ m/s} \quad (\text{A.18})$$

Ions suffer one-dimensional compressions in the plane waves (assumption) so the adiabatic index can be set to  $\gamma_i = 3$ . The electrons move fast compared to ion sound wave, so they have time to equalize their temperature everywhere (isothermal), thus  $\gamma_e = 1$ .

Alfven velocity:

$$v_A = \frac{B_0}{\sqrt{\mu_0 n_i m_i}} \approx 4.3 \cdot 10^6 \text{ m/s} \quad (\text{A.19})$$

Alfven velocity of the reconnected magnetic lines:

$$v_A^* = \frac{B_\theta^*}{\sqrt{\mu_0 n_i m_i}} \approx 3.9 \cdot 10^4 \text{ m/s} \quad (\text{A.20})$$

Characteristic velocity of the plasma fluid:

$$V_0 \approx \omega_{(1,1) \text{ mode}} R_0 \approx 6.2 \cdot 10^4 \text{ m/s} \quad (\text{A.21})$$

Mach number (the ratio of the fluid velocity  $V_0$  to the fluid sound velocity  $v_{th,fluid} \approx C_{s,i}$ ):

$$M = \frac{V_0}{C_{s,i}} \approx 0.07 \quad (\text{A.22})$$

### Characteristic lengths

Characteristic length of the system taken as:

$$L = 1.0 \text{ m} \quad (\text{A.23})$$

Debye Length:

$$\lambda_D = \sqrt{\frac{\epsilon_0 k_B T_e}{n_e e^2}} \approx 53 \text{ } \mu\text{m} \quad (\text{A.24})$$

Electron and ion skin depths:

$$\lambda_e = \frac{c}{\omega_{pe}} \approx 0.6 \text{ mm} \quad (\text{A.25})$$

$$\lambda_i = \frac{c}{\omega_{pi}} \approx 3.6 \text{ cm} \quad (\text{A.26})$$

Electron and ion gyroradii (Larmor radii):

$$\rho_e = \frac{m_e v_{\perp,e}}{e B_0} \approx \frac{\sqrt{m_e k_B T_e}}{e B_0} \approx 60 \text{ } \mu\text{m} \quad (\text{A.27})$$

$$\rho_i = \frac{m_i v_{\perp,i}}{e B_0} \approx \frac{\sqrt{m_i k_B T_i}}{e B_0} \approx 4 \text{ mm} \quad (\text{A.28})$$

Ion sound Larmor radius:

$$\rho_s = \sqrt{\frac{k_B T_e}{m_i}} \frac{1}{\omega_{ci}} \approx 4 \text{ mm} \quad (\text{A.29})$$

the mean-free path for electron-ion collisions [Chen, 2016, pg 415]:

$$\lambda_{mfp} = 3(2\pi)^{3/2} \frac{(k_B T_e \epsilon_0)^2}{n e^4 \ln \Lambda} \approx 1.6 \text{ km} \quad (\text{A.30})$$

Scale-length of the two-fluid effects in the generalized Ohm's law:

$$L_{inertia} = \lambda_e \approx 0.6 \text{ mm} \quad (\text{A.31})$$

$$L_{Hall, Sweet-Parker} = \frac{\lambda_i}{M} \approx 0.5 \text{ m} \quad (\text{A.32})$$

$$L_{Hall, strong guide field} = \frac{\rho_s}{M} \approx 5.7 \text{ cm} \quad (\text{A.33})$$

$$L_{pressure, Sweet-Parker} = \frac{\beta^{1/2} \lambda_i}{M} \approx 7 \text{ cm} \quad (\text{A.34})$$

$$L_{\text{pressure, strong guide field}} = \frac{\beta^{1/2} \rho_s}{M} \approx 7.4 \text{ mm} \quad (\text{A.35})$$

$$L_{\text{collisions}} = \beta^{1/2} \frac{\lambda_e \cdot \lambda_i}{\lambda_{mfp}} \frac{1}{M} \approx 3 \cdot 10^{-8} \text{ m} \quad (\text{A.36})$$

### Characteristic times

Alfven time:

$$\tau_A = \frac{L}{v_A} \approx 2 \cdot 10^{-7} \text{ s} \quad (\text{A.37})$$

$$\tau_A^* = \frac{L}{v_A^*} \approx 2 \cdot 10^{-5} \text{ s} \quad (\text{A.38})$$

Resistive time scale:

$$\tau_{RD} = \frac{\mu_0 L^2}{\eta_{Sp}} \approx 350 \text{ s} \quad (\text{A.39})$$

Alfven time of the reconnected magnetic lines:

Collision times [Stroth, 2011, pg 258]:

$$\tau_{ee} \approx 1.4 \cdot 10^{10} \frac{(T_e[\text{eV}])^{3/2}}{n_e[\text{m}^{-3}]} [\text{s}] \approx 4 \cdot 10^{-5} \text{ s} \quad (\text{A.40})$$

$$\tau_{ei} \approx 2.8 \cdot 10^{10} \frac{(T_e[\text{eV}])^{3/2}}{Z_i^2 n_e[\text{m}^{-3}]} [\text{s}] \approx 9 \cdot 10^{-5} \text{ s} \quad (\text{A.41})$$

$$\tau_{ii} \approx 6 \cdot 10^{11} \frac{A_i^{1/2} (T_e[\text{eV}])^{3/2}}{Z_i^4 n_e[\text{m}^{-3}]} [\text{s}] \approx 3 \cdot 10^{-3} \text{ s} \quad (\text{A.42})$$

Parallel diffusion times:

$$\tau_{\parallel}^{SH} = \frac{L^2}{\chi_{\parallel}^{SH}} \approx 7 \cdot 10^{-12} \text{ s} \quad (\text{A.43})$$

$$\tau_{\parallel}^{CC} = \frac{L^2}{\chi_{\parallel}^{CC}} \approx 5 \cdot 10^{-8} \text{ s} \quad (\text{A.44})$$

# Appendix B

## Transport coefficients in GRILLIX

In collisionless plasma, as in the core plasma of ASDEX Upgrade, parallel transport coefficient  $\chi_{\parallel}$  can be estimated with [Chang and Callen, 1992]:

$$\chi_{\parallel} = \frac{\chi_{SH}}{\sqrt{1 + \left(3.16 \frac{v_{th,e}}{\nu_{ei} L_c}\right)^2}} \left[ \frac{m^2}{s} \right] \quad (\text{B.1})$$

where  $\chi_{SH}$  is the classical Spitzer-Härm formula  $\chi_{SH}$  [Spitzer and Härm, 1953] for perpendicular transport coefficient in collisional plasma:

$$\chi_{SH} = 3.16 v_{th,e} \lambda_e = 3.6 \cdot 10^{29} \frac{T_e [keV]^{\frac{5}{2}}}{n_e [m^{-3}]} m^2 s^{-1} \quad (\text{B.2})$$

and  $\nu_{ei}$  is electron-ion collision frequency [Chen, 2016, p. 415]:

$$\nu_{ei} = 2 \cdot 10^{-6} \frac{Z n_e [cm^{-3}] \ln \Lambda}{T_e^{\frac{3}{2}} [eV]} [s^{-1}] \quad (\text{B.3})$$

In the equations above,  $v_{th,e}$  is the electron thermal velocity,  $\lambda_e$  is the mean free path of electrons,  $T_e$  and  $n_e$  are the electron temperature and density respectively,  $L_c$  is the heat connection length,  $Z$  is the ion charge state,  $\ln \Lambda$  is the Coulomb logarithm.

Plasma parameters of the considered in this paper sawtooth crashes are:  $Z = 2$  (deuterium plasma),  $T_e \approx 3 \text{ keV}$ ,  $n_e \approx 5 \cdot 10^{19} \text{ m}^{-3}$ ,  $\ln \Lambda = 17$ ,  $L_c = 2\pi R_0 = 10.4 \text{ m}$  ( $R_0$  is major radius of ASDEX Upgrade). The result of the calculation:  $v_{th,e} = 2.3 \cdot 10^7 \text{ m/s}$ ,  $\nu_{ei} = 10^4 \text{ s}^{-1}$ ,  $\chi_{SH} = 1.1 \cdot 10^{11} \text{ m}^2/\text{s}$ ,  $\chi_{\parallel} \approx 2 \cdot 10^8 \text{ m}^2/\text{s}$ .

Perpendicular heat transport coefficient is taken as a typical value for an ASDEX-Upgrade discharge in the core plasma  $\chi_{\perp} \approx 1 \text{ m}^2/\text{s}$  [Luda et al., 2020]. The ratio between parallel and perpendicular coefficients:  $\frac{\chi_{\parallel}}{\chi_{\perp}} = 2 \cdot 10^8$ . Such high anisotropies can be handled with GRILLIX thanks to the flux-coordinate independent approach in combination with the support operator method [Stegmeir et al., 2016]. Additionally, the results in section 3 were found to be converged in resolution.

# Appendix C

## Crash statistic: plasma parameters

Input parameters of the statistical model is summarised in table C.2 (see figure 4.5 as a schematic representation of the listed parameters).

Plasma parameters of the analysed discharges from section 4.3 is summarised in table C.2. The following notation is used:  $t$  and  $f_{mode}$  are the time and mode frequency ranges, respectively, of the analysed sawteeth in a specific shot;  $I_p$  is the plasma current;  $NBI$  is the neutral beam injection;  $ECRH$  and  $ICRH$  are the electron and ion cyclotron resonant heating, respectively;  $n_e$  is the average plasma density received from interferometry. The axial toroidal magnetic field for all considered shots was  $B_t = 2.5 T$ .

Table C.1: Input parameters of the statistical model

| Parameter             | Value  | Description   |
|-----------------------|--|---|
| $r_{q=1}$             | 0.2 m  | Radius of q=1 magn. surf  |
| $R_0$                 | 1.65 m   | ASDEX Upgrade major radius  |
| $t_{crash}$           | 90 $\mu s$   | Time duration of Sawtooth crash (duration of simulation)  |
| $dt_{ECEI}$           | 5 $\mu s$  | ECEI temporal resolution (simulation time step)   |
| $\Delta\theta_{ECEI}$ | 90°  | Poloidal coverage of $q = 1$ magn. surf by ECEI window  |
| $f_{mode}$            | 0.5 – 11.5 kHz, step 0.5 kHz   | Frequency range of the (1,1) mode   |
| $N$                   | 10 <sup>5</sup>  | Number of simulation runs on a singular (1, 1) mode frequency $f_{mode}$  |
| $\Delta\theta_{rec}$  | 15°  | Poloidal angle of magnetic reconnection (taken from experimental data)  |
| $\Delta\chi_{rec}$    | 120° for local crash<br>360° for global crash  | Toroidal angle of magnetic reconnection (taken from Ref. [Munsat] for local crash)  |
| $\phi_{q=1}$          | 0 – 360°, set randomly at each model run   | Initial toroidal angle between ECEI window and the lowest field side of $q = 1$ magnetic line on which the magnetic reconnection occurs |
| $\chi_0$              | 0 – 360°, set randomly at each model run for local crash (not relevant for global crash) | The initial localisation of magnetic reconnection centreon $q = 1$ magnetic line  |

Table C.2: Plasma parameters of the analysed discharges

| <i>Shot</i> | <i>t</i> [s] | <i>f<sub>mode</sub></i> [kHz] | <i>N<sub>ST</sub></i> | <i>I<sub>p</sub></i> [MA] | <i>NBI</i> [MW] | <i>ECRH</i> [MW] | <i>ICRH</i> [MW] | <i>n<sub>e</sub></i> [10 <sup>19</sup> m <sup>-3</sup> ] |
|-------------|--------------|-------------------------------|-----------------------|---------------------------|-----------------|------------------|------------------|--|
| 25775       | 1.8-2.8      | 1.0-6.0                       | 24                    | 1                         | 0-2.6           | 0                | 4.5              | 8.6  |
| 25781       | 2.1-5        | 0.5-10.0                      | 54                    | 1                         | 2.6-5.2         | 0.8-1.7          | 4.5              | 8.8  |
| 25782       | 2.26-3.35    | 1.0-11.0                      | 14                    | 1                         | 5.1             | 1.7              | 4.3              | 8.8  |
| 25783       | 2.07-2.46    | 1.2-9.5                       | 9                     | 1                         | 5.1             | 0.7              | 3.7              | 9.6  |
| 25785       | 2.17-5.85    | 1.0-11.0                      | 42                    | 1                         | 5.1             | 0                | 0-4.3            | 8.6  |
| 26333       | 1.41-1.97    | 3.0-7.5                       | 7                     | 0.7                       | 5.2             | 0.7              | 0                | 6.5  |
| 26612       | 1.62-1.96    | 2.0-3.6                       | 10                    | 0.8                       | 2.5             | 0                | 2.37             | 4.8  |
| 26717       | 1.57-1.93    | 6.0-10.0                      | 7                     | 1                         | 2.5-5.0         | 0.8              | 0                | 9.5  |

# Appendix D

## Velocimetry: plasma parameters

Plasma parameters of the analysed sawtooth crashes are summarized in table D.1. The following notation is used:  $t$  is the crash time;  $f_{mode}$  is the frequency of the (1,1) mode before the crash;  $I_p$  is the plasma current;  $NBI$  is the neutral beam injection;  $ECRH$  and  $ICRH$  are the electron and ion cyclotron resonant heating, respectively;  $T_e^{core}$  and  $n_e^{core}$  are the core plasma electron temperature and density, respectively;  $r_{q=1}$  is the radius of the  $q = 1$  magnetic surface before the crash;  $\beta_N$  is normalized plasma beta [Zohm, 2015, pg. 118]. The axial toroidal magnetic field for all considered shots was  $B_t = 2.5 T$ .

Table D.1: Plasma parameters of the studied sawtooth crashes

| <i>Shot</i> | $t$ [s] | $f_{mode}$ [kHz] | $I_p$ [MA] | $NBI$ [MW] | $ECRH$ [MW] | $ICRH$ [MW] | $T_e^{core}$ [keV] | $n_e^{core}$ [ $10^{19} m^{-3}$ ] | $r_{q=1}$ [m] | $\beta_N$ [%] |
|-------------|---------|------------------|------------|------------|-------------|-------------|--------------------|-----------------------------------|---------------|---------------|
| 25775       | 2.064   | 1.4              | 1          | 0          | 0           | 4.5         | 2.1                | 8.6                               | 0.159         | 0.9           |
| 25775       | 2.48    | 1.3              | 1          | 0          | 0           | 4.5         | 2.1                | 8.6                               | 0.159         | 0.9           |
| 25775       | 2.526   | 1.6              | 1          | 2.6        | 0           | 4.5         | 2.4                | 8.6                               | 0.173         | 1.15          |
| 25782       | 2.32    | 3.2              | 1          | 5.1        | 1.7         | 4.3         | 3.0                | 8.8                               | 0.165         | 1.43          |
| 25782       | 3.143   | 7                | 1          | 5.1        | 1.7         | 4.3         | 4.5                | 8.8                               | 0.155         | 1.9           |
| 26612       | 1.929   | 2.7              | 0.8        | 2.5        | 0           | 2.37        | 2.5                | 4.8                               | 0.150         | 0.9           |

# Appendix E

## Plasma vortices during the crash phase

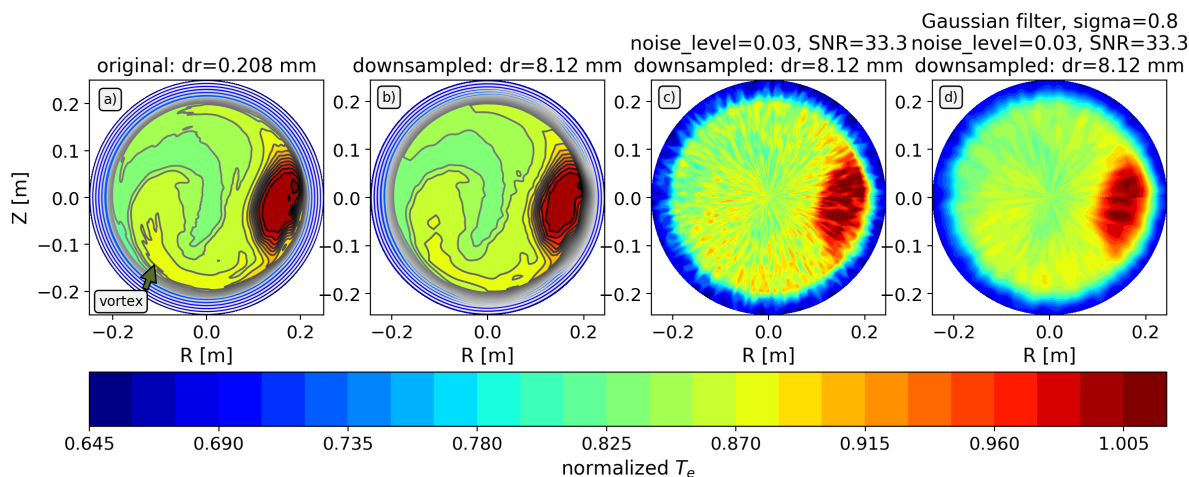


Figure E.1: (a) Original contour plot of the nonlinear simulation, the plasma vortex is indicated with an arrow; (b) original plot with the reduced spatial resolution to the level of the ECEI resolution; (c) Gaussian distribution noise with the noise level 0.03 is added to the plot (b); Gaussian image filter applied ( $\sigma = 0.8$ ) to the plot (c). The amplitude of the plasma vortex is below the noise level.

The nonlinear simulation result showed a presence of plasma vortices (fig. E.1a), which we have not yet been experimentally observed in ASDEX Upgrade. Here we want to study the technical possibility of measuring them with ECEI diagnostic. The strategy is to apply the level of noise present during ECEI measurements to the numerical result. Then then see whether the vortices are observable in the resulting "noised" temperature profile.

The noise present during measurements of electron radiation temperature in optically dense plasma (the condition is satisfied in our core plasma measurements) has form of white noise [Cavallo and Cano, 1981, Cima et al., 1995] (power spectral density of the

noise is constant in frequency range). To estimate the noise level in ECEI diagnostic we use so-called radiometer formula [Hartfuss et al., 1997b]:

$$Noise\ level = \frac{1}{Signal\ to\ noise\ ratio\ (SNR)} = \frac{\sqrt{\langle i^2 \rangle}}{\langle I \rangle} = \sqrt{\frac{2B_v}{B_{IF}}}$$

where  $\sqrt{\langle i^2 \rangle}$  is standard deviation of relative signal fluctuation;  $\langle I \rangle$  is mean signal value;  $B_v$  is video bandwidth;  $B_{IF}$  is intermediate frequency bandwidth.

The noise level of ECEI in ASDEX Upgrade ( $B_v = 0.4\ MHz$ ,  $B_{IF} = 700\ MHz$ ):

$$Noise\ level = \frac{1}{SNR} \approx 0.03$$

Before applying the noise to the numerical data, we first downsample the spatial resolution of this data to match the spatial resolution of the ECEI diagnostic ( $\approx 8\ mm$ ). The original normalized temperature plot is shown in fig. E.1a, whereas downsampled one is shown in the fig. E.1b. To the downsampled data we apply the noise in the following way. Firstly, we create a dataset of random uniform distribution with the standard deviation  $\sigma = \sqrt{\langle i^2 \rangle} = \langle I \rangle \sqrt{\frac{2B_v}{B_{IF}}}$ , where mean signal  $\langle I \rangle$  found from downsampled simulation data,  $B_v$  and  $B_{IF}$  are ECEI diagnostic parameters. The created dataset has the same structure and dimensionality as our downsampled simulation data. Then, the "noised" data we get by summing the dataset and downsampled simulation data together (fig. E.1c). Finally, in fig. E.1d we apply the same noise filter (Gaussian 2D filter [SciPyndimage, 2021] with  $\sigma = 0.8$ ) as we normally apply to the ECEI data (fig. 4.4) to make direct comparison with the ECEI radiation temperature 2D profiles.

From fig. E.1 c and d we conclude, although experimentally we have never observed the plasma vortexes which are present in the nonlinear simulation. It is likely that these vortexes structure are "drowned" in the thermal noise of plasma.

# Bibliography

- [Con, 2017] (2017). Convolution example. Link to the website [github.com/OKStateACM/AIWorkshop](https://github.com/OKStateACM/AIWorkshop).
- [Sta, 2022] (2022). Nuclear power plants by country 2021 | Statista. <https://www.statista.com/statistics/267159/number-of-nuclear-reactors-in-operation-by-country>. [Online; accessed 24. Mar. 2022].
- [Aja-Fernández and Vegas-Sánchez-Ferrero, 2016] Aja-Fernández, S. and Vegas-Sánchez-Ferrero, G. (2016). Statistical analysis of noise in mri. *Switzerland: Springer International Publishing*.
- [Andrés et al., 2014] Andrés, N., Martin, L., Dmitruk, P., and Gómez, D. (2014). Effects of electron inertia in collisionless magnetic reconnection. *Phys. Plasma*, 21(7):072904.
- [Ara et al., 1978] Ara, G., Basu, B., Coppi, B., Laval, G., Rosenbluth, M., and Waddell, B. (1978). Magnetic reconnection and  $m=1$  oscillations in current carrying plasmas. *Annals of Physics*, 112(2):443–476.
- [Armstrong et al., 1994] Armstrong, J., Rickett, B., and Spangler, S. (1994). Electron density power spectrum in the local interstellar medium.
- [Artsimovich, 1972] Artsimovich, L. (1972). Tokamak devices. *Nuclear Fusion*, 12(2):215.
- [Aydemir, 1992] Aydemir, A. (1992). Nonlinear studies of  $m=1$  modes in high-temperature plasmas. *Physics of Fluids B: Plasma Physics*, 4(11):3469–3472.
- [Azam et al., 2015] Azam, H., Gao, B.-X., Liu, W.-D., Xie, J.-L., Team, E., et al. (2015). Electron cyclotron emission imaging observations of  $m/n=1/1$  and higher harmonic modes during sawtooth oscillation in icrf heating plasma on east. *Chinese Physics Letters*, 32(6):065201.
- [Balescu, 1988] Balescu, R. (1988). *Classical Transport*. North Holland.
- [Barbarino, 2020] Barbarino, M. (2020). A brief history of nuclear fusion. *Nature Physics*, 16(9):890–893.

- [Baty et al., 1992] Baty, H., Luciani, J.-F., and Bussac, M.-N. (1992). Asymmetric reconnection and stochasticity in tokamaks. *Nucl. Fusion*, 32(7):1217–1223.
- [Baumjohann and Treumann, 2012] Baumjohann, W. and Treumann, R. A. (2012). *Basic space plasma physics*. World Scientific.
- [Bhattacharjee et al., 2005] Bhattacharjee, A., Germaschewski, K., and Ng, C. (2005). Current singularities: Drivers of impulsive reconnection. *Physics of plasmas*, 12(4):042305.
- [Birn et al., 2001] Birn, J., Drake, J. F., Shay, M. A., Rogers, B. N., Denton, R. E., Hesse, M., Kuznetsova, M., Ma, Z. W., Bhattacharjee, A., Otto, A., and Pritchett, P. L. (2001). Geospace Environmental Modeling (GEM) Magnetic Reconnection Challenge. *J. Geophys. Res. Space Phys.*, 106(A3):3715–3719.
- [Bishop, 1960] Bishop, A. S. (1960). *Project Sherwood: the US program in controlled fusion*. Anchor Books.
- [Biskamp, 1997] Biskamp, D. (1997). *Nonlinear magnetohydrodynamics*. Number 1. Cambridge University Press.
- [Biskamp et al., 1997] Biskamp, D., Schwarz, E., and Drake, J. F. (1997). Two-fluid theory of collisionless magnetic reconnection. *Physics of Plasmas*, 4(4):1002–1009.
- [Bondeson et al., 1992] Bondeson, A., Vlad, G., and Lütjens, H. (1992). Resistive toroidal stability of internal kink modes in circular and shaped tokamaks. *Phys. Fluids B*, 4(7):1889–1900.
- [Boyd et al., 2003] Boyd, T., Boyd, T., and Sanderson, J. (2003). *The physics of plasmas*. Cambridge University Press.
- [Brown and Hwang, 1997] Brown, R. G. and Hwang, P. Y. (1997). Introduction to random signals and applied kalman filtering: with matlab exercises and solutions. *Introduction to random signals and applied Kalman filtering: with MATLAB exercises and solutions*.
- [Bussac et al., 1975] Bussac, M., Pellat, R., Edery, D., and Soule, J. (1975). Internal kink modes in toroidal plasmas with circular cross sections. *Physical Review Letters*, 35(24):1638.
- [Bussac and Pellat, 1987] Bussac, M. N. and Pellat, R. (1987). Nonlinear Evolution of the Internal Kink in Tokamaks. *Phys. Rev. Lett.*, 59(23):2650–2653.
- [Bussac et al., 1984] Bussac, M. N., Pellat, R., Soule, J. L., and Tagger, M. (1984). Half-coalescence of the m=1, n=1 magnetic island in tokamaks. *Phys. Lett. A*, 105(1):51–53.
- [Candy, 2016] Candy, J. V. (2016). *Bayesian signal processing: classical, modern, and particle filtering methods*, volume 54. John Wiley & Sons.

- [Cassak, 2006] Cassak, P. A. (2006). *Catastrophe model for the onset of fast magnetic reconnection*. University of Maryland, College Park.
- [Cavallo and Cano, 1981] Cavallo, A. and Cano, R. (1981). Measurement of apparent turbulent temperature fluctuations on the TFR Tokamak. *Plasma Phys.*, 23(1):61–65.
- [Chang and Callen, 1992] Chang, Z. and Callen, J. D. (1992). Unified fluid/kinetic description of plasma microinstabilities. Part II: Applications. *Phys. Fluids B*, 4(5):1182–1192.
- [Chapman, 2010] Chapman, I. T. (2010). Controlling sawtooth oscillations in tokamak plasmas. *Plasma Phys. Controlled Fusion*, 53(1):013001.
- [Chapman et al., 2010] Chapman, I. T., Buttery, R. J., Coda, S., Gerhardt, S., Graves, J. P., Howell, D. F., Isayama, A., La Haye, R. J., Liu, Y., Maget, P., Maraschek, M., Sabbagh, S., Sauter, O., Upgrade, T. A., Diii-D., H1-2a, Jt-60u, Mast, Nstx, Tcv, and Tore Supra Teams and JET-EFDA Contributors (2010). Empirical scaling of sawtooth period for onset of neoclassical tearing modes. *Nucl. Fusion*, 50(10):102001.
- [Chen, 2011] Chen, F. F. (2011). *An indispensable truth: how fusion power can save the planet*. Springer.
- [Chen, 2016] Chen, F. F. (2016). *Introduction to Plasma Physics and Controlled Fusion*. Springer, Cham, Switzerland.
- [Chen and Hau, 2022] Chen, G.-W. and Hau, L.-N. (2022). Evidence of Magnetic Reconnection with Multiple X Lines and Flux Ropes in Thin Magnetotail Currents Observed by the MMS Spacecraft: Results of Grad–Shafranov Reconstruction. *Astrophys. J.*, 928(2):133.
- [Cima et al., 1995] Cima, G., Bravenec, R. V., Wootton, A. J., Rempel, T. D., Gandy, R. F., Watts, C., and Kwon, M. (1995). Core temperature fluctuations and related heat transport in the Texas Experimental Tokamak-Upgrade. *Phys. Plasma*, 2(3):720–726.
- [Classen et al., 2007] Classen, I., Godefridus, I., and Classen, J. (2007). Imaging and control of magnetic islands in tokamaks.
- [Classen et al., 2010] Classen, I. G. J., Boom, J. E., Suttrop, W., Schmid, E., Tobias, B., Domier, C. W., Luhmann, N. C., Donné, A. J. H., Jaspers, R. J. E., de Vries, P. C., Park, H. K., Munsat, T., García-Muñoz, M., and Schneider, P. A. (2010). 2D electron cyclotron emission imaging at ASDEX Upgrade (invited). *Rev. Sci. Instrum.*, 81(10):10D929.
- [Coppi et al., 1976] Coppi, B., Galvao, R., Pellat, R., Rosenbluth, M., and Rutherford, P. (1976). Resistive internal kink modes. *Soviet Journal of Plasma Physics*, 2:533–535.
- [Cozzani, 2020] Cozzani, G. (2020). *Microphysics of magnetic reconnection in near-Earth space: spacecraft observations and numerical simulations*. Springer Nature.

- [Creely et al., 2020] Creely, A., Greenwald, M., Ballinger, S., Brunner, D., Canik, J., Doody, J., Fülöp, T., Garnier, D., Granetz, R., Gray, T., et al. (2020). Overview of the sparc tokamak. *Journal of Plasma Physics*, 86(5).
- [Dal Pino and Lazarian, 2000] Dal Pino, E. M. d. G. and Lazarian, A. (2000). Ultra-high-energy cosmic-ray acceleration by magnetic reconnection in newborn accretion-induced collapse pulsars. *The Astrophysical Journal*, 536(1):L31.
- [Daughton et al., 2011] Daughton, W., Roytershteyn, V., Karimabadi, H., Yin, L., Albright, B., Bergen, B., and Bowers, K. (2011). Role of electron physics in the development of turbulent magnetic reconnection in collisionless plasmas. *Nature Physics*, 7(7):539–542.
- [De Blank, 2008] De Blank, H. J. (2008). Mhd instabilities in tokamaks. *Fusion Science and Technology*, 53(2T):122–134.
- [de Cheveigné and Nelken, 2019] de Cheveigné, A. and Nelken, I. (2019). Filters: when, why, and how (not) to use them. *Neuron*, 102(2):280–293.
- [DeGrassie et al., 2007] DeGrassie, J., Rice, J., Burrell, K., Groebner, R., and Solomon, W. (2007). Intrinsic rotation in diii-d. *Physics of Plasmas*, 14(5):056115.
- [Dinklage et al., 2005] Dinklage, A., Klinger, T., Marx, G., and Schweikhard, L. (2005). *Plasma physics: confinement, transport and collective effects*, volume 670. Springer Science & Business Media.
- [Dorfman et al., 2013] Dorfman, S., Ji, H., Yamada, M., Yoo, J., Lawrence, E., Myers, C., and Tharp, T. (2013). Three-dimensional, impulsive magnetic reconnection in a laboratory plasma. *Geophysical Research Letters*, 40(2):233–238.
- [Drake and Kleva, 1991] Drake, J. and Kleva, R. (1991). Collisionless reconnection and the sawtooth crash. *Physical review letters*, 66(11):1458.
- [Dungey, 1989] Dungey, J. (1989). Noise-free neutral sheets. *Reconnection in Space Plasma*, 2:15–19.
- [Dungey, 1961] Dungey, J. W. (1961). Interplanetary magnetic field and the auroral zones. *Physical Review Letters*, 6(2):47.
- [Ebrahimi and Raman, 2015] Ebrahimi, F. and Raman, R. (2015). Plasmoids formation during simulations of coaxial helicity injection in the national spherical torus experiment. *Physical Review Letters*, 114(20):205003.
- [Eriksson et al., 2016] Eriksson, S., Wilder, F. D., Ergun, R. E., Schwartz, S. J., Cassak, P. A., Burch, J. L., Chen, L.-J., Torbert, R. B., Phan, T. D., Lavraud, B., Goodrich, K. A., Holmes, J. C., Stawarz, J. E., Sturmer, A. P., Malaspina, D. M., Usanova, M. E., Trattner, K. J., Strangeway, R. J., Russell, C. T., Pollock, C. J., Giles, B. L., Hesse, M.,

- Lindqvist, P.-A., Drake, J. F., Shay, M. A., Nakamura, R., and Marklund, G. T. (2016). Magnetospheric Multiscale Observations of the Electron Diffusion Region of Large Guide Field Magnetic Reconnection. *Phys. Rev. Lett.*, 117(1):015001.
- [Fitzpatrick, 2004] Fitzpatrick, R. (2004). Scaling of forced magnetic reconnection in the hall-magnetohydrodynamic taylor problem. *Physics of Plasmas*, 11(3):937–946.
- [Fox et al., 2017] Fox, W., Sciortino, F., V. Stechow, A., Jara-Almonte, J., Yoo, J., Ji, H., and Yamada, M. (2017). Experimental Verification of the Role of Electron Pressure in Fast Magnetic Reconnection with a Guide Field. *Phys. Rev. Lett.*, 118(12):125002.
- [Fu et al., 2017] Fu, H. S., Vaivads, A., Khotyaintsev, Y. V., André, M., Cao, J. B., Olshevsky, V., Eastwood, J. P., and Retinò, A. (2017). Intermittent energy dissipation by turbulent reconnection. *Geophys. Res. Lett.*, 44(1):37–43.
- [Genestreti et al., 2018] Genestreti, K. J., Varsani, A., Burch, J. L., Cassak, P. A., Torbert, R. B., Nakamura, R., Ergun, R. E., Phan, T.-D., Toledo-Redondo, S., Hesse, M., Wang, S., Giles, B. L., Russell, C. T., Vörös, Z., Hwang, K.-J., Eastwood, J. P., Lavraud, B., Escoubet, C. P., Fear, R. C., Khotyaintsev, Y., Nakamura, T. K. M., Webster, J. M., and Baumjohann, W. (2018). MMS Observation of Asymmetric Reconnection Supported by 3-D Electron Pressure Divergence. *J. Geophys. Res. Space Phys.*, 123(3):1806–1821.
- [Gimblett and Hastie, 1994] Gimblett, C. G. and Hastie, R. J. (1994). Calculation of the post-crash state and 1 1/2 D simulation of sawtooth cycles. *Plasma Phys. Controlled Fusion*, 36(9):1439–1455.
- [Goedbloed et al., 2004] Goedbloed, J. H., Goedbloed, J., and Poedts, S. (2004). *Principles of magnetohydrodynamics: with applications to laboratory and astrophysical plasmas*. Cambridge university press.
- [Goedbloed et al., 2010] Goedbloed, J. P., Keppens, R., and Poedts, S. (2010). *Advanced magnetohydrodynamics: with applications to laboratory and astrophysical plasmas*. Cambridge University Press.
- [Golub et al., 1999] Golub, L., Bookbinder, J., DeLuca, E., Karovska, M., Warren, H., Schrijver, C., Shine, R., Tarbell, T., Title, A., Wolfson, J., et al. (1999). A new view of the solar corona from the transition region and coronal explorer (trace). *Physics of Plasmas*, 6(5):2205–2216.
- [Gonzalez and Woods, 2018] Gonzalez, R. C. and Woods, R. E. (2018). Digital image processing, global edition. *Digital Image Processing, Global Edition*, 19.
- [Gore, 2007] Gore, A. (2007). *An Inconvenient Truth: The Crisis of Global Warming*. Viking Books for Young Readers, New York, NY, USA.

- [Granier et al., 2022] Granier, C., Borgogno, D., Grasso, D., and Tassi, E. (2022). Gyrofluid analysis of electron  $\beta_e$  effects on collisionless reconnection. *Journal of Plasma Physics*, 88(1).
- [Green et al., 2003] Green, B. et al. (2003). Iter: burning plasma physics experiment. *Plasma physics and controlled fusion*, 45(5):687.
- [Günter et al., 2015] Günter, S., Yu, Q., Lackner, K., Bhattacharjee, A., and Huang, Y. (2015). Fast sawtooth reconnection at realistic lundquist numbers. *Plasma Physics and Controlled Fusion*, 57(1):014017.
- [Gurnett and Bhattacharjee, 2017] Gurnett, D. A. and Bhattacharjee, A. (2017). *Introduction to plasma physics: With space, laboratory and astrophysical applications*. Cambridge University Press.
- [Hardy, 2003] Hardy, J. T. (2003). *Climate change: causes, effects, and solutions*. John Wiley & Sons.
- [Hare et al., 2017] Hare, J., Suttle, L., Lebedev, S., Loureiro, N., Ciardi, A., Burdiak, G., Chittenden, J., Clayson, T., Garcia, C., Niasse, N., et al. (2017). Anomalous heating and plasmoid formation in a driven magnetic reconnection experiment. *Physical review letters*, 118(8):085001.
- [Hartfuss et al., 1997a] Hartfuss, H., Geist, T., and Hirsch, M. (1997a). Heterodyne methods in millimetre wave plasma diagnostics with applications to ece, interferometry and reflectometry. *Plasma Physics and Controlled Fusion*, 39(11):1693.
- [Hartfuss et al., 1997b] Hartfuss, H. J., Geist, T., and Hirsch, M. (1997b). Heterodyne methods in millimetre wave plasma diagnostics with applications to ECE, interferometry and reflectometry. *Plasma Phys. Controlled Fusion*, 39(11):1693.
- [Hastie et al., 1987] Hastie, R., Hender, T., Carreras, B., Charlton, L., and Holmes, J. (1987). Stability of ideal and resistive internal kink modes in toroidal geometry. *The Physics of fluids*, 30(6):1756–1766.
- [Hender et al., 2007] Hender, T., Wesley, J., Bialek, J., Bondeson, A., Boozer, A., Buttery, R., Garofalo, A., Goodman, T., Granetz, R., Gribov, Y., et al. (2007). Mhd stability, operational limits and disruptions. *Nuclear fusion*, 47(6):S128.
- [Henry and Hofrichter, 1992] Henry, E. and Hofrichter, J. (1992). [8] singular value decomposition: Application to analysis of experimental data. In *Methods in enzymology*, volume 210, pages 129–192. Elsevier.
- [Herrmann and Gruber, 2003] Herrmann, A. and Gruber, O. (2003). Chapter 1: Asdex upgrade-introduction and overview. *Fusion Science and Technology*, 44(3):569–577.

- [Hesse et al., 2004] Hesse, M., Kuznetsova, M., and Birn, J. (2004). The role of electron heat flux in guide-field magnetic reconnection. *Phys. Plasma*, 11(12):5387–5397.
- [Hesse et al., 2002] Hesse, M., Kuznetsova, M., and Hoshino, M. (2002). The structure of the dissipation region for component reconnection: Particle simulations. *Geophysical research letters*, 29(12):4–1.
- [Hoffert et al., 2002] Hoffert, M. I., Caldeira, K., Benford, G., Criswell, D. R., Green, C., Herzog, H., Jain, A. K., Kheshgi, H. S., Lackner, K. S., Lewis, J. S., et al. (2002). Advanced technology paths to global climate stability: energy for a greenhouse planet. *science*, 298(5595):981–987.
- [Horiuchi et al., 2014] Horiuchi, R., Usami, S., and Ohtani, H. (2014). Influence of a Guide Field on Collisionless Driven Reconnection. *Plasma and Fusion Research*, 9:1401092.
- [Hu et al., 2006] Hu, B., Betti, R., and Manickam, J. (2006). Kinetic stability of the internal kink mode in iter. *Physics of plasmas*, 13(11):112505.
- [Huang and Bhattacharjee, 2010] Huang, Y.-M. and Bhattacharjee, A. (2010). Scaling laws of resistive magnetohydrodynamic reconnection in the high-lundquist-number, plasmoid-unstable regime. *Physics of Plasmas*, 17(6):062104.
- [Huang and Bhattacharjee, 2013] Huang, Y.-M. and Bhattacharjee, A. (2013). Plasmoid instability in high-lundquist-number magnetic reconnection. *Physics of Plasmas*, 20(5):055702.
- [Huba, 2005] Huba, J. D. (2005). Hall magnetic reconnection: Guide field dependence. *Phys. Plasma*, 12(1):012322.
- [Hussain et al., 2021] Hussain, A., Xie, J., and Liu, W. (2021). Experimental investigation of a partial collapse during the sawtooth instability in east. *Radiation Effects and Defects in Solids*, 176(7-8):591–600.
- [Hutchinson, 2002] Hutchinson, I. H. (2002). Principles of plasma diagnostics. *Plasma Physics and Controlled Fusion*, 44(12):2603.
- [Igochine et al., 2010a] Igochine, V., Boom, J., Classen, I., Dumbrajs, O., Günter, S., Lackner, K., Pereverzev, G., Zohm, H., and Team, A. U. (2010a). Structure and dynamics of sawteeth crashes in asdex upgrade. *Physics of Plasmas*, 17(12):122506.
- [Igochine et al., 2006a] Igochine, V., Dumbrajs, O., Constantinescu, D., Zohm, H., Zvejniéks, G., et al. (2006a). Stochastization as a possible cause for fast reconnection during mhd mode activity in the asdex upgrade tokamak. *Nuclear fusion*, 46(7):741.
- [Igochine et al., 2008] Igochine, V., Dumbrajs, O., Zohm, H., et al. (2008). Transition from quasiperiodicity to chaos just before sawtooth crash in the asdex upgrade tokamak. *Nuclear fusion*, 48(6):062001.

- [Igochine et al., 2006b] Igochine, V., Dumbrajs, O., Zohm, H., Flaws, A., and Team, T. A. U. (2006b). Stochastic sawtooth reconnection in ASDEX Upgrade. *Nucl. Fusion*, 47(1):23.
- [Igochine et al., 2015] Igochine, V. et al. (2015). *Active control of magneto-hydrodynamic instabilities in hot plasmas*. Springer.
- [Igochine et al., 2010b] Igochine, V., Gude, A., Maraschek, M., and Team, A. U. (2010b). Hotlink based soft x-ray diagnostic on asdex upgrade.
- [Inan and Gołkowski, 2010] Inan, U. S. and Gołkowski, M. (2010). *Principles of plasma physics for engineers and scientists*. Cambridge university press.
- [Isayama et al., 2003] Isayama, A., Kamada, Y., Hayashi, N., Suzuki, T., Oikawa, T., Fujita, T., Fukuda, T., Ide, S., Takenaga, H., Ushigusa, K., Ozeki, T., Ikeda, Y., Umeda, N., Yamada, H., Isobe, M., Narushima, Y., Ikeda, K., Sakakibara, S., Yamazaki, K., Nagasaki, K., and Team, T. J. T.-. (2003). Achievement of high fusion triple product, steady-state sustainment and real-time NTM stabilization in high- $\beta_p$  ELMy H-mode discharges in JT-60U. *Nucl. Fusion*, 43(10):1272–1278.
- [Jara-Almonte et al., 2016] Jara-Almonte, J., Ji, H., Yamada, M., Yoo, J., and Fox, W. (2016). Laboratory observation of resistive electron tearing in a two-fluid reconnecting current sheet. *Physical review letters*, 117(9):095001.
- [Jardin et al., 2020] Jardin, S. C., Krebs, I., and Ferraro, N. (2020). A new explanation of the sawtooth phenomena in tokamaks. *Physics of Plasmas*, 27(3):032509.
- [Ji and Daughton, 2011] Ji, H. and Daughton, W. (2011). Phase diagram for magnetic reconnection in heliophysical, astrophysical, and laboratory plasmas. *Physics of Plasmas*, 18(11):111207.
- [Ji et al., 2022] Ji, H., Daughton, W., Jara-Almonte, J., Le, A., Stanier, A., and Yoo, J. (2022). Magnetic reconnection in the era of exascale computing and multiscale experiments. *Nature Reviews Physics*, pages 1–20.
- [Jiang et al., 2015] Jiang, M., Shi, Z., Domier, C., Luhmann Jr, N., Zhong, W., Chen, W., Liu, Z., Ding, X., Yang, Q., Zhang, B., et al. (2015). Note: Upgrade of electron cyclotron emission imaging system and preliminary results on hl-2a tokamak. *Review of Scientific Instruments*, 86(7):076107.
- [Kadomtsev, 1975] Kadomtsev, B. B. (1975). Disruptive instability in Tokamaks. *Fiz. Plazmy*, 1:710–715.
- [Karimabadi et al., 1999] Karimabadi, H., Krauss-Varban, D., Omidi, N., and Vu, H. (1999). Magnetic structure of the reconnection layer and core field generation in plasmoids. *Journal of Geophysical Research: Space Physics*, 104(A6):12313–12326.

- [Karimabadi et al., 2013] Karimabadi, H., Roytershteyn, V., Wan, M., Matthaeus, W., Daughton, W., Wu, P., Shay, M., Loring, B., Borovsky, J., Leonardis, E., et al. (2013). Coherent structures, intermittent turbulence, and dissipation in high-temperature plasmas. *Physics of Plasmas*, 20(1):012303.
- [Kautsky et al., 2016] Kautsky, U., Saetre, P., Berglund, S., Jaeschke, B., Nordén, S., Brandefelt, J., Keesmann, S., Näslund, J.-O., and Andersson, E. (2016). The impact of low and intermediate-level radioactive waste on humans and the environment over the next one hundred thousand years. *J. Environ. Radioact.*, 151:395–403.
- [Keilhacker et al., 1999] Keilhacker, M., Gibson, A., Gormezano, C., Lomas, P. J., Thomas, P. R., Watkins, M. L., Andrew, P., Balet, B., Borba, D., Challis, C. D., Coffey, I., Cottrell, G. A., De Esch, H. P. L., Deliyannis, N., Fasoli, A., Gowers, C. W., Guo, H. Y., Huysmans, G. T. A., Jones, T. T. C., Kerner, W., König, R. W. T., Loughlin, M. J., Maas, A., Marcus, F. B., Nave, M. F. F., Rimini, F. G., Sadler, G. J., Sharapov, S. E., Sips, G., Smeulders, P., Söldner, F. X., Taroni, A., Tubbing, B. J. D., von Hellermann, M. G., Ward, D. J., and Team, J. (1999). High fusion performance from. *Nucl. Fusion*, 39(2):209–234.
- [Khotyaintsev et al., 2019] Khotyaintsev, Y. V., Graham, D. B., Norgren, C., and Vaivads, A. (2019). Collisionless Magnetic Reconnection and Waves: Progress Review. *Front. Astron. Space Sci.*, 0.
- [Kleva et al., 1995] Kleva, R. G., Drake, J., and Waelbroeck, F. (1995). Fast reconnection in high temperature plasmas. *Physics of Plasmas*, 2(1):23–34.
- [Kolesnichenko and Yakovenko, 2013] Kolesnichenko, Y. I. and Yakovenko, Y. V. (2013). Can the stochasticity of field lines be responsible for sawtooth crashes? *Plasma Phys. Controlled Fusion*, 55(11):115006.
- [Kowal et al., 2009] Kowal, G., Lazarian, A., Vishniac, E., and Otmianowska-Mazur, K. (2009). Numerical tests of fast reconnection in weakly stochastic magnetic fields. *The Astrophysical Journal*, 700(1):63.
- [Krall and Trivelpiece, 1973] Krall, N. A. and Trivelpiece, A. W. (1973). Principles of plasma physics. *American Journal of Physics*, 41(12):1380–1381.
- [Krane, 1991] Krane, K. S. (1991). *Introductory nuclear physics*. John Wiley & Sons.
- [Krebs et al., 2017] Krebs, I., Jardin, S., Günter, S., Lackner, K., Hoelzl, M., Strumberger, E., and Ferraro, N. (2017). Magnetic flux pumping in 3d nonlinear magnetohydrodynamic simulations. *Physics of Plasmas*, 24(10):102511.
- [Kulsrud, 1983] Kulsrud, R. M. (1983). Mhd description of plasma. *Handbook of plasma physics*, 1:115.

- [Kuritsyn et al., 2006] Kuritsyn, A., Yamada, M., Gerhardt, S., Ji, H., Kulsrud, R., and Ren, Y. (2006). Measurements of the parallel and transverse spitzer resistivities during collisional magnetic reconnection. *Physics of Plasmas*, 13(5):055703.
- [Lathi and Green, 2014] Lathi, B. P. and Green, R. A. (2014). *Essentials of digital signal processing*. Cambridge University Press.
- [Lawson, 1957] Lawson, J. D. (1957). Some criteria for a power producing thermonuclear reactor. *Proceedings of the physical society. Section B*, 70(1):6.
- [Lazarian, 2005] Lazarian, A. (2005). Astrophysical Implications of Turbulent Reconnection: from cosmic rays to star formation. *AIP Conf. Proc.*, 784(1):42–53.
- [Lazarian and Vishniac, 1999] Lazarian, A. and Vishniac, E. T. (1999). Reconnection in a weakly stochastic field. *The Astrophysical Journal*, 517(2):700.
- [Liang et al., 2007] Liang, Y., Koslowski, H., Krämer-Flecken, A., Zimmermann, O., Löwenbrück, K., Bertschinger, G., Wolf, R., et al. (2007). Observations of secondary structures after collapse events occurring at the  $q=2$  magnetic surface in the textor tokamak. *Nuclear fusion*, 47(9):L21.
- [Lichtenberg et al., 1992] Lichtenberg, A. J., Itoh, K., Itoh, S.-I., and Fukuyama, A. (1992). The role of stochasticity in sawtooth oscillations. *Nucl. Fusion*, 32(3):495–512.
- [Loureiro and Uzdensky, 2015] Loureiro, N. and Uzdensky, D. (2015). Magnetic reconnection: from the sweet–parker model to stochastic plasmoid chains. *Plasma Physics and Controlled Fusion*, 58(1):014021.
- [Loureiro and Boldyrev, 2020] Loureiro, N. F. and Boldyrev, S. (2020). Nonlinear reconnection in magnetized turbulence. *The Astrophysical Journal*, 890(1):55.
- [Loureiro et al., 2007] Loureiro, N. F., Schekochihin, A. A., and Cowley, S. C. (2007). Instability of current sheets and formation of plasmoid chains. *Phys. Plasma*, 14(10):100703.
- [Luda et al., 2020] Luda, T., Angioni, C., Dunne, M. G., Fable, E., Kallenbach, A., Bonanomi, N., Schneider, P. A., Siccino, M., Tardini, G., Team, T. A. U., and Team, T. E. M. (2020). Integrated modeling of ASDEX Upgrade plasmas combining core, pedestal and scrape-off layer physics. *Nucl. Fusion*, 60(3):036023.
- [Lutjens et al., 1992] Lutjens, H., Bondeson, A., and Vlad, G. (1992). Ideal MHD stability of internal kinks in circular and shaped tokamaks. *Nucl. Fusion*, 32(9):1625–1636.
- [Lyons and Pridmore-Brown, 1990] Lyons, L. R. and Pridmore-Brown, D. C. (1990). Force balance near an X line in a collisionless plasma. *J. Geophys. Res. Space Phys.*, 95(A12):20903–20909.

- [Lyons, 1997] Lyons, R. G. (1997). *Understanding digital signal processing, 3/E*. Pearson Education India.
- [Lyutikov, 2003] Lyutikov, M. (2003). Explosive reconnection in magnetars. *Monthly Notices of the Royal Astronomical Society*, 346(2):540–554.
- [Ma and Bhattacharjee, 1996] Ma, Z. W. and Bhattacharjee, A. (1996). Fast impulsive reconnection and current sheet intensification due to electron pressure gradients in semi-collisional plasmas. *Geophys. Res. Lett.*, 23(13):1673–1676.
- [Ma and Bhattacharjee, 2001] Ma, Z. W. and Bhattacharjee, A. (2001). Hall magnetohydrodynamic reconnection: The Geospace Environment Modeling challenge. *J. Geophys. Res. Space Phys.*, 106(A3):3773–3782.
- [MacGregor et al., 2021] MacGregor, M. A., Weinberger, A. J., Loyd, R. P., Shkolnik, E., Barclay, T., Howard, W. S., Zic, A., Osten, R. A., Cranmer, S. R., Kowalski, A. F., et al. (2021). Discovery of an extremely short duration flare from proxima centauri using millimeter through far-ultraviolet observations. *The Astrophysical Journal Letters*, 911(2):L25.
- [Malakit, 2012] Malakit, K. (2012). *Asymmetric magnetic reconnection: a particle-in-cell study*. University of Delaware.
- [Martynov et al., 2005] Martynov, A., Graves, J. P., and Sauter, O. (2005). The stability of the ideal internal kink mode in realistic tokamak geometry. *Plasma Phys. Controlled Fusion*, 47(10):1743–1762.
- [Matthaeus and Lamkin, 1986] Matthaeus, W. and Lamkin, S. L. (1986). Turbulent magnetic reconnection. *The Physics of fluids*, 29(8):2513–2534.
- [Merkulov, 2006] Merkulov, O. (2006). *Control of plasma profiles and stability through localised electron cyclotron current drive*. PhD thesis, Utrecht University.
- [Mistry et al., 2016] Mistry, R., Eastwood, J. P., Haggerty, C. C., Shay, M. A., Phan, T. D., Hietala, H., and Cassak, P. A. (2016). Observations of Hall Reconnection Physics Far Downstream of the X Line. *Phys. Rev. Lett.*, 117(18):185102.
- [Mozer et al., 2002] Mozer, F., Bale, S., and Phan, T. (2002). Evidence of diffusion regions at a subsolar magnetopause crossing. *Physical review letters*, 89(1):015002.
- [Munsat et al., 2010] Munsat, T., Domier, C. W., Kong, X., Liang, T., Luhmann Jr, N. C., Tobias, B. J., Lee, W., Park, H. K., Yun, G., Classen, I. G., et al. (2010). Electron cyclotron emission imaging in tokamak plasmas. *Applied optics*, 49(19):E20–E30.
- [Munsat et al., 2007] Munsat, T., Park, H., Classen, I., Domier, C., Donn, A., Luhmann, N., Mazzucato, E., van de Pol, M., and the TEXTOR team (2007). Localization of the magnetic reconnection zone during sawtooth crashes in tokamak plasmas. *Nuclear Fusion*, 47(11):L31–L35.

- [Nagayama et al., 1996] Nagayama, Y., Yamada, M., Park, W., Fredrickson, E. D., Janos, A. C., McGuire, K. M., and Taylor, G. (1996). Tomography of full sawtooth crashes on the Tokamak Fusion Test Reactor. *Physics of Plasmas*, 3(5):1647–1655.
- [Nakamura et al., 2017] Nakamura, T., Hasegawa, H., Daughton, W., Eriksson, S., Li, W. Y., and Nakamura, R. (2017). Turbulent mass transfer caused by vortex induced reconnection in collisionless magnetospheric plasmas. *Nature communications*, 8(1):1–8.
- [Nam et al., 2018] Nam, Y., Ko, J., Choe, G., Bae, Y., Choi, M., Lee, W., Yun, G., Jardin, S., and Park, H. (2018). Validation of the full reconnection model of the sawtooth instability in kstar. *Nuclear Fusion*, 58(6):066009.
- [Nave et al., 2003] Nave, M. F. F., Rapp, J., Bolzonella, T., Dux, R., Mantsinen, M. J., Budny, R., Dumortier, P., von Hellermann, M., Jachmich, S., Koslowski, H. R., Maddison, G., Messiaen, A., Monier-Garbet, P., Ongena, J., Puiatti, M. E., Strachan, J., Telesca, G., Unterberg, B., Valisa, M., de Vries, P., and contributors to the JET-EFDA Workprogramme (2003). Role of sawtooth in avoiding impurity accumulation and maintaining good confinement in JET radiative mantle discharges. *Nucl. Fusion*, 43(10):1204–1213.
- [Nishimura et al., 1999] Nishimura, Y., Callen, J. D., and Hegna, C. C. (1999). Onset of high-n ballooning modes during tokamak sawtooth crashes. *Phys. Plasma*, 6(12):4685–4692.
- [Øieroset et al., 2001] Øieroset, M., Phan, T., Fujimoto, M., Lin, R., and Lepping, R. (2001). In situ detection of collisionless reconnection in the earth’s magnetotail. *Nature*, 412(6845):414–417.
- [Olson et al., 2021] Olson, J., Egedal, J., Clark, M., Endrizzi, D. A., Greess, S., Millet-Ayala, A., Myers, R., Peterson, E. E., Wallace, J., and Forest, C. B. (2021). Regulation of the normalized rate of driven magnetic reconnection through shocked flux pileup. *Journal of Plasma Physics*, 87(3).
- [Olson et al., 2016] Olson, J., Egedal, J., Greess, S., Myers, R., Clark, M., Endrizzi, D., Flanagan, K., Milhone, J., Peterson, E., Wallace, J., et al. (2016). Experimental demonstration of the collisionless plasmoid instability below the ion kinetic scale during magnetic reconnection. *Physical review letters*, 116(25):255001.
- [Ono et al., 2011] Ono, Y., Hayashi, Y., Ii, T., Tanabe, H., Ito, S., Kuwahata, A., Ito, T., Kamino, Y., Yamada, T., Inomoto, M., et al. (2011). Intermittent magnetic reconnection in ts-3 merging experiment. *Physics of Plasmas*, 18(11):111213.
- [Ottaviani and Porcelli, 1993] Ottaviani, M. and Porcelli, F. (1993). Nonlinear collisionless magnetic reconnection. *Physical review letters*, 71(23):3802.

- [Park, 2019] Park, H. K. (2019). Newly uncovered physics of MHD instabilities using 2-D electron cyclotron emission imaging system in toroidal plasmas. *Advances in Physics: X*, 4(1):1633956. Publisher: Taylor & Francis eprint: <https://doi.org/10.1080/23746149.2019.1633956>.
- [Park et al., 2006] Park, H. K., Donn, A. J. H., Luhmann, N. C., Classen, I. G. J., Domier, C. W., Mazzucato, E., Munsat, T., van de Pol, M. J., and Xia, Z. (2006). Comparison Study of 2D Images of Temperature Fluctuations during Sawtooth Oscillation with Theoretical Models. *Physical Review Letters*, 96(19):195004.
- [Park et al., 1995] Park, W., Fredrickson, E. D., Janos, A., Manickam, J., and Tang, W. M. (1995). High- $\beta$  Disruption in Tokamaks. *Phys. Rev. Lett.*, 75(9):1763–1766.
- [Park et al., 1992] Park, W., Parker, S., Biglari, H., Chance, M., Chen, L., Cheng, C. Z., Hahm, T. S., Lee, W. W., Kulsrud, R., Monticello, D., Sugiyama, L., and White, R. (1992). Three-dimensional hybrid gyrokinetic-magnetohydrodynamics simulation. *Phys. Fluids B*, 4(7):2033–2037.
- [Parker, 1957] Parker, E. (1957). Acceleration of cosmic rays in solar flares. *Physical Review*, 107(3):830.
- [Pert, 2021] Pert, G. J. (2021). *Foundations of Plasma Physics for Physicists and Mathematicians*. Wiley, Hoboken, NJ, USA.
- [Pescatore and Vári, 2006] Pescatore, C. and Vári, A. (2006). Stepwise approach to the long-term management of radioactive waste. *Journal of Risk Research*, 9(1):13–40.
- [Phan et al., 2007] Phan, T., Drake, J., Shay, M., Mozer, F., and Eastwood, J. (2007). Evidence for an elongated ( $\approx 60$  ion skin depths) electron diffusion region during fast magnetic reconnection. *Physical Review Letters*, 99(25):255002.
- [Phan et al., 2006] Phan, T., Gosling, J., Davis, M., Skoug, R., Øieroset, M., Lin, R., Lepping, R., McComas, D., Smith, C., Reme, H., et al. (2006). A magnetic reconnection x-line extending more than 390 earth radii in the solar wind. *Nature*, 439(7073):175–178.
- [Porcelli, 1991] Porcelli, F. (1991). Collisionless  $m=1$  tearing mode. *Physical review letters*, 66(4):425.
- [Porcelli et al., 1996] Porcelli, F., Boucher, D., and Rosenbluth, M. N. (1996). Model for the sawtooth period and amplitude. *Plasma Phys. Controlled Fusion*, 38(12):2163–2186.
- [Priest and Forbes, 2000] Priest, E. and Forbes, T. (2000). *Magnetic Reconnection: MHD Theory and Applications*. Cambridge University Press.

- [Pritchett and Coroniti, 2004] Pritchett, P. L. and Coroniti, F. V. (2004). Three-dimensional collisionless magnetic reconnection in the presence of a guide field. *J. Geophys. Res. Space Phys.*, 109(A1).
- [Proakis, 2001] Proakis, J. G. (2001). *Digital signal processing: principles algorithms and applications*. Pearson Education India.
- [Rathgeber, 2013] Rathgeber, S. (2013). *Electron temperature and pressure at the edge of ASDEX Upgrade plasmas*. PhD thesis, Imu.
- [Rechester and Rosenbluth, 1978] Rechester, A. B. and Rosenbluth, M. N. (1978). Electron Heat Transport in a Tokamak with Destroyed Magnetic Surfaces. *Phys. Rev. Lett.*, 40(1):38–41.
- [Reinders, 2021] Reinders, L. J. (2021). *The Fairy Tale of Nuclear Fusion*. Springer, Cham, Switzerland.
- [Ren et al., 2005] Ren, Y., Yamada, M., Gerhardt, S., Ji, H., Kulsrud, R., and Kuritsyn, A. (2005). Experimental verification of the hall effect during magnetic reconnection in a laboratory plasma. *Physical review letters*, 95(5):055003.
- [Retinò et al., 2007] Retinò, A., Sundkvist, D., Vaivads, A., Mozer, F., André, M., and Owen, C. (2007). In situ evidence of magnetic reconnection in turbulent plasma. *Nature Physics*, 3(4):235–238.
- [Ricci et al., 2004a] Ricci, P., Brackbill, J., Daughton, W., and Lapenta, G. (2004a). Collisionless magnetic reconnection in the presence of a guide field. *Physics of plasmas*, 11(8):4102–4114.
- [Ricci et al., 2004b] Ricci, P., Brackbill, J. U., Daughton, W., and Lapenta, G. (2004b). Collisionless magnetic reconnection in the presence of a guide field. *Phys. Plasma*, 11(8):4102–4114.
- [Rogers et al., 2003] Rogers, B. N., Denton, R. E., and Drake, J. F. (2003). Signatures of collisionless magnetic reconnection. *J. Geophys. Res. Space Phys.*, 108(A3).
- [Rosenbluth et al., 1973a] Rosenbluth, M. N., Dagazian, R., and Rutherford, P. (1973a). Nonlinear properties of the internal  $m=1$  kink instability in the cylindrical tokamak. *The Physics of Fluids*, 16(11):1894–1902.
- [Rosenbluth et al., 1973b] Rosenbluth, M. N., Dagazian, R. Y., and Rutherford, P. H. (1973b). Nonlinear properties of the internal  $m=1$  kink instability in the cylindrical tokamak. *Phys. Fluids*, 16(11):1894–1902.
- [Samoylov et al., 2022a] Samoylov, O., Igochine, V., Stegmeir, A., Zohm, H., and Team, T. A. U. (2022a). Global nature of magnetic reconnection during sawtooth crash in ASDEX Upgrade. *J. Plasma Phys.*, 88(1).

- [Samoylov et al., 2022b] Samoylov, O., Igochine, V., Yu, Q., Zohm, H., and Team, T. A. U. (2022b). Magnetic reconnection rate during sawtooth crashes in ASDEX Upgrade. *Nucl. Fusion*, 62(7):074002.
- [Samtaney et al., 2009] Samtaney, R., Loureiro, N. F., Uzdensky, D. A., Schekochihin, A. A., and Cowley, S. C. (2009). Formation of Plasmoid Chains in Magnetic Reconnection. *Phys. Rev. Lett.*, 103(10):105004.
- [Sauter et al., 2002] Sauter, O., Westerhof, E., Mayoral, M. L., Alper, B., Belo, P. A., Buttery, R. J., Gondhalekar, A., Hellsten, T., Hender, T. C., Howell, D. F., Johnson, T., Lamalle, P., Mantsinen, M. J., Milani, F., Nave, M. F. F., Nguyen, F., Pecquet, A. L., Pinches, S. D., Podda, S., and Rapp, J. (2002). Control of Neoclassical Tearing Modes by Sawtooth Control. *Phys. Rev. Lett.*, 88(10):105001.
- [Schafer, 2011] Schafer, R. W. (2011). What Is a Savitzky-Golay Filter? [Lecture Notes]. *IEEE Signal Process. Mag.*, 28(4):111–117.
- [Schmidt et al., 2009] Schmidt, S., Günter, S., and Lackner, K. (2009). Reconnection in semicollisional, low- $\beta$  plasmas. *Physics of Plasmas*, 16(7):072302.
- [Schnack, 2009] Schnack, D. D. (2009). *Lectures in magnetohydrodynamics: with an appendix on extended MHD*, volume 780. Springer.
- [Schnack, 2012] Schnack, D. D. (2012). The internal kink mode and giant sawteeth in tokamaks.
- [SciPy-ndimage, 2021] SciPy-ndimage (2020 (accessed 25-03-2021)). Scipy ndimage: Gaussian filter library. [https://docs.scipy.org/doc/scipy/reference/generated/scipy.ndimage.gaussian\\_filter.html](https://docs.scipy.org/doc/scipy/reference/generated/scipy.ndimage.gaussian_filter.html).
- [Servidio et al., 2009] Servidio, S., Matthaeus, W., Shay, M., Cassak, P., and Dmitruk, P. (2009). Magnetic reconnection in two-dimensional magnetohydrodynamic turbulence. *Physical review letters*, 102(11):115003.
- [Shaing et al., 2010] Shaing, K.-C., Sabbagh, S., and Chu, M. (2010). An approximate analytic expression for neoclassical toroidal plasma viscosity in tokamaks. *Nuclear fusion*, 50(2):025022.
- [Shay et al., 1999] Shay, M., Drake, J., Rogers, B., and Denton, R. (1999). The scaling of collisionless, magnetic reconnection for large systems. *Geophysical research letters*, 26(14):2163–2166.
- [Shibata and Tanuma, 2001] Shibata, K. and Tanuma, S. (2001). Plasmoid-induced-reconnection and fractal reconnection. *Earth, Planets and Space*, 53(6):473–482.

- [Shibata et al., 1995] Shibata, K. c., Masuda, S., Shimojo, M., Hara, H., Yokoyama, T., Tsuneta, S., Kosugi, T., and Ogawara, Y. (1995). Hot-plasma ejections associated with compact-loop solar flares. *The Astrophysical Journal*, 451(2):L83.
- [Smith et al., 2004] Smith, D., Ghosh, S., Dmitruk, P., and Matthaeus, W. (2004). Hall and turbulence effects on magnetic reconnection. *Geophysical research letters*, 31(2).
- [Smith, 2013] Smith, S. (2013). *Digital signal processing: a practical guide for engineers and scientists*. Elsevier.
- [Somov, 2012a] Somov, B. V. (2012a). *Plasma Astrophysics, Part I: Fundamentals and Practice*, volume 391. Springer Science & Business Media.
- [Somov, 2012b] Somov, B. V. (2012b). *Plasma astrophysics, part II: reconnection and flares*, volume 392. Springer Science & Business Media.
- [Somov, 2013] Somov, B. V. (2013). *Cosmic plasma physics*, volume 251. Springer Science & Business Media.
- [Sonnerup, 1988] Sonnerup, B. Ö. (1988). On the theory of steady state reconnection. *Computer Physics Communications*, 49(1):143–159.
- [Speiser, 1970] Speiser, T. W. (1970). Conductivity without collisions or noise. *Planet. Space Sci.*, 18(4):613–622.
- [Spitkovsky, 2006] Spitkovsky, A. (2006). Time-dependent force-free pulsar magnetospheres: axisymmetric and oblique rotators. *The Astrophysical Journal*, 648(1):L51.
- [Spitzer and Härm, 1953] Spitzer, L. and Härm, R. (1953). Transport Phenomena in a Completely Ionized Gas. *Phys. Rev.*, 89(5):977–981.
- [Stacey, 2012] Stacey, W. M. (2012). *Fusion Plasma Physics*.
- [Steger, 2017] Steger, V. (2017). *ASDEX Upgrade, IPP*. <https://www.ipp.mpg.de/4289368/nfaward-17>.
- [Stegmeir et al., 2016] Stegmeir, A., Coster, D., Maj, O., Hallatschek, K., and Lackner, K. (2016). The field line map approach for simulations of magnetically confined plasmas. *Computer Physics Communications*, 198:139–153.
- [Stegmeir et al., 2018] Stegmeir, A., Coster, D., Ross, A., Maj, O., Lackner, K., and Poli, E. (2018). GRILLIX: a 3D turbulence code based on the flux-coordinate independent approach. *Plasma Phys. Controlled Fusion*, 60(3):035005.
- [Steinhauser et al., 2014] Steinhauser, G., Brandl, A., and Johnson, T. E. (2014). Comparison of the chernobyl and fukushima nuclear accidents: a review of the environmental impacts. *Science of the total environment*, 470:800–817.

- [Stenzel et al., 1986] Stenzel, R., Gekelman, W., and Urrutia, J. (1986). Lessons from laboratory experiments on reconnection. *Advances in space research*, 6(1):135–147.
- [Stroth, 2011] Stroth, U. (2011). *Plasmaphysik*. Springer.
- [Sweet, 1958] Sweet, P. (1958). The production of high energy particles in solar flares. *Il Nuovo Cimento (1955-1965)*, 8(2):188–196.
- [Tan and Jiang, 2018] Tan, L. and Jiang, J. (2018). *Digital signal processing: fundamentals and applications*. Academic Press.
- [Tang et al., 2021] Tang, S. Y., Zhang, Y. C., Dai, L., Chen, T., and Wang, C. (2021). MMS Observation of the Hall Field in an Asymmetric Magnetic Reconnection with Guide Field. *Astrophys. J.*, 922(2):96.
- [Taylor and Newton, 2015] Taylor, J. and Newton, S. (2015). Special topics in plasma confinement. *Journal of Plasma Physics*, 81(5).
- [Teller, 2012] Teller, E. (2012). *Fusion Part A: Magnetic Confinement Part A*. Elsevier.
- [Tobias et al., 2009] Tobias, B., Kong, X., Liang, T., Spear, A., Domier, C. W., Luhmann, N. C., Classen, I. G. J., Boom, J. E., van de Pol, M. J., Jaspers, R., Donné, A. J. H., Park, H. K., and Munsat, T. (2009). Advancements in electron cyclotron emission imaging demonstrated by the TEXTOR ECEI diagnostic upgrade. *Rev. Sci. Instrum.*, 80(9):093502.
- [Torbert et al., 2018] Torbert, R. B., Burch, J. L., Phan, T. D., Hesse, M., Argall, M. R., Shuster, J., Ergun, R. E., Alm, L., Nakamura, R., Genestreti, K. J., Gershman, D. J., Paterson, W. R., Turner, D. L., Cohen, I., Giles, B. L., Pollock, C. J., Wang, S., Chen, L.-J., Stawarz, J. E., Eastwood, J. P., Hwang, K. J., Farrugia, C., Dors, I., Vaith, H., Mouikis, C., Ardakani, A., Mauk, B. H., Fuselier, S. A., Russell, C. T., Strangeway, R. J., Moore, T. E., Drake, J. F., Shay, M. A., Khotyaintsev, Y. V., Lindqvist, P.-A., Baumjohann, W., Wilder, F. D., Ahmadi, N., Dorelli, J. C., Avanov, L. A., Oka, M., Baker, D. N., Fennell, J. F., Blake, J. B., Jaynes, A. N., Le Contel, O., Petrinec, S. M., Lavraud, B., and Saito, Y. (2018). Electron-scale dynamics of the diffusion region during symmetric magnetic reconnection in space. *Science*, 362(6421):1391–1395.
- [Toschi, 1997] Toschi, R. (1997). Nuclear fusion, an energy source. *Fusion engineering and design*, 36(1):1–8.
- [Troyon et al., 1988] Troyon, F., Roy, A., Cooper, W. A., Yasseen, F., and Turnbull, A. (1988). Beta limit in tokamaks. Experimental and computational status. *Plasma Phys. Controlled Fusion*, 30(11):1597–1609.
- [Tsyrovich, 2016] Tsyrovich, V. N. (2016). *An Introduction to the Theory of Plasma Turbulence: International Series of Monographs in Natural Philosophy*, volume 44. Elsevier.

- [Udintsev et al., 2005] Udintsev, V., Ottaviani, M., Maget, P., Giruzzi, G., Segui, J., Aniel, T., Artaud, J., Clairet, F., Goniche, M., Hoang, G., et al. (2005). Experimental observation of  $m/n=1/1$  mode behaviour during sawtooth activity and its manifestations in tokamak plasmas. *Plasma physics and controlled fusion*, 47(8):1111.
- [Uzdensky and Kulsrud, 2006] Uzdensky, D. A. and Kulsrud, R. M. (2006). Physical origin of the quadrupole out-of-plane magnetic field in Hall-magnetohydrodynamic reconnection. *Phys. Plasma*, 13(6):062305.
- [Uzdensky et al., 2010] Uzdensky, D. A., Loureiro, N. F., and Schekochihin, A. A. (2010). Fast Magnetic Reconnection in the Plasmoid-Dominated Regime. *Phys. Rev. Lett.*, 105(23):235002.
- [Vanovac, 2019] Vanovac, B. (2019). *Low-frequency inter-ELM pedestal modes at ASDEX Upgrade*. PhD thesis, Eindhoven University of Technology Eindhoven.
- [Vaseghi, 2008] Vaseghi, S. V. (2008). *Advanced digital signal processing and noise reduction*. John Wiley & Sons.
- [Vezinet et al., 2016] Vezinet, D., Igochine, V., Weiland, M., Yu, Q., Gude, A., Meshcheriakov, D., Sertoli, M., Team, T. A. U., and Team, T. E. M. (2016). Non-monotonic growth rates of sawtooth precursors evidenced with a new method on ASDEX Upgrade. *Nucl. Fusion*, 56(8):086001.
- [von Goeler et al., 1974] von Goeler, S., Stodiek, W., and Sauthoff, N. (1974). Studies of Internal Disruptions and  $m = 1$  Oscillations in Tokamak Discharges with Soft—X-Ray Techniques. *Phys. Rev. Lett.*, 33(20):1201–1203.
- [Wan et al., 2009] Wan, B., Collaborators, I., et al. (2009). Recent experiments in the east and ht-7 superconducting tokamaks. *Nuclear Fusion*, 49(10):104011.
- [Wan et al., 2015] Wan, M., Matthaeus, W. H., Roytershteyn, V., Karimabadi, H., Parashar, T., Wu, P., and Shay, M. (2015). Intermittent Dissipation and Heating in 3D Kinetic Plasma Turbulence. *Phys. Rev. Lett.*, 114(17):175002.
- [Wang et al., 2020] Wang, S., Wang, R., Lu, Q., Fu, H., and Wang, S. (2020). Direct evidence of secondary reconnection inside filamentary currents of magnetic flux ropes during magnetic reconnection. *Nat. Commun.*, 11(3964):1–8.
- [Wang, 2010] Wang, Y. (2010). *Nonlinear heating of the reconnection layer by strong lower hybrid instabilities*. Princeton University.
- [Webb and Howard, 2012] Webb, D. F. and Howard, T. A. (2012). Coronal mass ejections: Observations. *Living Reviews in Solar Physics*, 9(1):1–83.
- [Wesson and Campbell, 2011] Wesson, J. and Campbell, D. J. (2011). *Tokamaks*, volume 149. Oxford university press.

- [Wesson, 1990] Wesson, J. A. (1990). Sawtooth reconnection. *Nuclear Fusion*, 30(12):2545.
- [Westerhof et al., 1989] Westerhof, E., Smeulders, P., and Cardozo, N. L. (1989). Observations of sawtooth postcursor oscillations in jet and their bearing on the nature of the sawtooth collapse. *Nuclear fusion*, 29(6):1056.
- [Yamada, 2022] Yamada, M. (2022). *Magnetic Reconnection: A Modern Synthesis of Theory, Experiment, and Observations*, volume 47. Princeton University Press.
- [Yamada and Ji, 2010] Yamada, M. and Ji, H. (2010). Study of magnetic reconnection in collisional and collisionless plasmas in Magnetic Reconnection Experiment (MRX). *Proc. Int. Astron. Union*, 6(S274):10–17.
- [Yamada et al., 2010] Yamada, M., Kulsrud, R., and Ji, H. (2010). Magnetic reconnection. *Rev. Mod. Phys.*, 82(1):603–664.
- [Yamada et al., 2006] Yamada, M., Ren, Y., Ji, H., Breslau, J., Gerhardt, S., Kulsrud, R., and Kuritsyn, A. (2006). Experimental study of two-fluid effects on magnetic reconnection in a laboratory plasma with variable collisionality. *Physics of Plasmas*, 13(5):052119.
- [Yoon, 2020] Yoon, Y. D. (2020). *Probing the Progression, Properties, and Progenies of Magnetic Reconnection*. PhD thesis, California Institute of Technology.
- [Yoon and Bellan, 2018] Yoon, Y. D. and Bellan, P. M. (2018). An intuitive two-fluid picture of spontaneous 2D collisionless magnetic reconnection and whistler wave generation. *Phys. Plasma*, 25(5):055704.
- [Yoon and Bellan, 2019] Yoon, Y. D. and Bellan, P. M. (2019). The electron canonical battery effect in magnetic reconnection: Completion of the electron canonical vorticity framework. *Phys. Plasma*, 26(10):100702.
- [Yu et al., 2012a] Yu, L., Domier, C., Kong, X., Che, S., Tobias, B., Park, H., Yu, C., and Luhmann Jr, N. (2012a). Recent advances in ece imaging performance. *Journal of Instrumentation*, 7(02):C02055.
- [Yu et al., 2015] Yu, Q., Günter, S., and Lackner, K. (2015). Numerical modelling of sawtooth crash using two-fluid equations. *Nuclear Fusion*, 55(11):113008.
- [Yu et al., 2012b] Yu, Q., Günter, S., Lackner, K., and Maraschek, M. (2012b). Seed island formation by forced magnetic reconnection. *Nuclear Fusion*, 52(6):063020.
- [Yu et al., 2014] Yu, Q., Günter, S., and Lackner, K. (2014). Formation of plasmoids during sawtooth crashes. *Nucl. Fusion*, 54(7):072005.
- [Zhang, 2020] Zhang, B. (2020). The physical mechanisms of fast radio bursts. *Nature*, 587(7832):45–53.

- [Zhdankin et al., 2013] Zhdankin, V., Uzdensky, D. A., Perez, J. C., and Boldyrev, S. (2013). STATISTICAL ANALYSIS OF CURRENT SHEETS IN THREE-DIMENSIONAL MAGNETOHYDRODYNAMIC TURBULENCE. *Astrophys. J.*, 771(2):124.
- [Zohm, 2015] Zohm, H. (2015). *Magnetohydrodynamic stability of tokamaks*. John Wiley & Sons.
- [Zweibel and Yamada, 2009] Zweibel, E. G. and Yamada, M. (2009). Magnetic reconnection in astrophysical and laboratory plasmas. *Annual review of astronomy and astrophysics*, 47:291–332.
- [Zweibel and Yamada, 2016] Zweibel, E. G. and Yamada, M. (2016). Perspectives on magnetic reconnection. *Proceedings of the Royal Society A: Mathematical, Physical and Engineering Sciences*, 472(2196):20160479.

# Acknowledgements

I thank **Valentin Igochine** for always helping me to find an answer to my questions, for being available for me, for giving me a lot of freedom and for allowing me to study many topics not directly related to my PhD thesis, and for being the best supervisor I have ever had. I thank **Hartmut Zohm** for finding time to look carefully through my research results and for giving me new ideas and direction for further study. I thank Hartmut for his great book, which was an inspiration for me on how to write well, and for his nice humour. I thank **Qingquan Yu** for discussing with me any topics I bring and for always being positive and welcoming towards me. I thank **Wolfgang Suttrop** for answering many questions about physics, software and hardware and for telling entertaining stories alongside the explanations. I thank **Branka Vanovac** for sharing with me the good and bad times during the endless reparation of the ECEI diagnostic and for openly sharing her life lessons. I thank **Matthias Willensdorfer** for his unconventional views on research and science, and for the good time during ECE operation and calibration. I thank **Andreas Stegmeir** for being open to collaboration, for modifying his code to suit my purposes and for explaining to me anything I ask in a friendly and welcoming way. I thank our MHD group - **Anja Gude** and **Marc Maraschek** - for being open with me and for asking me critical questions about my research, which helped me a lot to understand what I am doing. I thank the Alternative Fusion Concepts group - **Brando Rettino**, **Pedro Molina** and **Karl Lackner** - for exciting meetings, where I could learn a lot about nuclear fusion physics. I thank my office mates - **Veronika Klevarova**, **Soeren Hansen**, **Christian Schuster** and **Felix Klossek** - for creating and supporting a friendly and calm atmosphere in our office. I thank **Petra Jordan** and **Anja Bauer** for helping me a lot with bureaucracy (visa, accommodation, HEPP and university enrollment) and for always being friendly, patient and welcoming to me. I thank **Simon Pinches** for his PhD thesis which was an inspiration and a "model" of a well-written thesis for me.

I thank my **mother**, **father** and **brother** for supporting my choices in career and life.

I thank **Clara Vienna** and **Pedro Molina** for a great time together during and outside work. I thank **Klara Höfler** for being my "older sister", for showing me the ropes in organisational and multitasking activities, and for teaching me to speak the German language. I thank **Brando Rettino** for being honest and transparent with his thoughts and for striving to find exciting research. I thank **Farah Atour** for our many walks and entertaining dialogues, and for your contagious love of mathematics. I thank **Tautvidas Jeronimas** for the friendship and for the funny discussions about Peterson and Watts. I

thank **Sasha Mustonen** for our competition in laziness. I thank **Nathan de Oliveira** for his inspirational passion for philosophy and thinking. I thank **Francesco Vannini** and **Silvia Santarelli** for the time full of joy. I thank **Marco Murace** for his authenticity and for the stupid jokes, which were amazing. I thank **Antoonio Magnianimo** for bringing an Italian vibe and Italians around. I thank **Teobaldo Luda di Cortemiglia** for being an example of how not to take work and life too seriously. I thank **Benedikt Zimmerman** for our entertaining discussions of paintings and poetry, and for bringing his Kandinsky and fitting him in. I thank **Peter Okelmann** for being one of the best flatmates I ever had and for our interesting discussions of Linux and programming.

I thank **Anzhela Valeeva** for being my other "older sister", for being an example of a person to look up to, and for helping me to discover the world of emotions. I thank **Miriam Chacon Mateos** for being the greatest friend. I thank **Maria Guitart Corominas** for a good friendship, sincere dialogues and our painting sessions. I thank **Kamshat Tazhenova** and **Dasha Postnikova** for your warm friendship and the connection despite the distance. I thank **Anton Komelkov**, **Momoka Kiyota**, **Egor Bochkarev**, **Alexander Zhukov**, **Rishat Shakirov**, **Francine Lima** and **Gosia Czepiel** for their good friendships and for the dialogues, which were bringing me a lot of joy.

Finally, I thank **Fedor Dostoevsky**, **Charles Bukowski**, **Voltaire**, **Paolo Coelho** and **Slavoi Zizek** for keeping me sane.

# The Author

The author was born on the 19th of March 1993 in Perm, Russia and was educated at Perm Gymnasium №7. He gained a Bachelor and Master degree in Applied Mathematics and Physics in Moscow Institute of Physics and Technology (Russia) in 2014 and in 2016, respectively. In 2018, he gained an Erasmus Mundus Master degree in Nuclear Fusion and Engineering Physics in Stuttgart (Germany) and Aix-Marseille (France) Universities and has accepted a research post at the Max-Planck-Institute für Plasmaphysik in Garching, Munich (Germany).

# Publications

First author:

- **Samoylov, O.**, Igochine, V., Yu, Q., Zohm, H., and AUG Team (2022). "*Magnetic reconnection rate during sawtooth crashes in ASDEX Upgrade*". Nucl. Fusion, 62(7), 074002. <https://doi.org/10.1088/1741-4326/ac6617>
- **Samoylov, O.**, Igochine, V., Stegmeir, A., Zohm, H., and AUG Team (2022). "*Global nature of magnetic reconnection during sawtooth crash in ASDEX Upgrade*". J. Plasma Phys., 88(1). doi: 10.1017/S0022377822000113

Co-author:

- Khodunov, I., Komm, M., Havranek, A., Adamek, J., Bohm, P., Cavalier, J., Seidl, J., Devitre, A., Dimitrova, M., Elmore, S., Faitsch, M., Hacek P., Havlicek, J., Hron, M., Imrisek, M., Krbec, J., Peterka, M., Panek, R., **Samoylov, O.**, Tomes, M., Tomova, K., Vondracek, P., Weinzett, M. (2021). "*Real-time feedback system for divertor heat flux control at COMPASS tokamak*". Plasma Phys. Controlled Fusion, 63(6), 065012. doi: 10.1088/1361-6587/abf03e
- Peukert, K., Jacobi, L., Geuer, J., Cisneros, I., Löffler, M., Lienig, T., Taylor, S., Gusic, M., Novakovic, N., Kuhl, T., Ordoni, E., Runge, A., **Samoylov, O.**, Narasimhan, K., Härtel, M., Amend, A., Nagel, M. "*Helmholtz Juniors Survey Report 2019*" (2020), [www.helmholtz.de/fileadmin/upload\\_Karriere/Survey\\_Report2019\\_update.pdf](http://www.helmholtz.de/fileadmin/upload_Karriere/Survey_Report2019_update.pdf)
- Komm, M., Khodunov, I., Cavalier, J., Vondracek, P., Henderson, S., Seidl, Horacek, J., Naydenkova, D., Adamek, J., Bilkova, P., Bohm, P., Devitre, A., Dimitrova M., Elmore, S., Faitsch, M., Hacek, P., Havlicek, J., Havranek, A., Imrisek, M., Krbec, J., Peterka, M., Panek, R., **Samoylov, O.**, Sos, M., Tomes, M., Tomova, K., Weinzett, V. (2019). "*Divertor impurity seeding experiments at the COMPASS tokamak*". Nucl. Fusion, 59(10), 106035. doi: 10.1088/1741-4326/ab34d2